Terahertz optoelectronics in HgTe-based heterostructures

Dissertation

zur Erlangung des Doktorgrades
der Naturwissenschaften (Dr. rer. nat.)
der Fakultät Physik
der Universität Regensburg

vorgelegt von

Stefan Hubmann

aus Weiden i.d.Opf.

im Jahr 2020

Promotionsgesuch eingereicht am: 19.10.2020

Die Arbeit wurde angeleitet von: Prof. Dr. Sergey D. Ganichev

Prüfungsausschuss

Vorsitzender: Prof. Dr. Jaroslav Fabian
1. Gutachter: Prof. Dr. Sergey D. Ganichev
2. Gutachter: Prof. Dr. Josef Zweck
weiterer Prüfer: Prof. Dr. Christian Schüller

Contents

1 Introduction

In the past decades, the HgTe material system has become the most important system for fast and sensitive detection of infrared and terahertz radiation. In this system, the band gap is highly tunable covering wavelengths from near infrared to the terahertz range [1–9]. Moreover, HgTe-based structures provide access to the novel material class of topological insulators due to the inverted band structure in HgTe [10–17]. In $Cd_xHg_{1-x}Te$ this can be achieved by tuning the Cd concentration x below a critical value x_c, which is $x_c \approx 0.17$ at a temperature $T = 4.2\,\mathrm{K}$ [18, 19]. This allows an access to helical surface states, which are a fingerprint for three-dimensional topological insulators. Moreover, low-dimensional structures such as HgTe/CdHgTe quantum wells (QWs) can be fabricated, whose band gap is also tunable between inverted and non-inverted band ordering. This is done by varying the thickness d of the quantum well, where QWs above the critical thickness of $d \approx 6.3\,\mathrm{nm}$ exhibit a band inversion and, thus, provide access to one-dimensional helical edge channels. These unique properties of HgTe-based systems led to the observation of fascinating phenomena like Kane fermions in $Cd_xHg_{1-x}Te$ [19–21], the quantum spin Hall effect [11, 12, 22] and helical edge photocurrents in HgTe QWs [23]. Moreover, Lindner et al. recently proposed the possibility to convert a topologically trivial HgTe QWs into a Floquet topological insulator by applying circularly polarized intense terahertz radiation [24]. The resulting chiral edge states are a fingerprint of topological insulators and could be proved by the terahertz-radiation induced generation of helical edge photocurrents as demonstrated in Ref. [23] for topologically nontrivial HgTe QWs. Thus, the investigation of optoelectronics applying terahertz radiation to HgTe-based structures is a highly interesting field of research. Consequently, this work is devoted to studies of optoelectronic phenomena in HgTe QWs and $Cd_xHg_{1-x}Te$ induced by terahertz radiation.

In the first part of this work photoresponses induced by intense terahertz radiation in topologically trivial HgTe QWs have been studied under the conditions suggested in Ref. [24]. The observed photocurrent shows a strongly nonlinear dependence changing the current sign at a certain intensity and featuring a superlinear dependence at high intensities. Analyzing the nonlinear behavior revealed that it originates from the phenomenon of light impact ionization. Due to this effect electron-hole pairs are generated by radiation with photon energies much smaller than the band gap energy ε_g. Previously,

light impact ionization has been observed in InSb crystals and other two- and three-dimensional semiconductor systems [25–31]. In contrast to these previous works the product of momentum relaxation time τ and radiation angular frequency ω is larger than unity in the framework of this thesis. On that condition, charge carriers reach high energies in the high-frequency radiation electric field due to multiple collisions [32–34]. Moreover, unlike previous studies of light impact ionization, the phenomenon is firstly reported while the Fermi energy is larger than the gap energy in the samples studied in this work. Under this condition, electron gas heating is crucial to deplete the final states for the impact ionization process in the conduction-band rather than just increasing the number of electrons with an energy above the impact ionization threshold energy [35, 36].

In the framework of this thesis, optoelectronics in bulk $Cd_xHg_{1-x}Te$ were studied in addition to HgTe QWs. Here, also a strongly nonlinear photocurrent was detected. Strikingly, similar to the photocurrents observed in HgTe QWs, this photocurrent features a change of sign with the radiation intensity caused by light impact ionization. The fact that this effect is present also in this material demonstrates the fundamental origin of light impact ionization. Moreover, a surprising, helicity-dependent photocurrent contribution, i.e, the circular photogalvanic effect (CPGE), has been detected in $Cd_xHg_{1-x}Te$, even though this effect is forbidden by symmetry in this material. In all previous works the point group symmetry of $Cd_xHg_{1-x}Te$ films has been supposed to be T_d, resembling the system's crystallographic structure. However, the CPGE is only possible in gyrotropic systems [32, 37], so the appearance of this effect is symmetry-forbidden in systems belonging to the non-gyrotropic T_d point group. In order to explain the formation of the CPGE in $Cd_xHg_{1-x}Te$ the films are considered to be strained causing a symmetry reduction of the crystal and, consequently, the CPGE is possible.

The thesis is organized as follows: In Chap. 2, theoretical basics relevant to this work are outlined: First, the HgTe material system, see Sec. 2.1 is described. The properties of bulk HgTe are depicted as well as the specifics of HgTe QWs and also a short description of $Cd_xHg_{1-x}Te$ films is given. In the following section, see Sec. 2.2, a phenomenological description of nonlinear optoelectric phenomena, in particular the photogalvanic effect (PGE) is given. This description is supplemented with exemplary microscopic mechanisms for the linear photogalvanic effect (LPGE) in structures with C_{3v}-symmetry and the CPGE in n-type quantum wells with C_s-symmetry as well

as in helical edge states, which are present in topological insulators. Furthermore, the photoconductivity effect is introduced phenomenologically and the microscopical description of terahertz-radiation induced electron gas heating and μ-photoconductivity is given. The last section, Sec. 2.3, outlines the specifics of impact ionization starting with general considerations and a short description of this effect in dc fields concluding with the peculiarities of light impact ionization. Chapter 3 is devoted to the properties of the samples investigated during this work and the corresponding measurement setup. Section 3.1 starts outlining the properties of the two HgTe QW wafers used in this work and describes the characteristics of the four investigated $Cd_xHg_{1-x}Te$ samples. Furthermore, in Sec. 3.2 the specifics of the setup are outlined including the used radiation sources, the optical setup, as well as the electrical signal detection.

The description of the experimental results starts with the presentation of the data obtained for HgTe QWs in Chap. 4. The data for strongly nonlinear terahertz-radiation induced photocurrent and photoconductivity detected in the HgTe QW below the critical thickness are shown in Sec. 4.1. In the following Sec. 4.2, the results for the HgTe QW close to critical thickness are presented. This is followed by a detailed analysis of both nonlinear photoconductivity and photocurrent in Sec. 4.3. This analysis shows that the observed nonlinearities are caused by the electron-hole-pair generation induced by light impact ionization and the subsequent photogalvanic effect on photogenerated electrons and holes. In Chap. 5 the results for $Cd_xHg_{1-x}Te$ samples are presented. Starting with a short presentation of the nonlinearities observed in this material, see Sec. 5.1, the main part of this chapter is devoted to the observed CPGE in $Cd_xHg_{1-x}Te$. The experimental results corresponding to this phenomenon are presented in Sec. 5.2 and are discussed and analyzed in Sec. 5.3. The analysis suggests that the origin of the observed CPGE in $Cd_xHg_{1-x}Te$ films is the symmetry reduction of the $Cd_xHg_{1-x}Te$ crystal due to strain. In the last chapter, Chap. 6, the work is summarized and a short outlook to further investigations is given.

2 Theoretical basics

2.1 HgTe-based structures

In this work different HgTe-based material systems are used, thus, this section outlines the properties of bulk HgTe as well as the properties of HgTe QWs and bulk $Cd_xHg_{1-x}Te$.

2.1.1 Band structure of bulk HgTe

HgTe is a II-VI material which crystallizes in zinc-blende structure. In this material the conduction band states are formed by p-states located at the group VI atoms. Consequently, the valence band states are formed by s-like states located at the group II atoms [38]. From this follows that the band ordering around the Γ-point is inverted [10, 12, 39]. The conduction band in bulk HgTe consists of the light-hole band LH_1 from the Γ_8 bands, while the valence band consists of the heavy-hole band HH_1 of the Γ_8 bands. Between conduction and valence band no band gap exists, but the heavy-hole band maxima are displaced in k and thus, valence and conduction bands overlap by $\Delta\varepsilon$ [10], see Fig. 1(a). This together with the inverted band structure classifies HgTe as a topological semimetal [42, 43]. The peculiar band structure is caused by several corrections to the initial Hamiltonian $\mathcal{H}_{\text{int}}$ describing the

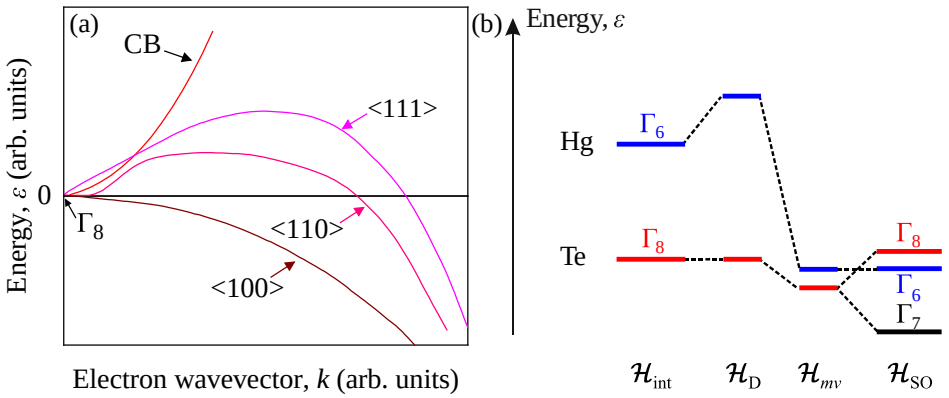

Figure 1: Panel (a): Sketch of the valence band in HgTe along different $\boldsymbol{k}$-directions together with the conduction band (CB). Figure adapted from [40]. Panel(b): Sketch of the energy levels at the Γ point in HgTe without consideration of relativistic effects ($\mathcal{H}_{\text{int}}$), with additionally considering the Darwin term ($\mathcal{H}_{\text{D}}$), the mass velocity correction($\mathcal{H}_{\text{mv}}$), and with considering the spin-orbit interaction ($\mathcal{H}_{\text{SO}}$). Figure adapted from Refs. [10, 39, 41].

system. These corrections are the Darwin term $\mathcal{H}_{\mathrm{D}}$, the spin-orbit interaction $\mathcal{H}_{\mathrm{SO}}$, and the mass-velocity term $\mathcal{H}_{\mathrm{MV}}$. In other II-VI materials, e.g. CdTe, the corrections have only little influence on the bands, but they are crucial for the band formation in HgTe. Since the atomic mass of the Hg atoms is large, the mass-velocity correction term $\mathcal{H}_{\mathrm{MV}}$ lowers the Γ_6 band to a similar energy value as the Γ_8 band. The spin-orbit interaction term $\mathcal{H}_{\mathrm{SO}}$ splits the Γ_8 band into a double-degenerated Γ_8 and a Γ_7. This splitting leads to a shift of the s-like Γ_6-band below the p-like Γ_8 band and thus, to an inverted band structure. The effect of the different corrections are sketched in Fig. 1(b). The k-displacement of the heavy-hole band mentioned above is caused by k-linear terms in the dispersion relation present due to the lack of an inversion center in the zinc-blende structure.

In order to open a band gap in the topological semimetal HgTe and access the whole range of dispersions from a trivial semiconductor to a Dirac-like linear dispersion to an inverted band ordering, several techniques are used. One possibility is the growth of thin HgTe QWs between CdTe barriers as described in Sec. 2.1.2. A band gap in bulk HgTe can be also opened by uniaxial strain yielding a three-dimensional topological insulator. [44, 45]. Another possibility to engineer the band gap is the substitution of a certain fraction x of the Hg atoms with Cd atoms, forming $\mathrm{Cd}_x\mathrm{Hg}_{1-x}\mathrm{Te}$ films, which is described in Sec. 2.1.3.

2.1.2 HgTe/CdTe quantum wells

In contrast to HgTe, bulk CdTe features a trivial semiconductor band structure, where the conduction band is formed by s-like states from the Γ_6 band and the valence band is formed by p-like states from the Γ_8 bands. Just as in HgTe, the band gap is smallest at the Γ-point in the Brillouin zone, see Fig. 2. Fabricating a QW from HgTe with CdTe barriers (referred to as HgTe/CdTe QW in the following) gives access to the peculiar properties of HgTe and makes band gap engineering possible. The following considerations are done according to Ref. [11].

At the Γ-point ($k_\parallel = 0$) of a HgTe/CdTe QW the three quantum well subband states E_1, H_1 and L_1 are formed. The L_1 subband is split off from the other two subbands and is neglected in the following considerations. The state $|E_1, m_J\rangle$ consists of a linear combination of the $|\Gamma_6, m_J = \pm 1/2\rangle$ and the $|\Gamma_8, m_J = \pm 1/2\rangle$ states, where m_J is the total angular momentum quantum

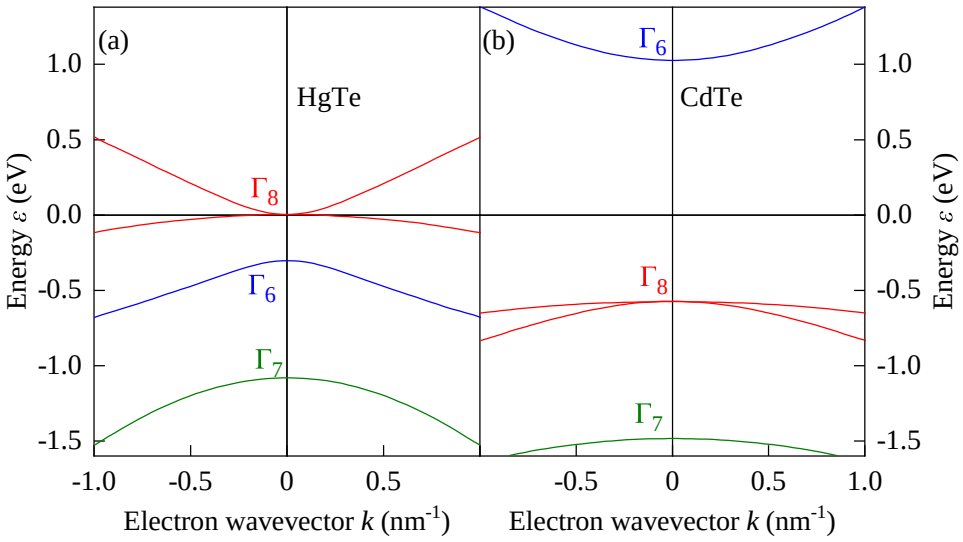

Figure 2: Sketch of the dispersion of bulk HgTe (a) CdTe (b) in the vicinity of the Γ-point. Figure adapted from [11].

number. The H_1 subband state, however, is formed by the $|\Gamma_8, m_J = \pm 3/2\rangle$ states. At $k_\parallel \neq 0$, the states E_1 and H_1 can intermix. The effective Hamiltonian can then be derived and expressed in the basis of $|E_1, 1/2\rangle$, $|H_1, 3/2\rangle$ and $|E_1, -1/2\rangle$, $|H_1, -3/2\rangle$:

$$\mathcal{H}_{\text{eff}}(k_x, k_y) = \begin{pmatrix} \mathcal{H}(k) & 0 \\ 0 & \mathcal{H}^*(-k) \end{pmatrix}, \quad \mathcal{H}(k) = \epsilon(k) + d_i(k)\sigma_i, \tag{1}$$

where σ_i are the Pauli matrices, $d_i(k)$ can be deduced to

$$\begin{aligned} d_1 + id_2 &= A(k_x + ik_y)\,, \\ d_3 &= M - B(k_x^2 + k_y^2)\,, \end{aligned} \tag{2}$$

due to symmetry arguments and

$$\epsilon(k) = C - D(k_x^2 + k_y^2)\,. \tag{3}$$

Here, A, B, C and D are material-specific expansion parameters, k_x and k_y are the electron momentum components in the QW plane and M is the Dirac mass parameter. The Dirac mass parameter describes the energy difference between the two QW subbands E_1 and H_1 at the Γ-point and, consequently, the band ordering. A positive M describes a "normal" band ordering similar to CdTe with the energies of the s-like E_1-band above the p-like H_1 at the Γ-point,

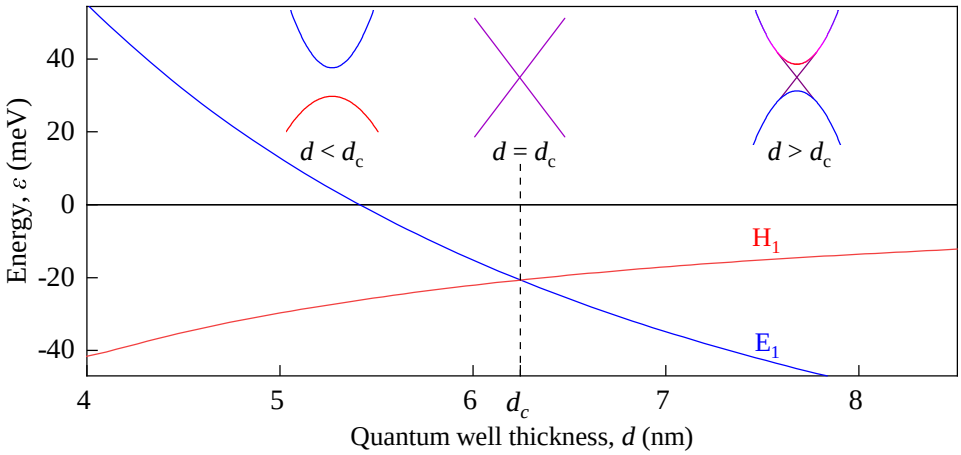

Figure 3: Energies of the E_1 and the H_1 bands at $k_{\parallel} = 0$ as a function of the QW thickness. Insets show an exemplary sketch of the dispersions of HgTe QWs with $d < d_c$, $d = d_c$ and $d > d_c$. Note that the underlying calculations were done for HgTe QWs with $Cd_{0.68}Hg_{0.32}Te$ barriers [11] and the value of d_c changes with the barrier composition. Figure and insets adapted from [11].

while $M < 0$ indicates an inverted band ordering with the H_1 band above the E_1 band. In HgTe/CdTe QWs the Dirac mass parameter M depends on the thickness of the QW d_{QW}, see Fig. 3: In QWs smaller than a critical thickness d_c the band ordering of CdTe dominates and, thus, the Dirac mass parameter is positive and the E_1-band lies above H_1 yielding a semiconductor-like behavior. In wider QWs, however, the band ordering of HgTe dominates, H_1 shifts above E_1, and, consequently, the QW exhibits $M < 0$. This regime belongs to the class of topological insulators. Here, helical pseudospin-polarized edge states with a Dirac-like linear dispersion form at the interface between the band-inverted HgTe/CdTe QW and a material with a topologically trivial material (e.g. air). These states are topologically protected and are energetically located in the band gap between the valence and conduction band. A more detailed description of topological insulators can be found in Refs. [12, 15, 46]. At $d_{\mathrm{QW}} = d_c$ the Dirac mass parameter changes its sign and is equal to zero. At this quantum well thickness, the system is effectively described by the Dirac equation for massless particles [12] leading to a graphene-like linear dispersion with a minimal band gap.

Note that real HgTe/CdTe QW barriers are typically made of $Cd_xHg_{1-x}Te$ instead of CdTe and the Cd concentration x in the barrier also affects the exact value of the critical thickness d_c. Additionally, the band ordering in HgTe QWs is dependent on temperature and strain. [47, 48]

2.1.3 $Cd_xHg_{1-x}Te$ films

Another possibility to open a band gap in HgTe, which is outlined shortly in this section, is the replacement of a fraction x of the Hg atoms with lighter Cd atoms. Due to the lower weight of the Cd atoms, this substitution reduces the influence of the relativistic effects responsible for the band structure in HgTe (see Sec. 2.1.1) [10]. The main consequence is the shifting of the s-like Γ_6-band to higher energies with increasing the Cd concentration [52], yielding the possibility to smoothly tune the band structure with the Cd concentration x, similar to the tunability of HgTe QWs with the thickness d_{QW}, see previous section. Consequently band gap values between $\varepsilon_{\mathrm{g}} = -300\,\mathrm{meV}$ and $\varepsilon_{\mathrm{g}} = 1.6\,\mathrm{eV}$ can be achieved in $Cd_xHg_{1-x}Te$ films, depending on the Cd concentration. For a certain critical concentration x_c the band gap vanishes ($\varepsilon_{\mathrm{g}} = 0$) and a Dirac-like linear dispersion is established. For $x < x_c$, the band gap is negative yielding a three-dimensional topological insulator, which makes the formation of

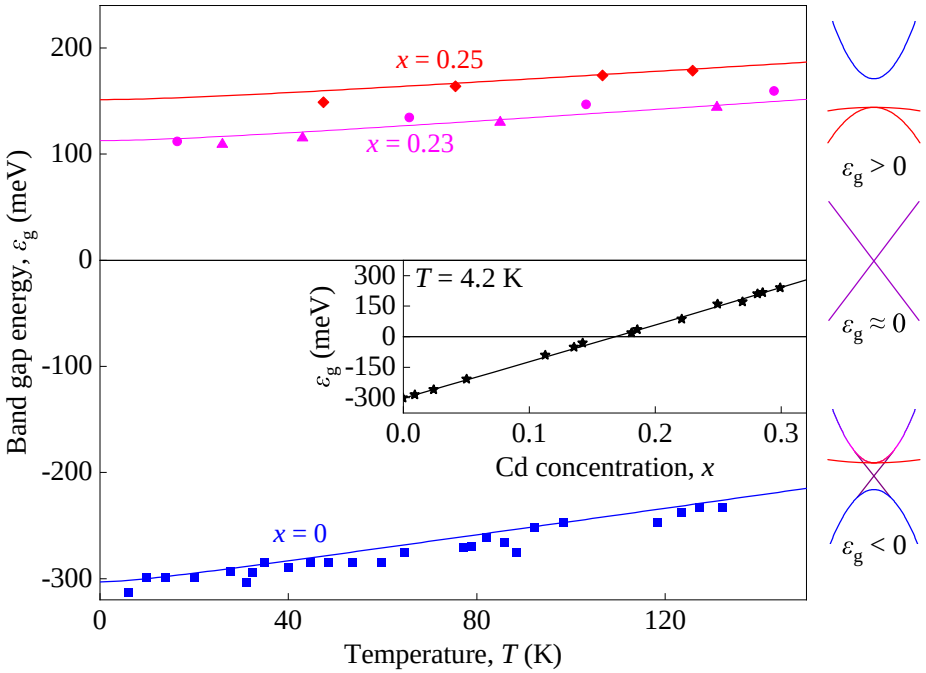

Figure 4: Band gap energy versus temperature for $Cd_xHg_{1-x}Te$ films with Cd concentrations $x = 0.25, 0.23$, and $x = 0$ (HgTe). Inset shows the dependence of the band gap energy on the Cd concentration at a temperature of 4.2 K. The solid lines show the calculated dependencies according to Ref. [18], while the data points show experimental values from Refs. [18] (circles), [49] (diamonds and squares), [50] (triangles), and [51] (stars). The sketches on the side represent the band structure for $\varepsilon_{\mathrm{g}} > 0$, $\varepsilon_{\mathrm{g}} \approx 0$ and $\varepsilon_{\mathrm{g}} < 0$. Figure adapted from Ref. [19].

topologically protected surface states with linear dispersion possible. For Cd concentrations above the critical concentration, the $Cd_xHg_{1-x}Te$ film exhibits a trivial semiconducting behavior. Furthermore, $Cd_xHg_{1-x}Te$ films exhibit a characteristic temperature dependence of the band gap [18, 19], and, consequently, the value of x_c also depends on the temperature. The temperature dependence is schematically shown for $Cd_xHg_{1-x}Te$ with different Cd concentrations x in Fig. 4. The inset depicts the dependence of the band gap energy ε_g on the Cd concentration x at a fixed temperature of $T = 4.2\,\mathrm{K}$.

2.2 Nonlinear optoelectric phenomena

Illumination of a material with terahertz radiation can lead to direct electric currents in the solid due to the alternating radiation electric field. These effects are termed nonlinear, if they are proportional to the second or higher order of the electric field. In this section nonlinear optoelectric phenomena are described phenomenologically and examples of corresponding microscopical models are given.

In the following, the radiation electric field is described by a plane wave

$$\boldsymbol{E}(\boldsymbol{r},t) = \boldsymbol{E}(\omega,\boldsymbol{q})\mathrm{e}^{-i\omega t+i\boldsymbol{q}\cdot\boldsymbol{r}} + \boldsymbol{E}^*(\omega,\boldsymbol{q})\mathrm{e}^{i\omega t-i\boldsymbol{q}\cdot\boldsymbol{r}}, \tag{4}$$

where ω is the angular frequency of the electric field, the asterisk marks complex conjugation and $\boldsymbol{q}$ is the photon momentum.

Phenomenologically, the influence of electric fields on the current density can be expanded in a series of powers of the radiation electric field E [53]:

$$\begin{aligned} j_\alpha(\boldsymbol{r},t) = &\sum_\beta \left[\sigma^{(1)}_{\alpha\beta}E_\beta(\omega,\boldsymbol{q})\mathrm{e}^{-i\omega t+i\boldsymbol{q}\cdot\boldsymbol{r}} + c.c.\right] \\ + &\sum_{\beta,\gamma}\left[\sigma^{(2')}_{\alpha\beta\gamma}E_\beta(\omega,\boldsymbol{q})E_\gamma(\omega,\boldsymbol{q})\mathrm{e}^{-2i\omega t+2i\boldsymbol{q}\cdot\boldsymbol{r}} + c.c.\right] \\ &+\sum_{\beta,\gamma}\left[\sigma^{(2)}_{\alpha\beta\gamma}E_\beta(\omega,\boldsymbol{q})E^*_\gamma(\omega,\boldsymbol{q})\right] + ... \end{aligned} \tag{5}$$

Here, σ is the conductivity tensor, the summation indices α, β and γ take the values of the Cartesian coordinates x, y, and z and *c.c.* denotes the complex conjugate. Note that the equation is limited to second order effects for simplicity, and third order effects are discussed in a special case later in this section. The first part of Eq. (5) describes the linear response of the current density j. This part averages to zero for an alternating electric field and, con-

sequently, vanishes in the case of terahertz radiation as a source of the electric field. Being proportional to $e^{-2i\omega t}$, the second part in Eq. (5) describes second harmonic generation. This effect is not a main subject of this thesis and therefore, it is neglected in the following. The third part in Eq. (5), however, has no oscillatory contributions and, consequently, describes a dc current density response to the ac radiation electric field. Since this part is mainly responsible for the photocurrents measured in the experiments, the focus is put on this part. The second-order conductivity $\sigma^{(2)}_{\alpha\beta\gamma}(\omega, \boldsymbol{q})$ corresponding to the dc current can be expressed by a sum of the photon momentum-dependent and a photon momentum-independent part: [53, 54]

$$\sigma^{(2)}_{\alpha\beta\gamma}(\omega, \boldsymbol{q}) = \sigma^{(2)}_{\alpha\beta\gamma}(\omega) + \sigma^{(2)}_{\alpha\beta\gamma}(\omega, \boldsymbol{q}) \tag{6}$$

The two parts of Eq. (6) are then redefined:

$$\sigma^{(2)}_{\alpha\beta\gamma}(\omega) = \chi_{\alpha\beta\gamma}(\omega), \qquad \sigma^{(2)}_{\alpha\beta\gamma}(\omega, \boldsymbol{q}) = T_{\alpha\delta\beta\gamma} q_\delta \tag{7}$$

Here, $\chi_{\alpha\beta\gamma}$ is a third rank tensor and $T_{\alpha\delta\beta\gamma}$ is a fourth rank tensor. Using these definitions and Eq. (6), Eq. (5) can be rewritten to

$$j_\alpha = \underbrace{\sum_{\beta,\gamma} \chi_{\alpha\beta\gamma} E_\beta E^*_\gamma}_{\text{photogalvanic effect}} + \underbrace{\sum_{\delta,\beta,\gamma} T_{\alpha\delta\beta\gamma} E_\beta E^*_\gamma q_\delta}_{\text{photon drag effect}} \tag{8}$$

The first part of Eq. (8) describes the PGE, while the second part yields the photon drag effect (PDE).

Note that the PGE is only possible in noncentrosymmetric systems, since $j_\alpha(-r) = -j_\alpha(r)$ can only be fulfilled for $\chi_{\alpha\beta\gamma} = 0$. The PDE, however, is possible in both centro- and noncentrosymmetric systems due to its dependence on the wave vector $\boldsymbol{q}$ [53].

In order to describe the polarization dependence of both PGE and PDE the product $E_\beta E^*_\gamma$ is mathematically rewritten into a real symmetric part $\left\{E_\beta E^*_\gamma\right\} = \frac{1}{2}\left(E_\beta E^*_\gamma + E_\gamma E^*_\beta\right)$ and an antisymmetric purely imaginary part $\left[E_\beta E^*_\gamma\right] = \frac{1}{2}\left(E_\beta E^*_\gamma - E_\gamma E^*_\beta\right)$:

$$E_\beta E^*_\gamma = \left(\left\{E_\beta E^*_\gamma\right\} + \left[E_\beta E^*_\gamma\right]\right) \tag{9}$$

In the following, the description is exemplarily done for the PGE, the charac-

terization of the PDE can be done in an analogue way. In Eq. (9), the first term is real and symmetric, while the second term is purely imaginary and antisymmetric. In order to describe the effect of circular polarization on the PGE, $\chi_{\alpha\beta\gamma}$ is reduced to a second rank pseudotensor $\xi_{\alpha\nu}$ using tensor contraction with the totally antisymmetric Levi-Civita tensor $\epsilon_{\nu\beta\gamma}$ on the antisymmetric part $\left[E_\beta E_\gamma^*\right]$ [32]:

$$\sum_{\beta,\gamma} \chi_{\alpha\beta\gamma} \left[E_\beta E_\gamma^*\right] = i \cdot \sum_{\nu,\beta,\gamma} \xi_{\alpha\nu} \epsilon_{\nu\beta\gamma} \left[E_\beta E_\gamma^*\right] = \sum_{\nu} \xi_{\alpha\nu} i \left(\boldsymbol{E} \times \boldsymbol{E}^*\right)_\nu \tag{10}$$

To summarize, the total photocurrent density related to the PGE can be denoted by

$$j_\alpha = \underbrace{\sum_{\beta,\gamma} \chi_{\alpha\beta\gamma} \left\{E_\beta E_\gamma^*\right\}}_{\text{linear photogalvanic effect}} + \underbrace{\sum_{\nu} \xi_{\alpha\nu} i \left(\boldsymbol{E} \times \boldsymbol{E}^*\right)_\nu}_{\text{circular photogalvanic effect}} \tag{11}$$

Here the first term describes the LPGE, while the second term describes the CPGE. The LPGE is excited by linearly polarized radiation, and is allowed only in non-centrosymmetric media of piezoelectric crystal classes, where $\chi_{\alpha\beta\gamma}$ has nonzero components. The CPGE, however, depends solely on the radiation helicity and is not induced by linearly polarized radiation. Since the CPGE depends on the second-rank pseudotensor $\xi_{\alpha\nu}$, this effect is only allowed in gyrotropic media [32].

2.2.1 LPGE in structures with C_{3v}-symmetry

A simple microscopical model for the generation of the LPGE can be given for structures belonging to the C_{3v}-symmetry group. In such systems, no inversion center is present and, thus, the elastic scattering is asymmetric even for scatterers without anisotropy [55–57]. This can be written as $W_{\boldsymbol{p},\boldsymbol{p}'} \neq W_{-\boldsymbol{p},-\boldsymbol{p}'}$, where $W_{\boldsymbol{p},\boldsymbol{p}'}$ is the probability that an electron with initial momentum $\boldsymbol{p}'$ obtains the momentum $\boldsymbol{p}$ after the elastic scattering process. The generation of the LPGE can be visualized considering such asymmetric elastic scattering of charge carriers on randomly distributed, but equally oriented triangle-shaped wedges representing C_{3v}-symmetry [32, 56, 58]. The wedges and the current generation mechanisms are sketched in Fig. 5. In equilibrium, the carrier momenta are randomly distributed along any direction. Application of an external ac electric field $\boldsymbol{E}$, e.g., the radiation electric field of terahertz radiation, re-

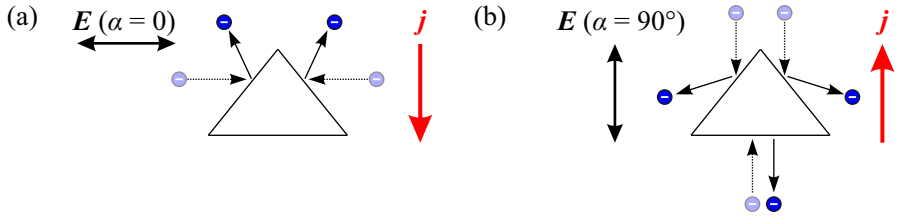

Figure 5: Schematic illustration of the microscopic mechanism of LPGE generation due to elastic scattering on triangle-shaped wedges. The radiation electric field $\boldsymbol{E}$ causes the charge carriers exemplarily sketched as electrons (blue) to move (dotted arrows). Elastic scattering on the wedges causes an alignment of carrier momenta (solid arrows) and, consequently, a photocurrent $\boldsymbol{j}$ (red arrow). Panels (a) and (b) show two different orientations of the electric field vector $\boldsymbol{E}$ and the corresponding photocurrent $\boldsymbol{j}$. Figure adapted from Refs. [32, 56, 58].

sults in an optical alignment of the carrier momenta along the radiation electric field[1]. This alignment of carriers is described by the second angular harmonic of the distribution function $f_{\boldsymbol{p}}^{(2)} \propto |\boldsymbol{E}|^2$ and does not result in a current by itself. The photocurrent is generated due to elastic asymmetric scattering of the momentum-aligned carriers on the wedges, see Fig. 5. Direction and amplitude of the photocurrent depend on the orientation of the electric field with respect to the wedges: If the electric field is aligned parallel to the wedges' base, the photocurrent is generated in a direction normal to the electric field $\boldsymbol{E}$ due to elastic scattering on the wedges, see Fig. 5(a). However, the photocurrent direction is reversed for the electric field oriented normal to the base of the wedges, see Fig. 5(b). This change of sign with the rotation of the electric field results in a characteristic polarization dependence, i.e., the LPGE.

2.2.2 Exemplary microscopic models for the CPGE

In general, microscopic models of both LPGE and CPGE crucially depend on the symmetry of the investigated structure as well as the polarization of the incident radiation [32]. In order to visualize the phenomenological description of the PGE explained above, two exemplary microscopic models of the CPGE are described in the following.

2.2.2.1 CPGE in n-type quantum wells with C_s-symmetry As a first example, a microscopic model considering inter-subband transitions between size-

[1]Note that the carriers get optically aligned parallel to the electric field only in the regime of Drude absorption and intraband transitions [59, 60], which is typically relevant in the terahertz range, but normal to the electric field for interband transitions [61].

quantized subbands in n-type QWs belonging to the C_s point group symmetry excited by normally incident radiation is described [32, 41, 62, 63]. In structures with these properties, the Hamiltonian has the form [41]

$$\mathcal{H} = \frac{\hbar^2 k^2}{2m^*} + \mathcal{H}_{\mathrm{SO}} \,. \tag{12}$$

Here, m^* denotes the effective mass and $\mathcal{H}_{\mathrm{SO}}$ is an additional term due to the spin-orbit interaction. The spin-orbit interaction term can be written as [32]

$$\mathcal{H}_{\mathrm{SO}} = \sum_{\gamma\delta} \beta_{\gamma\delta} \sigma_\gamma k_\delta \,, \tag{13}$$

where $\beta_{\gamma\delta}$ is a second-rank pseudotensor, σ_γ are the Pauli matrices, and the summation is done over the cartesian coordinates $\gamma, \delta = x, y, z$. In structures of the C_s point symmetry group, the term proportional to $\sigma_z k_x$ in Eq. (13) is symmetry-allowed and leads to a splitting of the initially spin-degenerate bands into spin subbands with the projection of the spin $m_s = \pm 1/2$ on the growth direction z (corresponding states are labeled $|\pm 1/2\rangle_z$ in the following). In order to simplify the model, only the first two conduction subbands E1 and E2 are considered. The conduction band splitting can be described by [32]

$$\varepsilon_{\mathrm{E}\nu,\pm 1/2}(k_x) = \frac{\hbar^2 k_x^2}{2m^*} \pm \beta^{(\mathrm{E}\nu)} k_x \,, \tag{14}$$

where $\nu = 1, 2$ denotes the subband index. The spin splitting of the conduction subbands is visualized in Fig. 6. For circularly polarized radiation and incidence normal to the QW plane, optical selection rules only allow transitions between subbands including a respective spin-flip, i.e. $\Delta m_s = +1$ for right-handed circularly polarized (σ^+) radiation and $\Delta m_s = -1$ for left-handed circularly polarized radiation (σ^-). Consequently, for monochromatic left-circularly polarized radiation with an angular frequency ω_1 only the transition at $-k_x'$ sketched in Fig. 6(a) is allowed due to selection rules and energy conservation. This transition leads to an asymmetry of the electron/hole momentum distribution in both the E1 and the E2 subbands, i.e. electric current contributions with different sign for both subbands. Typically, the energy separation between the E1 and E2 subbands in n-type QWs is larger than the longitudinal optical phonon energy $\hbar\Omega_{\mathrm{LO}}$ and, consequently, the relaxation time of the excited electrons in the E2 subband is very small due to the emission of phonons. Thus, the current contribution from the E2 band can be neglected due to the

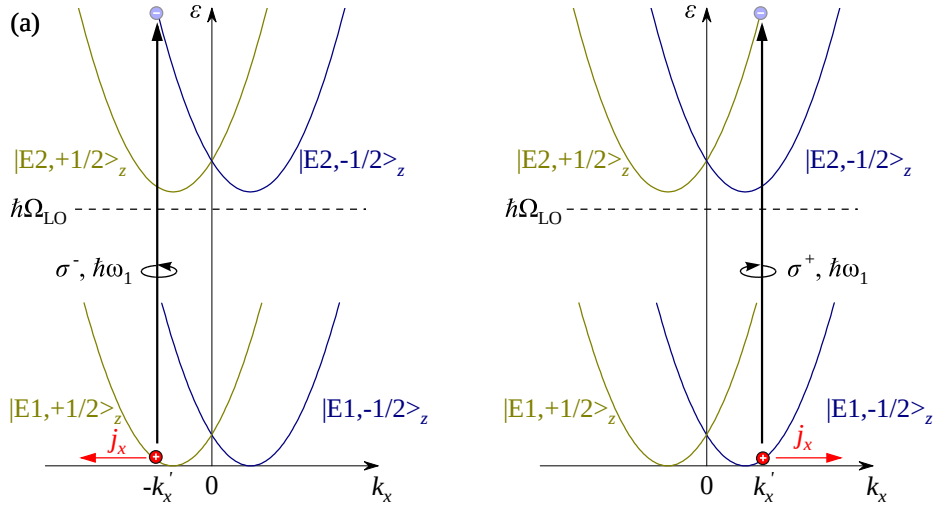

Figure 6: Microscopic theory of the CPGE in a QW with C_s point group symmetry considering the split first two conduction subbands E1 and E2. Dashed black line shows the longitudinal optical phonon energy $\hbar\Omega_{\mathrm{LO}}$ Panel (a): Photocurrent excited by left-circularly polarized radiation with photon energy $\hbar\omega_1$. Due to selection rules and energy conservation, only the sketched transition (blue arrow) is allowed. The dominating current contribution comes from the holes with momentum $-k_x'$ in the E1 subband (red), since the electrons in the E2 subband relax very fast due to emission of optical phonons yielding the current j_x (red arrow). Panel (b): Photocurrent excited by right-circularly polarized radiation with the same photon energy $\hbar\omega_1$ as in Panel (a). Here, the optical transition takes place at k_x', and, consequently the photocurrent reverses its sign compared to Panel (a). Figure adapted from [32].

fast relaxation and the dominating current results from the holes in the E1 band, see red arrow in Fig. 6(a). Consequently, the photocurrent is dependent on the relaxation time and group velocity of the holes in the E1 band. For right-handed circularly polarized radiation, however, the transitions take place at $+k_x'$ and, consequently, the photocurrent reverses its sign as compared to the respective case for left-circularly polarized radiation, see Fig. 6(b). Note that variation of the photon energy leads to a shift of k_x' and can even lead to a sign inversion of the photocurrent without the change of polarization [32].

2.2.2.2 Helical Edge Currents in Topological Insulators Recently, it has been shown that helical edge channels in topological insulators can be probed by measurements of the terahertz-induced photocurrent [23, 64, 65]. Since helical edge photocurrents are also important for the discussion of some of the results in this work, an underlying mechanism for helical edge photocurrents in topological insulators is introduced below.

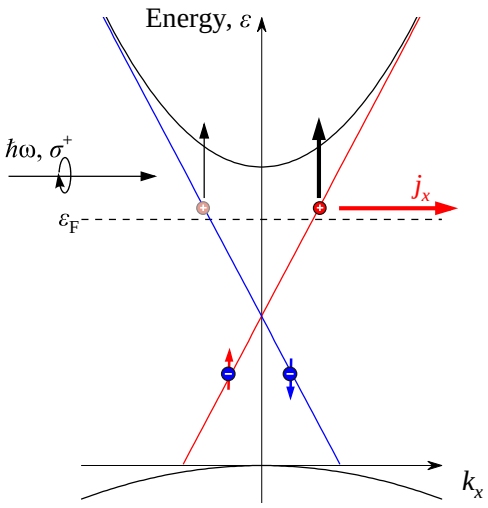

Figure 7: Schematic of the generation of a helical edge photocurrent excited by right-handed circularly polarized (σ^+) radiation. Figure adapted from Ref. [23].

For the following model, pseudospin-polarized topological one-dimensional edge states with linear dispersion are considered lying in the band gap between parabolic valence and conduction bands, see Fig. 7. Note that this is the corresponding situation, e.g., for HgTe QWs slightly above the critical thickness, see Sec. 2.1.2. The Fermi energy ε_F is considered to be in the bulk band gap. Furthermore, the radiation is assumed to fulfill $\hbar\omega \ll \varepsilon_\mathrm{g}$, so that direct optical band-to-band transitions are not possible.

If the Fermi energy is near the conduction band bottom, transitions from helical edge states to the bulk conduction band (="photoionization of edge states") are possible, see Fig. 7(a). For right-handed circularly polarized (σ^+) radiation, the probability of the optical transitions involving the spin-up band with pseudospin $s = +1/2$ (red line in Fig. 7) is higher than the transitions from the states with pseudospin $s = -1/2$ due to selection rules [64, 65], as indicated by the thicker arrow in Fig. 7. This depletion of the edge states with positive k_x due to the dominant optical transition leads to an imbalance of carriers in the $\boldsymbol{k}$-space and, consequently, an electric current. For left-handed circularly polarized (σ^-) radiation , transitions from the spin-down band to the conduction band are dominant and, consequently, the photocurrent direction reverses its sign compared to excitation with σ^+-radiation. To sum up, this leads to a change of sign of the photocurrent for excitation by right- and left-circularly polarized radiation, i.e., the CPGE.

2.2.3 Third order effects - photoconductivity

In the phenomenological Eq. (5) the expansion has been limited to second order effects. In general, effects proportional to the third order of the electric field can also be efficiently excited, in particular in the case, where a static field $\boldsymbol{E}^{(\mathrm{dc})}(0,0)$ and an electromagnetic wave, defined according to Eq. (4), interact. This special case corresponds to photoconductivity phenomena, where the static electric field $\boldsymbol{E}^{(\mathrm{dc})}(0,0)$ is caused by an external bias, while the electromagnetic wave comes from the incoming radiation, see also the experimental setup in Sec. 3.2.2. Since a main part of this work is devoted to photoconductivity data, this phenomenon is especially important. In this situation, expanding similar to Eq. 5 leads to [53, 56]

$$j_\alpha(\boldsymbol{r},t) = \sum_{\beta\gamma\delta} \sigma^{(3'')}_{\alpha\beta\gamma\delta} E_\beta(\omega,\boldsymbol{q}) E^*_\gamma(\omega,\boldsymbol{q}) E^{(\mathrm{dc})}_\delta(0,0)\,. \tag{15}$$

with the corresponding fourth-order conductivity tensor $\sigma^{(3'')}_{\alpha\beta\gamma\delta}$. According to Eq. (15), the resulting current is proportional to the amplitude of the static electric field and the radiation intensity $I \propto |\boldsymbol{E}|^2(\omega,\boldsymbol{q})$. Examples for the microscopic mechanism of photoconductivity phenomena follow in the next sections.

Electron gas heating and μ-photoconductivity Microscopically, terahertz radiation-induced change of conductivity can take place due to changes in the carrier density n, e.g. by electron-hole pair generation due to direct interband transitions or light impact ionization, for the latter see Sec. 2.3. Apart from a variation of the carrier density, photoconductivity effects can also be induced by a change of the mobility $\Delta\mu$:

$$\Delta\sigma = |e| n \Delta\mu \tag{16}$$

Consequently, this type of photoconductivity is termed μ-photoconductivity. The change in mobility is mostly caused by electron gas heating induced by terahertz radiation and has been studied in various materials, e.g. InSb, GaAs, and Ge[32]. The heating process is outlined in more detail in the following.

When terahertz radiation is absorbed by free carriers a strong heating of the carrier occurs. With a carrier density n large enough, the electron-electron scattering time τ_{ee} is much shorter than the energy relaxation time τ_ε. Conse-

quently, absorption of terahertz radiation leads to an electron temperature T_e different from the lattice temperature T_lattice due to electron-electron scattering. The temperature T_e fulfills the balance equation for bulk materials [32]

$$\frac{K(\omega) I \varepsilon_\mathrm{eff}}{\hbar\omega} = \langle Q(T_\mathrm{e})\rangle n \,. \tag{17}$$

Here, $K(\omega)$ is the absorption coefficient, which is proportional to the concentration of free carriers n, ε_eff is the effective energy, which is released from an excited carrier to the system of electrons in equilibrium and $\langle Q\rangle = \langle d\varepsilon/dt\rangle$ denotes the energy losses per unit of time for one carrier.

For weak heating, the normalized change of the conductivity $\Delta\sigma/\sigma_0$ due to the change in mobility $\Delta\mu$ can be approximated by [32]

$$\frac{\Delta\sigma}{\sigma_0} = \frac{1}{\mu}\frac{\partial\mu}{\partial T_\mathrm{e}}\bigg|_{T_\mathrm{e}=T_\mathrm{lattice}} \Delta T_\mathrm{e}, \tag{18}$$

where σ_0 denotes the dark conductivity $\sigma_0 = |e|n\mu$. Eq. (18) shows that the sign of the μ-photoconductivity is determined by the sign of $\frac{\partial\mu}{\partial T_\mathrm{e}}$. This term is positive if, e.g., impurity scattering is the dominant scattering mechanism, while $\frac{\partial\mu}{\partial T_\mathrm{e}}$ is negative in the regime of scattering by phonons [66, 67]. The response time of μ-photoconductivity corresponds to the energy relaxation time τ_ε which typically is in the range of picoseconds to nanoseconds, being much shorter than the pulse duration used in this work ($\approx 100\,\mathrm{ns}$). Due to the fast kinetics of μ-photoconductivity, this effect is also used in fast terahertz radiation detectors [68–71].

Note that the application of highly intense radiation can also affect the lattice temperature T_lattice. The time scale of lattice-involving photoconductivity processes is usually longer than microseconds and, consequently, can be distinguished from the fast kinetics of electron-temperature driven processes. Furthermore, despite the high radiation pulse intensity used in this work, the corresponding pulse energy is rather small, making lattice heating a negligible factor.

2.3 Impact ionization in semiconductors

Because of its role in lightnings during thunderstorms impact ionization of gases caused by a dc electric field is one of the most popular effects present in

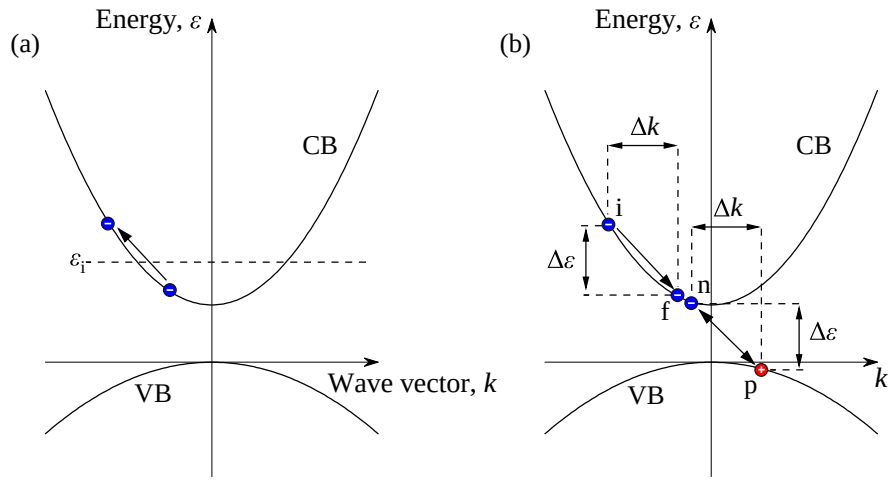

Figure 8: Panel (a) Sketch of a conduction band electron acquiring an energy larger than the threshold for impact ionization. Panel (b): Sketch of the impact ionization process: The electron (i) with $\varepsilon > \varepsilon_\mathrm{i}$ generates an electron-hole pair (n and p) due to a collision with a valence band electron and arrives in the state (f) after the collision. As indicated by the dashed lines, energy and momentum conservation laws have to be fulfilled in this process. Figure adapted from Ref. [72].

nature [32]. In semiconductors, the band-to-band impact ionization process as well as the impact ionization of impurities are also one of the most important carrier multiplication processes [32]. Moreover, impact ionization mechanisms are a central part of this work. In the following, the principle of the impact ionization process is exemplarily sketched on the simplified example of a semiconductor in an external dc electric field E_dc considering a one-dimensional model [67] and the corresponding impact ionization rate W is deduced. At an external field strength high enough, a conduction band electron can acquire an energy high enough to generate an electron-hole pair due to a collision process. In the following, this ionization threshold energy is termed ε_i. The aforementioned collision process is sketched in Fig. 8(b). The electron (i) with $\varepsilon > \varepsilon_\mathrm{i}$ collides with a valence band electron and arrives at (f) generating an electron-hole pair (n and p). Note that energy and momentum conservation law have to be fulfilled in this process [67, 73]:

$$m_n v_i^2/2 = m_n v_f^2/2 + m_n v_n^2/2 + m_p v_p^2/2 + \varepsilon_\mathrm{g} \tag{19}$$

$$m_n v_i = m_n v_f + m_n v_n + m_p v_p \,. \tag{20}$$

Here, m_n and m_p are the effective masses of electron and hole, respectively, v_i and v_f are the initial and final velocity of the electron, and v_n and v_p are the velocities of generated electron and hole, as indicated in Fig. 8(b). For equal velocities of all involved particles, i.e., $v_f = v_n = v_p$, the minimum kinetic energy for such an impact ionization process can be calculated from Eqs. (19) and (20):

$$\varepsilon_{\mathrm{i}} = m_n v_i^2/2 = \frac{2m_n + m_p}{m_n + m_p}\varepsilon_{\mathrm{g}} \tag{21}$$

According to Eq. (21), the value of the threshold energy ε_{i} ranges between ε_{g} and $2\varepsilon_{\mathrm{g}}$, depending on the effective masses. The rate of impact ionization W is dependent on the number of carriers with an energy above that ionization threshold ε_{i}. In a non-degenerate electron gas, the number of carriers with $\varepsilon > \varepsilon_{\mathrm{i}}$ is proportional to the exponential factor

$$W \propto \exp\left(-\frac{\varepsilon_{\mathrm{i}}}{k_{\mathrm{B}} T_e}\right), \tag{22}$$

where k_{B} is the Boltzmann constant and T_e is the electron temperature. The electron temperature can be determined from the energy balance equation, which has the form [67]

$$eE_{\mathrm{dc}} v_d = \frac{3}{2}\frac{k_{\mathrm{B}}(T_e - T)}{\tau_\varepsilon}, \tag{23}$$

where v_d is the electron drift velocity and τ_ε is the energy relaxation time. Assuming $T_e \gg T$ and neglecting the factor 3/2, the energy balance equation Eq. (23) can be simplified to

$$eE_{\mathrm{dc}} v_d \approx \frac{k_{\mathrm{B}} T_e}{\tau_\varepsilon} \tag{24}$$

and, consequently,

$$k_{\mathrm{B}} T_e \approx eE_{\mathrm{dc}} v_d \tau_\varepsilon = eE_{\mathrm{dc}} l \tag{25}$$

where l is the mean free path assuming dominant optical phonon emission with $l = v_d \tau_\varepsilon$ and considering τ_ε as constant. The ionization rate from Eq. (22) can

then be written as

$$W \propto \exp\left(-\frac{\varepsilon_\mathrm{i}}{eE_\mathrm{dc}l}\right) . \tag{26}$$

Note that the dependence of the ionization rate on the electric field $W \propto \exp(-E_\mathrm{dc}^{-1})$ suggested by Eq. (26) is only valid assuming that $v_d\tau_\varepsilon$ is independent on the electric field.

Note that at a sufficiently high electric field, the generated electron, see (n) in Fig. 8(b), has still an energy $\varepsilon > \varepsilon_\mathrm{i}$ and can again initiate an impact ionization process rather than recombining with a hole (p). Consequently, subsequent impact ionization processes lead to an exponential rise of the generated electron-hole pairs. This form of carrier multiplication is then termed avalanche breakdown and is the key working principle, e.g., for the generation of microwaves in impact ionization avalanche transit time (IMPATT) diodes [32, 67, 74].

Note that the inverse process to impact ionization, the Auger recombination, is also a very important process in semiconductors. Here, an electron-hole pair recombines by transferring the energy released by the recombination process to another electron [72, 74]. This process is a limiting mechanism for the carrier lifetime and one of the most important nonradiative recombination processes. Since the probability for this process increases with decreasing the band gap due to energy-momentum conservation, the Auger recombination is, e.g., an important limiting factor for efficiency of long-wavelength semiconductor lasers [72].

Light Impact Ionization Besides the aforementioned impact ionization in dc electric fields, the impact ionization process is also possible in ac fields. Since high-power lasers have been available, the phenomenon of impact ionization has been shown to be possible in gases and dielectrics even due to the high-frequency ac electric fields of visible radiation [75–77]. Furthermore, the effect was also observed in various two- and three-dimensional semiconductor systems and excited by several radiation sources [25–31, 78]. If excited by the electromagnetic field of radiation the phenomenon is termed *light* impact ionization [33, 79]. The study of light impact ionization induced by the ac electric field of intense terahertz radiation in low-dimensional semiconductor structures is a central part of this work. In most cases, the light impact ionization rate is determined by obtaining the probability, that an electron acquires

the energy ε_i needed to generate an electron-hole pair. As stated in the previous section, this threshold energy depends on the band gap and the effective masses of the involved particles due to energy and momentum conservation laws, see Eq. (21). Typically, the energy ε acquired by the electrons due to electron gas heating in the radiation electric field E, see also Sec. 2.2.3, is limited mainly due to the energy losses on phonon scattering. Impact ionization processes induced by an ac field are classified in two regimes depending on the value $\omega\tau$, where ω is the radiation angular frequency and τ is the momentum relaxation time.

On the one hand, the regime with $\omega\tau \ll 1$ is termed the quasi-static regime. Here, the charge carriers acquire the threshold energy ε_i in half of the period of the electric field without a single collision. In this regime an increase of the mean free path l results in an increase of carriers with an energy $\varepsilon \geq \varepsilon_\mathrm{i}$. It has been shown that in this regime the ionization rate W is proportional to [32, 34]

$$W \propto \exp\left(-\frac{\varepsilon_\mathrm{i}}{eEl}\right) , \tag{27}$$

where E is the radiation electric field. The term eEl describes the energy, which an electron obtains between two collision events.

On the other hand, for $\omega\tau \gg 1$ a system is in the high-frequency regime. Considering the electric field of radiation in the terahertz range as a driving force for the impact ionization, this regime is typically valid. In contrast to dc impact ionization or the quasi-static regime, the high-frequency regime has only been addressed in few works [25–31, 78].

In this regime, electrons do not follow the electric field any more due to multiple collisions and, consequently, can acquire much higher energies than if no collisions were considered in the energy acquisition process [32, 80]. Thus, in contrast to the quasi-static and dc case, the increase of the mean free path l results in a decrease of the energy acquired by the electrons and, consequently, a reduction of the impact ionization rate. It has been shown that the impact ionization rate W in this regime is described by [32, 34, 79]

$$W \propto \exp\left(-\frac{E_0^2}{E^2}\right) , \tag{28}$$

where the parameter E_0 is termed characteristic electric field. Note that the band-to-band light impact ionization process results in electron-hole pair gen-

eration, despite the fact that the corresponding photon energy can be much smaller than the energy gap. It has been shown that the characteristic electric field E_0 is proportional to the radiation angular frequency ω, i.e., the impact ionization probability decreases with increasing frequency [32, 33].

3 Methods

3.1 Investigated samples

3.1.1 HgTe/CdHgTe quantum wells

In order to investigate light impact ionization in semiconductors with different band structures, HgTe/CdHgTe QWs were used. These samples were prepared and grown in the group of Dr. Sergey Dvoretsky and Dr. Sergey Mikhailov in the A.V. Rzhanov Institute of Semiconductor Physics, Novosibirsk, Russia.

As depicted in Sec. 2.1.2, band ordering and structure in HgTe/CdHgTe QWs crucially depend on the HgTe layer thickness [11]. In this thesis two samples with the HgTe QW layer thickness of 5.7 nm (wafer #E) and 6.6 nm (wafer #F) were used. The samples were grown by molecular beam epitaxy on (013) (wafer #E) and (001) (wafer #F) oriented GaAs substrates in similar manner as depicted in Ref. [3]. The GaAs substrates were covered with 30 nm thick ZnTe layers and 4 µm thick CdTe layers in order to completely relax the strain caused by the lattice mismatch between HgTe and the GaAs substrates.

The QW barriers were made of $Cd_xHg_{1-x}Te$ with a Cd concentration $x = 0.6$ and a thickness of $d_{\mathrm{barrier}} = 30\,\mathrm{nm}$ for wafer #E and $x = 0.7$ and $d_{\mathrm{barrier}} = 39\,\mathrm{nm}$ for wafer #F, respectively. Cross-sections of both samples are shown in Fig. 9(a) and 9(c).

The layer compositions described above result in the band structures calculated by Dr. Grigory Budkin from the Ioffe Institute in St. Petersburg, Russia shown in Fig. 9(b) and 9(d) for wafer #E and wafer #F, respectively. While wafer #E has a parabolic dispersion with a band gap of $\varepsilon_{\mathrm{g}} = 17.6\,\mathrm{meV}$, the dispersion of wafer #F is nearly linear around $k = 0$ with a much smaller band gap of $\varepsilon_{\mathrm{g}} = 4.5\,\mathrm{meV}$. In both samples the Fermi energy ε_{F} is much higher than the band gap, with $\varepsilon_{\mathrm{F}} = 54\,\mathrm{meV}$ for sample wafer #E and $\varepsilon_{\mathrm{F}} \approx 60\,\mathrm{meV}$ for wafer #F.

In this work, square-shaped Van-der-Pauw geometry samples with a size of $5{\times}5\,\mathrm{mm}^2$ were used to study the photoresponse, see Fig. 10(a). In order to make this possible, six ohmic contacts, four at the edges and two at the middle of opposite edges were fabricated by indium soldering and numbered counter-clockwise, see Fig. 10(b). Also, Hall bar structures with a semitransparent gate were produced from wafer #E in order to study the Fermi level dependence of measured signals. The $200 \times 450\,\mu\mathrm{m}^2$ Hall bars were modeled using photolithography and Br-based wet etching [81]. 30 nm SiO_2 and

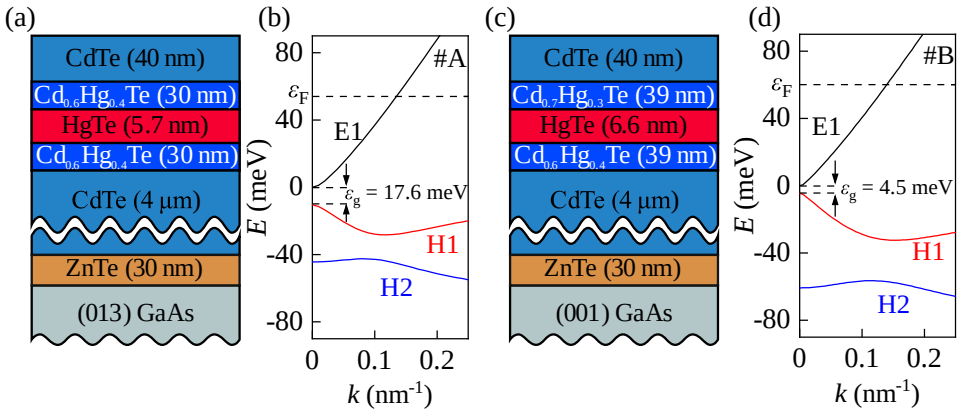

Figure 9: Layer compositions and energy dispersion calculated by G. Budkin (Ioffe Institute, St. Petersburg, Russia) for HgTe QW wafer #E (Panels (a) and (b)) and wafer #F (Panels (c) and (d)), respectively. Figures adapted from [35, 36]

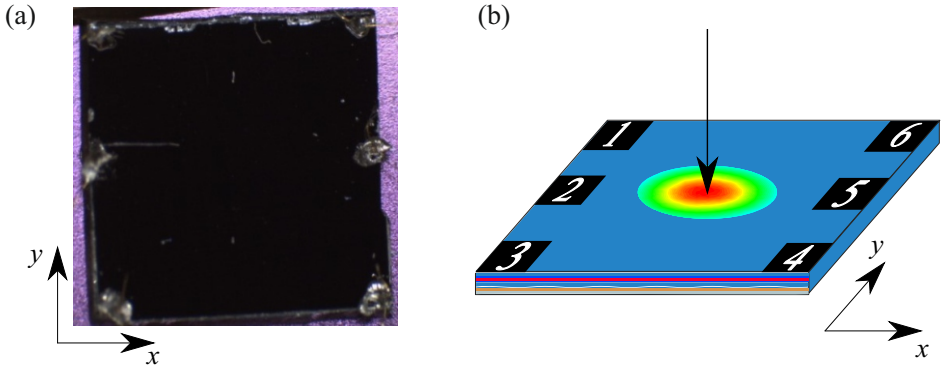

Figure 10: Panel (a): Photograph (top view) of the HgTe QW sample from wafer #E with Cartesian coordinates x, y. Panel (b): Sketch of the sample geometry with contact numbers and Cartesian coordinates x, y. Panel (b) adapted from [36].

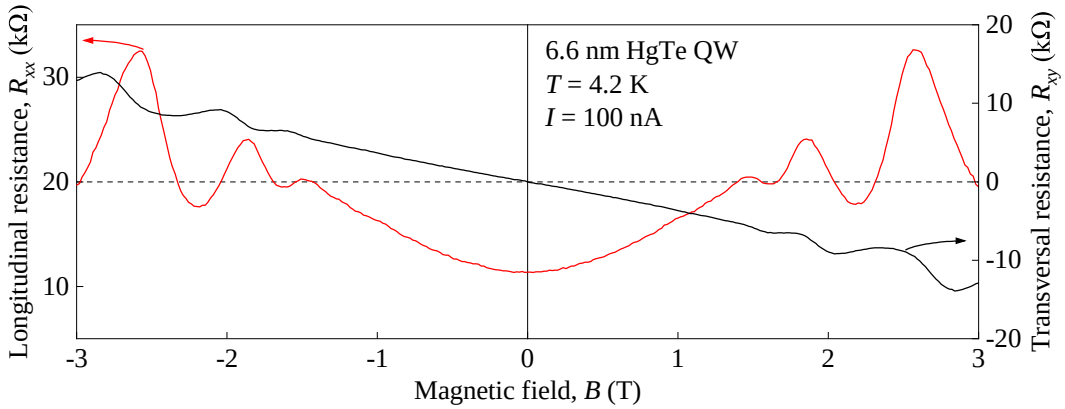

Figure 11: Typical magnetotransport measurement at $T = 4.2\,\mathrm{K}$ for a sample from HgTe QW wafer #F in van-der-Pauw geometry. The red curve shows the longitudinal resistance R_{xx} exhibiting Shubnikov-de Haas oscillations, while the black curve shows the transversal resistance R_{xy}. Figure adapted from [36]

100 nm Al_2O_3 were used as an insulating oxide layer between the Ti/Au gate electrode and the sample. Magnetotransport measurements done for sample characterization at the temperature $T = 4.2\,\mathrm{K}$ revealed carrier densities n and mobilities μ being $n = 3 \times 10^{11}\,\mathrm{cm}^{-2}$ and $\mu = 2.5 \times 10^4\,\mathrm{cm}^2/\mathrm{Vs}$ for wafer #E, and $n = 1.7 \times 10^{11}\,\mathrm{cm}^{-2}$ and $\mu = 5.7 \times 10^3\,\mathrm{cm}^2/\mathrm{Vs}$ for wafer #F, respectively. A typical magnetotransport measurement is exemplarily shown in Fig. 11 for a sample from wafer #F in van-der-Pauw geometry.

3.1.2 $Cd_xHg_{1-x}Te$ films

Another HgTe-based material system studied in this thesis are $Cd_xHg_{1-x}Te$ films. Similarly to the HgTe QWs, these structures have also been grown by the group of Dr. Sergey Dvoretsky and Dr. Sergey Mikhailov in the A.V. Rzhanov institute of Semiconductor Physics, Novosibirsk, Russia.

These samples were grown on top of (013) GaAs substrates. 30 nm ZnTe and 6 µm CdTe were used as intermediate layers between the substrate and the $Cd_xHg_{1-x}Te$ film in order to obtain the crystal quality for the growth of CdHgTe on top [83–87]. A sketch of the layer structure is shown in Fig. 12(a). Square-shaped samples with an approximate size of $5 \times 5\,\mathrm{mm}^2$ were used and contacts were fabricated by indium soldering at the sample edges and in the middle of opposite edges.

As described in Sec. 2.1.3 the Cd concentration is a crucial factor determining the properties of $Cd_xHg_{1-x}Te$. In this thesis, the experiments on

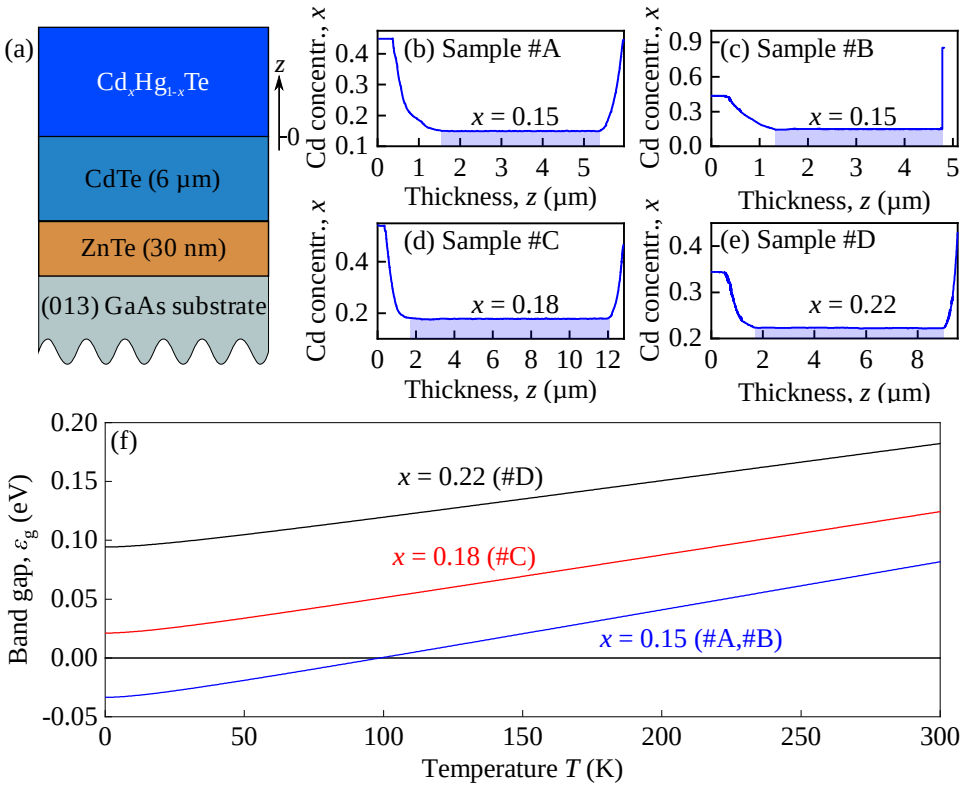

Figure 12: Panel (a) Sketch of the sample layer structure of the used $Cd_xHg_{1-x}Te$ films. The $Cd_xHg_{1-x}Te$ films are grown on a (013) GaAs substrate with a CdTe and a ZnTe layer in between in order to relax strain stemming from the lattice mismatch between CdHgTe and GaAs and, consequently, to reach the desired crystal quality. Panels (b)-(e): Cd content in the epitaxially grown layer for samples #A-#D as a function of the thickness z starting from the end of the intermediate CdTe layer, respectively. Figures adapted from [82]. Panel (f): Dependence of the band gap energy ε_g in $Cd_xHg_{1-x}Te$ on the temperature T for Cd concentrations x of 0.15, 0.18 and 0.22 corresponding to the samples used in this work. The data is calculated according to Refs. [18, 19]. Note that samples #A and #B ($x = 0.15$) exhibit a negative band gap at liquid helium temperature and, hence, the bands are inverted.

$Cd_xHg_{1-x}Te$ films were conducted on four different samples with Cd concentrations of $x = 0.15$ (Samples #A and #B) $x = 0.18$ (Sample #C) and $x = 0.22$ (Sample #D). In samples #A, #C, and #D the active layer with a constant Cd concentration $x = 0.15$, $x = 0.18$ and $x = 0.22$, respectively, was surrounded by regions with growing Cd concentration. This is sketched in Fig. 12(b),(d) and (e), where the Cd concentration x is shown as a function of the growth direction z. In contrast, Sample #B with $x = 0.15$ was capped by 30 nm $Cd_{0.85}Hg_{0.15}Te$ and, consequently, lacks the gradual increase of Cd concentration on the top. Note that the width $d_{\text{conduction}}q$ of the conduction

channel with constant Cd concentration is in the range of several micrometers in all samples. The actual set of samples allows access to different properties of $Cd_xHg_{1-x}Te$ films, which can be characterized by the band gap energy ε_g. Figure 12(f) shows the temperature dependence of the band gap energy ε_g on the temperature T calculated according to Ref. [18] for the Cd concentrations x relevant to samples #A to #D. While the band gap is positive in the whole temperature range for samples #C and #D, ε_g changes its sign for #A and #B at $T \approx 100\,\mathrm{K}$. The negative band gap for $\varepsilon_g \lessapprox 100\,\mathrm{K}$ indicates an inverted band ordering and, thus, formation of topological surface states [19]. In sample #C, the band gap is close to zero for liquid helium temperature, which implies that the energy dispersion is almost linear under this condition.

3.2 Measurement technique

In this chapter a brief description of the THz radiation sources, the optical setup, and the electronics used for the detection of photocurrent and photoconductivity is given.

3.2.1 Sources of terahertz laser radiation

For the illumination of samples, two types of THz radiation sources were used in this work: On the one hand a pulsed molecular gas THz laser and on the other hand a cw molecular gas THz laser [32, 88]. Both lasers are pumped by corresponding CO_2 lasers: For the pulsed THz laser a pulsed transversely-excited atmospheric pressure (TEA) CO_2 laser with a pulse duration of 100 ns and peak pulse powers up to megawatts was used as a pump source. For the cw THz laser, however, a longitudinally excited cw CO_2 laser with a power of $\approx 50\,\mathrm{W}$ was used. In both cases the CO_2 pump laser radiation is tunable in the frequency range from approx. 27 to 33 THz. The pump radiation is coupled into a resonator filled with molecular gas, where vibrational-rotational transitions are excited and the rotational relaxation transitions are used to emit laser radiation in the THz range. Note that some lines of the pulsed THz laser are based on stimulated Raman scattering and a permanent electric dipole moment in the gas molecule is essential for these lines [32, 89]. With both THz laser systems several frequency lines between 0.6 and 8.5 THz can be emitted, while the used molecular gases are NH_3, CH_3OH, CH_3F,CH_2F_2, D_2O and CH_2O_2. Hereby, the accessible frequency lines are determined by the molecule weight, i.e. heavier molecules generate radiation with lower frequency. This is

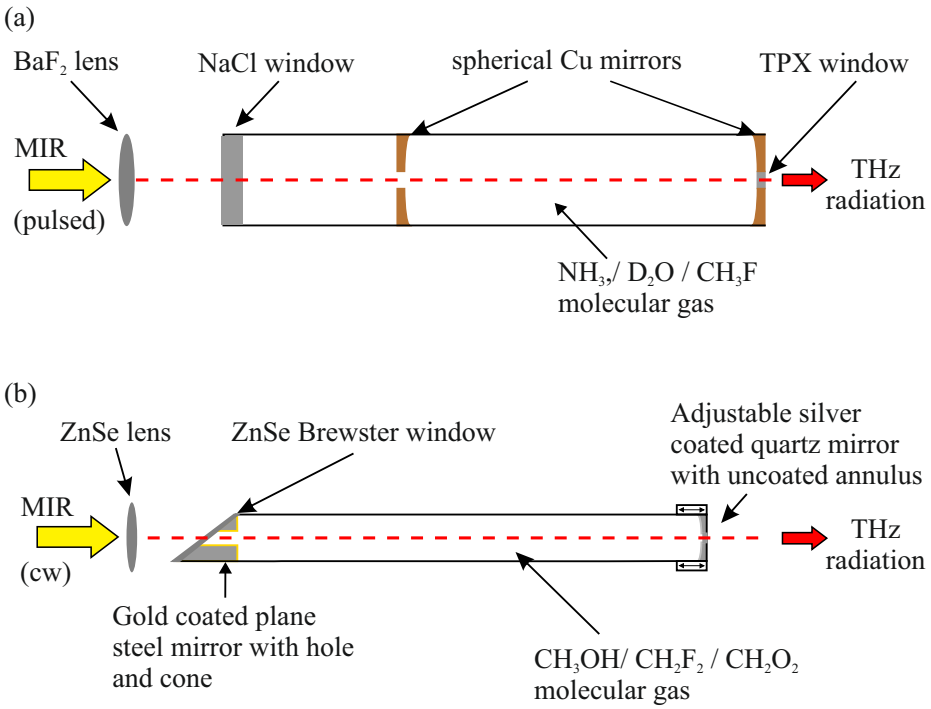

Figure 13: Sketch of the laser resonators for the pulsed (Panel (a)) and the cw (Panel (b)) THz laser. Adapted from [92]

because the rotational levels get closer for heavier molecules [90]. In both cases, the transversal beam profile is Gaussian as checked by a pyroelectric camera [91] and the frequency-dependent focused beam diameter d_{beam} defined as the full width at half maximum of power is between is between 1.5 and 3.5 mm full width at half maximum. While the working principle described above holds for both, the pulsed and the cw THz laser, the differences of both systems are pointed out in the following paragraphs.

Pulsed molecular THz laser In the pulsed THz laser the mid-infrared pulses from the TEA-CO_2 laser are coupled into the molecular gas-filled resonator by focusing the radiation via a BaF_2 lens through a NaCl window. The resonator consists of a glass cylinder with gold-coated spherical Cu mirrors with an in/outcoupling hole in the middle, see Fig. 13(a). On the output side, a TPX (poly-4-methyl-1-penthen) window ensures absorption of the remaining mid-infrared radiation stemming from the CO_2 laser, while being transparent for THz radiation. The pulsed THz laser emits pulses with a duration of ≈ 100 ns with a frequency-line-dependent peak power in the range of several tens of kW, measured by photon drag detectors [93].

cw molecular THz laser On the other hand, in the cw molecular THz laser, the radiation stemming from a cw CO_2 laser is focused into the resonator via a ZnSe lens through a ZnSe Brewster window and the cone of a gold coated plane steel mirror, see Fig. 13(b). The resonator length in this type of THz laser can be varied by changing the position of a silver coated dielectric z-cut quartz mirror, which allows to control the mode structure and wavelength emitted by the laser. An uncoated central z-cut quartz annulus acts as an outcoupling transmission window for THz radiation. The cw THz laser emits radiation with a power between 20 and 80 mW.

3.2.2 Experimental setup

In the following section the optical setups to modify THz radiation as well as the electronic setup to detect THz radiation-induced photocurrents and photoconductivity are outlined.

Manipulation of radiation intensity The radiation intensity was controlled by a crossed linear polarizer setup. The initially linearly polarized THz laser beam passes a rotatable first polarizer P_1, while the angle between the transmission direction of the polarizer and the electric field of the linearly polarized emitted laser radiation is termed β. According to Malus' law, the radiation intensity I_1 after passing the polarizer rotated by the angle β is then described by

$$I_1 = I_0 \cos^2(\beta), \tag{29}$$

while I_0 denotes the initial intensity of the emitted radiation. After passing the polarizer P_1, the radiation passes a second polarizer P_2, whose transmission direction is fixed and parallel to the linear polarization of the initially emitted laser radiation. This is done to ensure a fixed polarization at the output of the polarizer setup. The radiation intensity I_2 after passing both polarizers P_1 and P_2 is the described by

$$I_2 = I_0 \cos^2(\beta) \cdot \cos^2(-\beta) = I_0 \cos^4(\beta) \tag{30}$$

Manipulation of Radiation Polarization In order to modify the radiation polarization, waveplates or grid linear polarizer are used. In experiments with elliptically polarized light, the initially linearly polarized radiation was manipu-

lated using rotatable quarter-wave plates made from x-cut crystal quartz. The rotation angle of the quarter-wave plates is termed φ, while the polarization remains unchanged for $\varphi = 0, 90°$ and 180°. For the quarter-wave plate's rotation angles $\varphi = 45°$ and 135° the output polarization is right- or left-handed circularly polarized, respectively. In the case of a rotating quarter-wave plate, the Stokes parameters are varied according to

$$P_{\mathrm{L1}}(\varphi) = (\cos(4\varphi) + 1)/2, \quad P_{\mathrm{L2}}(\varphi) = \sin(4\varphi)/2, \quad P_{\mathrm{circ}}(\varphi) = \sin(2\varphi), \tag{31}$$

while P_{L1} and P_{L2} define the degree of linear polarization and P_{circ} defines the degree of circular polarization. Note that the quarter-wave plate rotation angle is also referred to as phase angle in this work.

In experiments with rotation of the linear polarization, this was achieved either by the rotation of half-wave plates or by the rotation of a linear polarizer placed behind a quarter-wave plate at $\varphi = 45°$ providing circularly polarized radiation. The rotation angle of the linear polarization is termed azimuth angle α. Rotating the linear polarization, the corresponding Stokes parameter are varied according to

$$P_{\mathrm{L1}}(\alpha) = \cos(2\alpha), \quad P_{\mathrm{L2}}(\alpha) = \sin(2\alpha). \tag{32}$$

Note that the rotation angle of linear polarization α is also referred to as azimuth angle in this work.

Calibration of Radiation Intensity In order to monitor the laser intensity acting on the sample during the measurement a thin Mylar sheet was inserted in the optical path acting as a beam splitter. The reflected radiation was then focused onto a reference power detector, while the transmitted part is used to illuminate the sample. By conducting calibration measurements with a second detector at the sample position, see exemplary sketch in Fig. 14, the wavelength and setup-dependent ratio between reflected and transmitted radiation power could be determined and, thus, the reference detector signal could be matched with the radiation power coming onto the sample. By measuring the spatial beam profile with a pyroelectric camera the beam spot diameter could be determined and, consequently, the radiation power P could be recalculated to

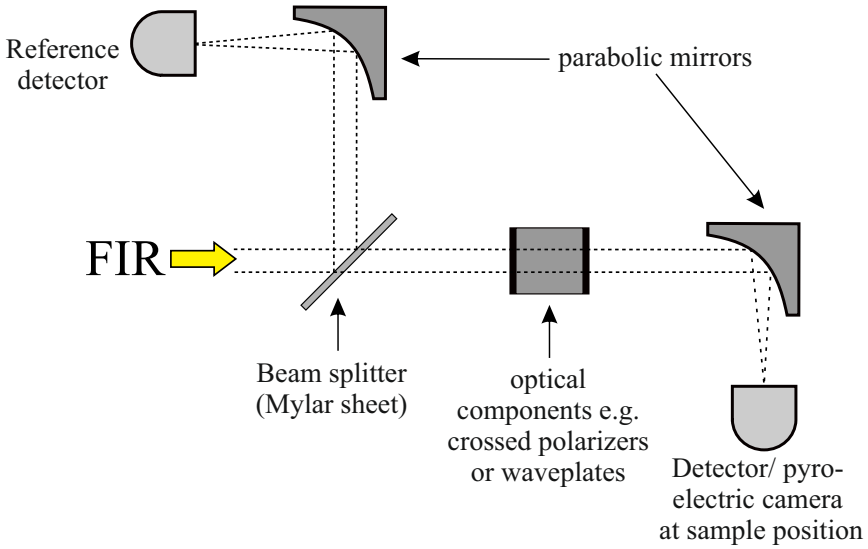

Figure 14: Exemplary sketch of the setup for a calibration measurement. Adapted from [92].

the corresponding intensity I. This was done by

$$I = \frac{P}{\pi \cdot d_x \cdot d_y} = \frac{P}{A_{\text{beam}}}, \tag{33}$$

where d_x and d_y are the full width at half maximum values for the Gaussian spatial beam profiles in x and y-directions, respectively, and A_{beam} is the beam diameter. A typical beam profile is shown for the frequency of $f = 0.6\,\text{THz}$ in Fig. 15(b).

Measurement Configurations After passing the beam splitter and the optical components used for radiation state manipulation, the THz radiation originating either from the pulsed or the cw THz laser, see Sec. 3.2.1, is focused onto the sample in a cryostat using parabolic mirrors. A sketch of an exemplary setup is shown in Fig. 15(a). In all measurements the samples were illuminated under normal incidence. In this thesis three types of cryostats were used: On the one hand a temperature-variable cold finger and a liquid helium flow cryostat were used for measurements without magnetic field, on the other hand a helium bath cryostat with a superconducting magnet was used being able to provide magnetic fields up to $\pm 7\,\text{T}$. Using these types of cryostats it was possible to address a broad temperature range from room temperature to $\approx 2\,\text{K}$.

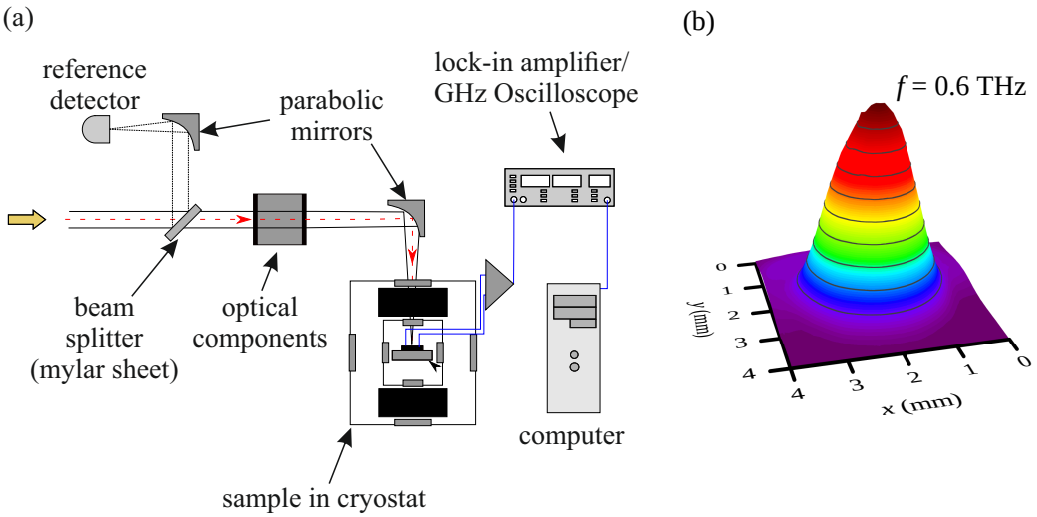

Figure 15: Panel (a): Sketch of the measurement setup. Note that for the cw laser a chopper was part of the optical components and the lock-in amplifier was used, while in the pulsed laser setup the GHz oscilloscope was used. Adapted from [94]. Panel (b): Typical beam profile measured by a pyroelectric camera for the frequency of $f = 0.6\,\mathrm{THz}$.

Electronic setup The components in the experimental setup are connected with a computer via GPIB (General Purpose Interface Bus), USB, or the parallel printer port. The optical components like e.g. waveplates were rotated using step motors. In the pulsed laser setup the photosignals are amplified and then processed by a digital storage oscilloscope. On the contrary in the cw system the laser radiation is chopped optically in order to use standard lock-in technique for the signal processing.

All THz-induced photosignals were measured as a voltage drop over a load resistor R_L or directly over the sample and are amplified using low-noise preamplifiers. The voltage drop was detected by a GHz digital storage oscilloscope (pulsed laser) or lock-in technique (cw laser). For photocurrent measurements no external bias was applied and the measured voltage U is proportional to the photocurrent J. For the photoconductivity measurements, in contrast, a dc bias of $\pm 300\,\mathrm{mV}$ was applied to the sample.

In order to eliminate the contribution of the photocurrent in the photoconductivity measurements the signal was measured for two bias polarities ($\pm 300\,\mathrm{mV}$) and the bias-independent photocurrent was eliminated by subtracting the signals for both polarities and dividing by two. From the obtained photoconductivity signal, the relative photoinduced change of conductivity $\Delta\sigma/\sigma$ was calculated.

4 Impact ionization induced by terahertz radiation in HgTe quantum wells

In this chapter the results regarding terahertz-radiation induced impact ionization in HgTe QWs are presented and discussed. Starting with the findings for the sample with parabolic dispersion, the obtained photocurrents are outlined first, followed by the photoconductivity data, the results for the sample with almost linear dispersion, and a subsequent discussion. All results in this section are obtained using the pulsed terahertz laser (see Sec. 3.2.1).

4.1 Nonlinearities in HgTe quantum wells below the critical thickness

The description of the results in terms of impact ionization in HgTe QWs starts with the 5.7 nm wide QW (wafer #E), which exhibits a parabolic dispersion, see Fig. 9.

4.1.1 Photocurrent

Firstly, the photocurrent data are outlined. Illumination of the bulk or the edges of the HgTe QW with linearly or circularly polarized radiation led to a complex photocurrent dynamics depending on the radiation intensity. In Fig. 16 the evolution of this photocurrent is shown exemplarily for a radiation frequency of $f = 0.6\,\mathrm{THz}$ and circularly polarized light: At low radiation intensities (Panel(b)) the photocurrent response just follows the reference laser pulse (Panel (a)) with a negative sign. Increasing the radiation intensity a change in the temporal shape was observed, see Fig. 16(c): At the maximum of the excitation pulse ($t = t_{\mathrm{max}}$, dashed vertical line), the photosignal rapidly drops to zero. Thereafter, the photocurrent rises again before it follows the excitation pulse and, consequently, vanishes. Increasing the radiation intensity further, the photocurrent changes its sign at a certain radiation intensity I_{inv} and, hence, becomes positive at $t = t_{\mathrm{max}}$. At intensities $I > I_{\mathrm{inv}}$, the positive signal contribution dominates the photoresponse, which is shown in Fig. 16(d-f).

This complicated photocurrent dynamic is caused by the change of the photocurrent sign with rising intensity: At the rising edge of the incident laser pulse the intensity consequently rises with the time t, which results in the

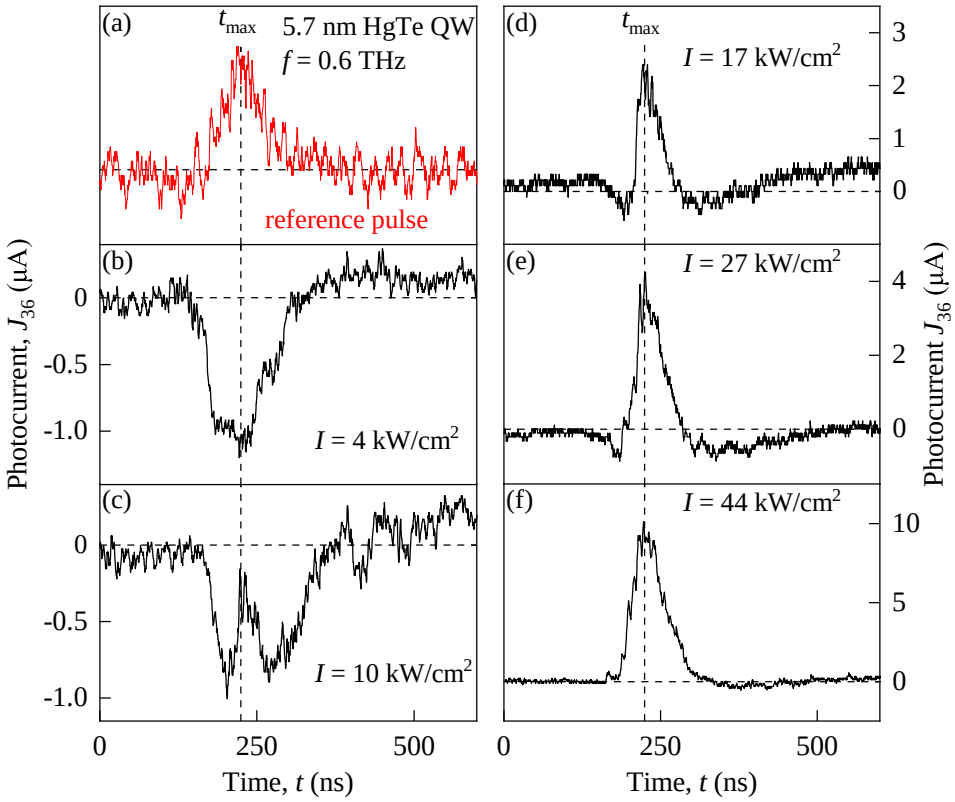

Figure 16: Panel (a): Temporal shape of a reference laser pulse in arbitrary units. The vertical dashed lines indicate the time t_{max} of the maximum of the excitation pulse. Panels (b-f): Temporal shape of the photocurrent excited by illumination of the center of a sample from wafer #E with right-handed circularly polarized radiation at different intensities with a frequency of $f = 0.6\,\mathrm{THz}$. The photocurrent was measured diagonally between contacts 3 and 6, see Fig. 10. At low intensities the photocurrent response almost follows the reference pulse with a negative amplitude, while at higher intensities a nonlinear positive contribution is observed resulting in a sign change at an intensity of approximately $10\,\mathrm{kW/cm^2}$. Adapted from Ref. [35].

dynamic photocurrent sign inversion. In contrast, at the falling edge of the incident laser pulse the intensity decreases and the photocurrent dynamic is roughly mirrored. Thus, the photocurrent peak emerges at $t = t_{max}$. Consequently, the presented photocurrent signals in the following plots are always recorded at $t = t_{max}$.

In further studies the helicity-dependence of the photocurrent described above was examined. In Fig. 17(a) the intensity dependence of the photocurrent signal recorded at $t = t_{max}$ is shown for right- and left-handed circular polarization of the incident radiation illuminating the sample edge. The data reveal that both polarization states result in a photocurrent sign inversion

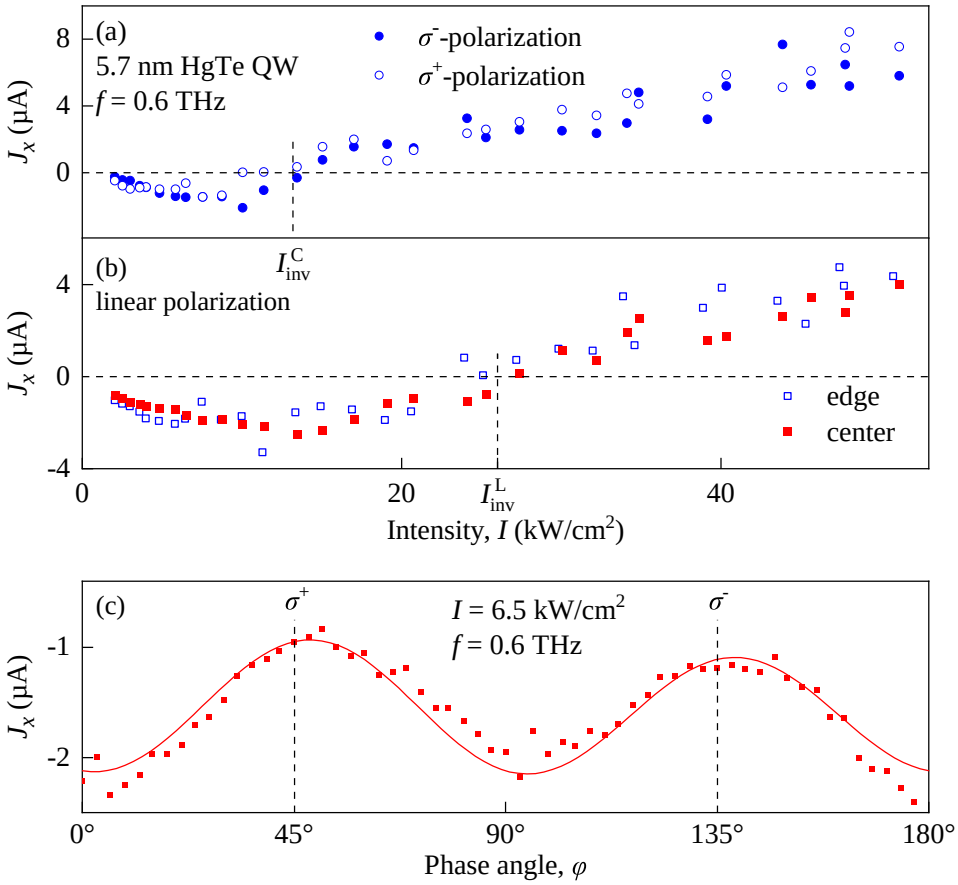

Figure 17: Panel (a): Intensity dependencies of the edge photocurrent excited by right-handed (open circles) and left-handed (full circles) circularly polarized radiation with a frequency of $f = 0.6\,\mathrm{THz}$ in a sample from Wafer #E. The photocurrent was measured between the edge contacts 1 and 6 while illuminating the corresponding sample edge, see Fig. 10. Panel (b): Intensity dependencies of the photocurrent at the edge (blue, picked up from contacts 1 and 6) and in the center (red, picked up from contacts 2 and 5) of a sample from wafer #E, see Fig. 10. The photocurrent was excited by linearly polarized radiation with a frequency of $f = 0.6\,\mathrm{THz}$ illuminating the sample center. Panel (c): Dependence of the photocurrent in the sample bulk on the rotation angle of the quarter-wave plate φ measured at the radiation intensity of $I = 6.5\,\mathrm{kW/cm^2}$ for the radiation frequency of $f = 0.6\,\mathrm{THz}$. The solid line shows a fit according to Eq. (34) with the fitting parameters $J_0 = -1.0\,\mu\mathrm{A}$, $J_1 = -1.1\,\mu\mathrm{A}$, $J_2 = -0.3\,\mu\mathrm{A}$, and $J_3 = 0.1\,\mu\mathrm{A}$. Adapted from Ref. [35].

at $I_{\mathrm{inv}}^{\mathrm{C}} = 15\,\mathrm{kW/cm^2}$. Moreover, almost no difference between the signals obtained for right- and left-handed circularly polarized radiation could be detected. This independence of the photocurrent on the radiation helicity is approved by the dependence of the photocurrent on the quarter-wave plate rotation angle φ for an intensity of $I = 6.5\,\mathrm{kW/cm^2}$ shown in Fig. 17(c). The

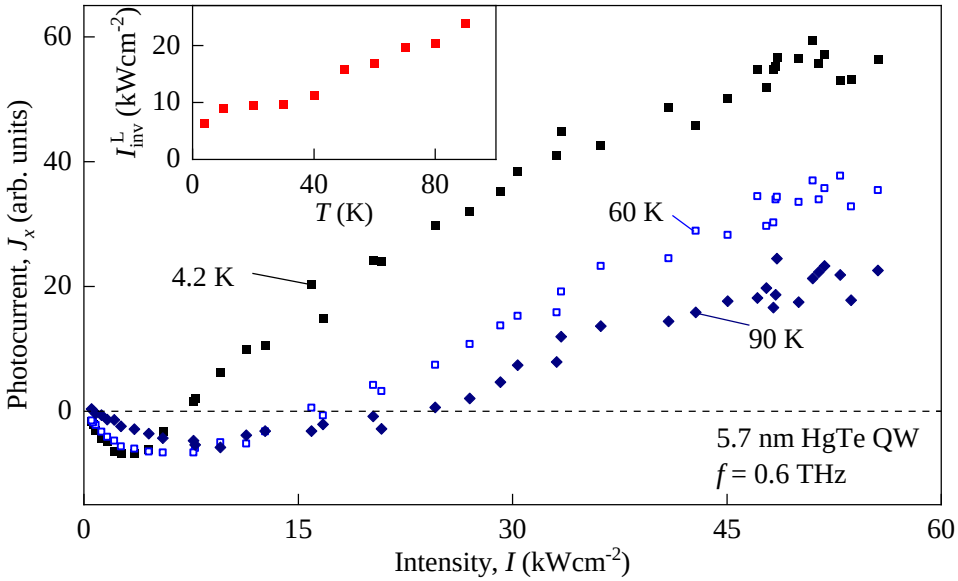

Figure 18: Intensity dependencies of the photocurrent excited by linearly polarized radiation with a frequency of $f = 0.6\,\mathrm{THz}$ for sample temperatures of $T = 4.2$, 60, and 90 K in a sample from wafer #E. The photocurrent was measured between the central contacts 2 and 5, see Fig. 10, while illuminating the sample center. The inset shows the intensity of sign inversion $I_{\mathrm{inv}}^{\mathrm{L}}$ as a function of the temperature dependence. Adapted from Ref. [35].

data is fitted according to

$$J_x = J_0 + J_1 P_{\mathrm{L1}}(\varphi) + J_2 P_{\mathrm{L2}}(\varphi) + J_3 P_{\mathrm{circ}}(\varphi)\,, \tag{34}$$

with the Stokes parameters defined in Eq. (31). Again, no difference between the photocurrents excited by right- and left-handed circularly polarized radiation could be measured. A qualitatively similar intensity dependence as for circularly polarized radiation was detected using linear polarization, see empty blue squares in Fig. 17(b). Here, the inversion intensity has a higher value $I_{\mathrm{inv}}^{\mathrm{L}} \approx 25\,\mathrm{kW/cm^2}$. Additionally the photocurrent was studied at temperatures T from 4.2 to 90 K. The corresponding intensity dependencies are shown in Fig. 18. The data reveal that the qualitative behavior of the photocurrent is retained at higher temperatures, while the inversion intensity rises with temperature, see also inset in Fig. 18.

The detected insensitivity to the radiation helicity excludes the generation of helical edge photocurrents as a driving force for the nonlinear photocurrent described above. Furthermore, comparing the photocurrent picked up across the sample obtained by illumination of the sample center and the photocurrent

picked up at the sample edges under the same conditions revealed no measurable difference. This comparison is done in Fig. 17(b) for photocurrents excited by linearly polarized radiation at the edges (blue empty squares) and in the sample center (red full squares). This demonstrates that the photocurrent is not even generated at the edges excluding edge mechanisms as the origin of the nonlinear photocurrent. Below in Sec. 4.3 it will be shown that the nonlinear photocurrent is caused by electron-hole pair generation due to light impact ionization. The evidence for this has been obtained in the measurements of the radiation-induced change of conductivity $\Delta\sigma/\sigma$ described in the next section.

4.1.2 Photoconductivity

A typical photoconductivity response pulse is illustrated in the inset of Fig. 19. For all measured frequencies a positive photoconductivity signal was observed and the pulse is twice times longer as compared with the photocurrent response, see Fig. 16. Since they are in line with the recombination time

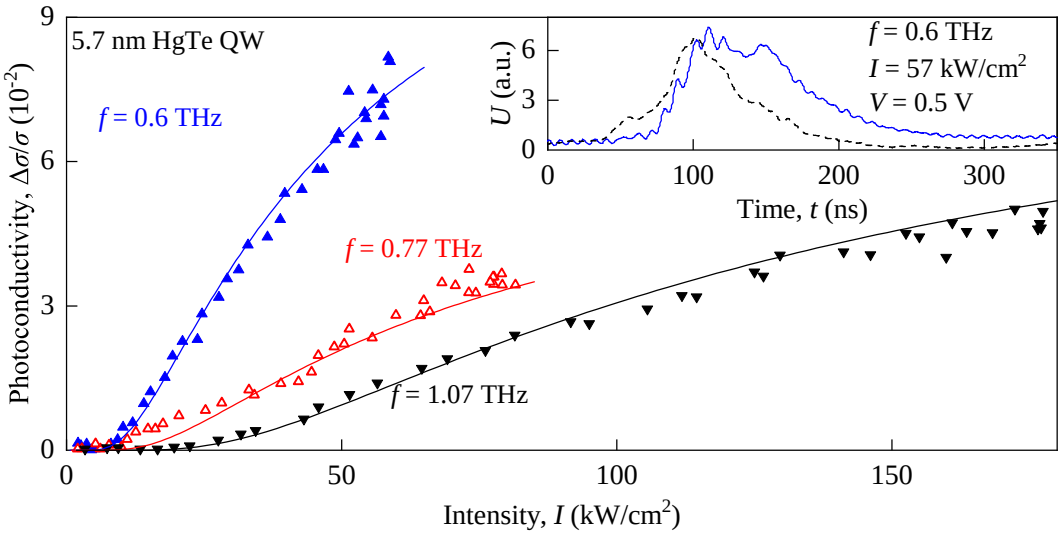

Figure 19: Dependencies of the normalized photoconductivity $\Delta\sigma/\sigma$ excited by linearly polarized radiation in the center of a sample from wafer #E for the radiation frequencies of 0.6 (blue triangles), 0.77 (red triangles), and 1.07 THz (black triangles) on the intensity I. The photoconductivity signal is picked up from the central contacts 2 and 5. The solid lines depict the corresponding fits according Eq. (35) with the fitting parameters A and I_0. The inset shows the temporal shape of an exemplary photoconductivity pulse (solid line) measured in the center of the samples using linearly polarized radiation with a frequency of 0.6 THz and an intensity of 57 kW/cm^2. The dashed line shows a reference laser pulse. Adapted from Ref. [35].

known for HgTe QWs [95], these corresponding response times together with the increase of conductivity indicate that this photoconductivity is caused by electron-hole pair generation despite the fact that the photon energy $\hbar\omega$ is much smaller than the band gap ε_g. Characteristic intensity dependencies of the photoconductivity $\Delta\sigma/\sigma$ are shown in Fig. 19 for three different frequencies of linear polarized radiation illuminating the sample center. The data show a superlinear raise of the photoconductivity, while the nonlinearity decreases by going to higher radiation frequencies. The data is fitted after

$$\frac{\Delta\sigma}{\sigma} = A \cdot \exp\left(-\frac{I_0}{I}\right) = A \cdot \exp\left(-\frac{E_0^2}{E^2}\right) , \tag{35}$$

with the coefficient A and the characteristic intensity I_0 as fitting parameters, the radiation electric field E, the radiation intensity $I = (E^2 \cdot n_\omega/2(Z_0))$, the characteristic electric field E_0, the vacuum impedance Z_0, and the refractive index n_ω. Measurements of the photoconductivity in the temperature range from 4.2 to 90 K revealed that an increase of the temperature leads to a decrease of the nonlinearity, which manifests in an increase of the characteristic

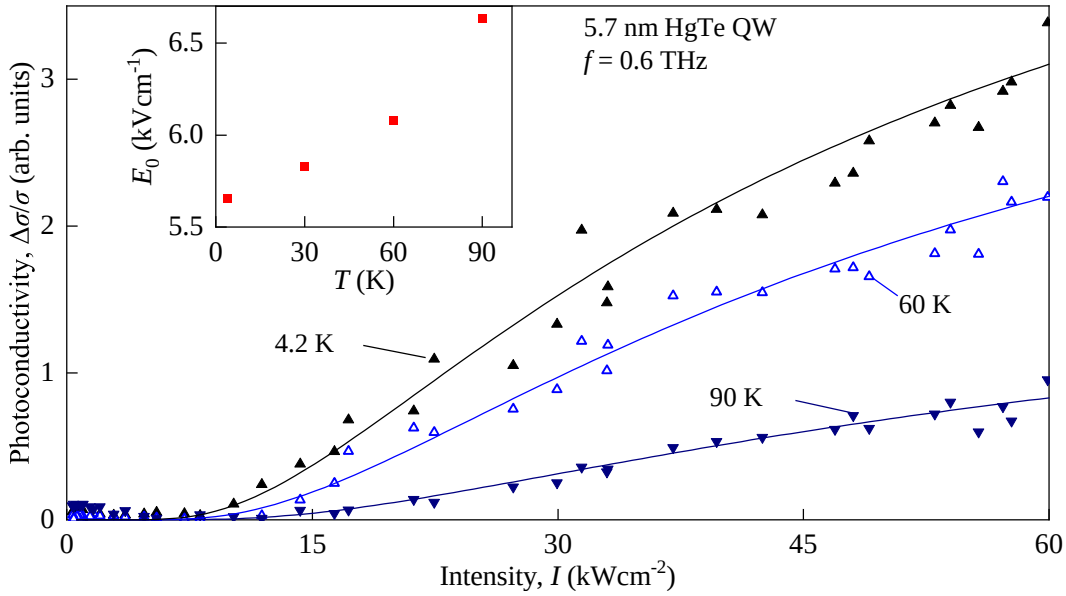

Figure 20: Intensity dependencies of the normalized photoconductivity $\Delta\sigma/\sigma$ excited by linearly polarized radiation with $f = 0.6$ THz in the center of a sample from wafer #E. The data were obtained for temperatures of $T = 4.2$, 60, and 90 K and the central contacts 2 and 5 were used, see Fig. 10. The solid lines show fits after Eq. (35) with the fitting parameters A and I_0. The inset shows the temperature dependence of the fitting parameter $E_0 \propto \sqrt{I_0}$. Adapted from Ref. [35].

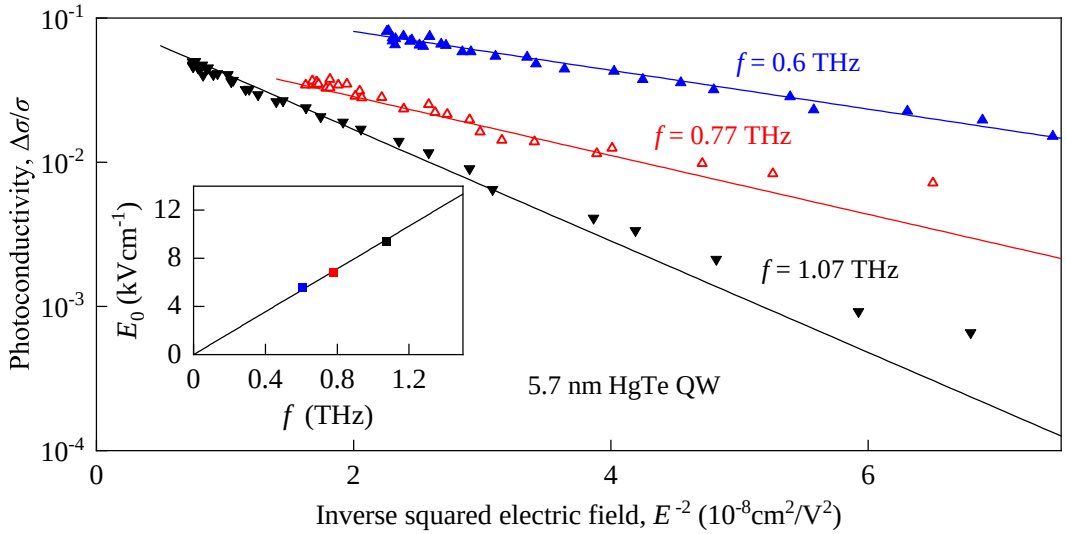

Figure 21: Half-logarithmic plot of the normalized photoconductivity $\Delta\sigma/\sigma$ induced by linearly polarized radiation in the center of a sample from wafer #E as a function of the inverse squared radiation electric field E^{-2}. The presented data for the radiation frequencies of 0.6 (blue triangles), 0.77 (red triangles), and 1.07 THz (black triangles) is the same as for Fig. 21. Solid lines depict fits after Eq. (35) [see also theoretical Eqs. (51) and (52).] using A and E_0 as fitting parameters. The inset shows the fitting parameter E_0 extracted from the corresponding fits from panel (a) as a function of the radiation frequency f. Adapted from Ref. [35].

electric field E_0, see main figure and inset in Fig. 20. Replotting the data from Fig. 19 in a half-logarithmic scale as a function of the inverse squared electric field $E^{-2} \propto I^{-1}$ yields that the data are well described by Eq. (35) especially for high radiation intensities, i.e. low E^{-2}, see Fig. 21. At low intensities, however a deviation is seen, which is attributed to a contribution of μ-photoconductivity, see Sec. 2.2.3. Extracting E_0 from the data in Fig. 21 revealed that the characteristic electric field rises linearly with the radiation frequency, see inset in Fig. 21.

In Hall bar structures with semitransparent gate also the effect of the Fermi energy ε_g on the photoconductivity was studied, see Fig. 22 for a radiation frequency of $f = 0.6\,\mathrm{THz}$. The data demonstrates that increasing the Fermi energy leads to a reduction of the nonlinearity, i.e. increase in E_0. Note that for all measured gate voltages the Fermi energy ε_g is above the band gap.

To sum up, illuminating the HgTe QWs with parabolic dispersion with intense terahertz radiation results in strongly nonlinear photoresponses caused by electron-hole pair generation with a photon energy below the band gap. This process results in a nonlinear photoconductivity proportional to $\exp\left(-E_0^2/E^2\right)$

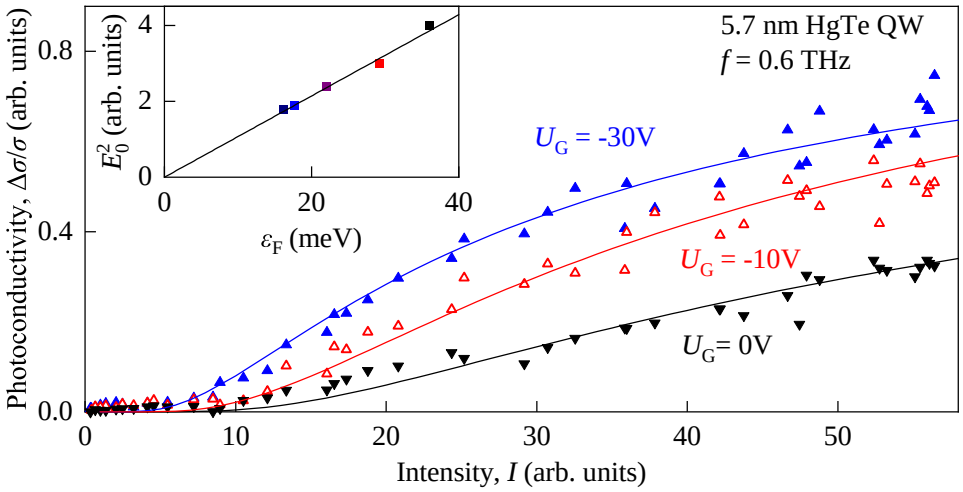

Figure 22: Intensity dependencies of the normalized photoconductivity $\Delta\sigma/\sigma$ induced by linearly polarized radiation with a frequency of $f = 0.6\,\mathrm{THz}$ in a Hall bar sample with a semitransparent gate from wafer #E. The solid lines show fits after Eq. (35) [see also theoretical Eq. (51)] using A and $I_0 \propto E_0^2$ as fitting parameters. The inset shows the dependence of E_0^2 on the Fermi energy. The Fermi energy was obtained from corresponding magnetotransport measurements. Note that the values are given in arbitrary units due to the fact that the intensity acting on 2DEG after transmission through the gate is unknown. Adapted from Ref. [35].

with $E_0 \propto f$ and a photocurrent inverting its sign with the radiation intensity.

4.2 Nonlinearities in HgTe quantum wells close to the critical thickness

For further studies of the process of light impact ionization in HgTe QWs a second wafer (wafer #F) with nearly linear dispersion was investigated, see Sec. 3.1.1. Hereby, only photoconductivity results are presented since the photoconductivity gives a more direct access to the electron-hole pair generation caused by light impact ionization as the photocurrent. Note that the measurements in this section were conducted at a temperature of 4.2 K, if not specified differently. In this structure, the small band gap $\varepsilon_g \approx 4.5\,\mathrm{meV}$ is in the range of photon energies $\hbar\omega$ provided by the pulsed terahertz laser. In the first part of this section we will focus on the data obtained by radiation frequencies with energies smaller than the band gap, i.e., $\hbar\omega < \varepsilon_g$.

In the inset of Fig. 23 the temporal shape of the photoconductivity response is shown for an excitation frequency of 0.6 THz and a radiation intensity of $48\,\mathrm{kW/cm^2}$. This exemplary temporal shape is characteristic for all measured

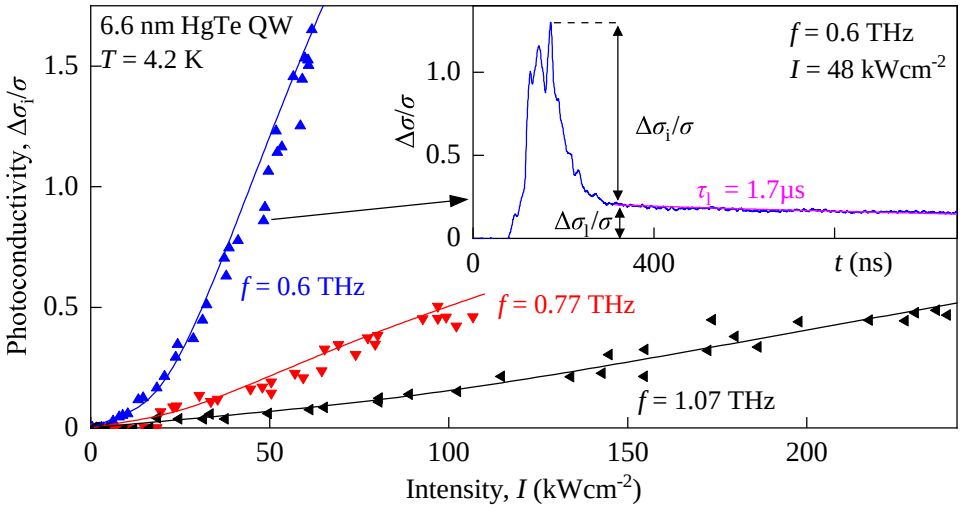

Figure 23: Intensity dependence of the normalized photoconductivity signal $\Delta\sigma_\mathrm{i}/\sigma$ for the frequencies of 0.6 (blue triangles), 0.77 (red triangles), and 1.07 THz (black triangles) in a sample from wafer #F. The solid lines show a fit according to Eq. (36) with the fitting parameters A, B, and I_0. Note that the photon energies for all frequencies is lower than the band gap ($\hbar\omega < \varepsilon_\mathrm{g}$). The inset shows the typical temporal shape of a photoconductivity response for a frequency of 0.6 THz and an intensity of 48 kW/cm^2. The magenta line shows an exponential decay fit according to $\Delta\sigma_\mathrm{l}/\sigma \propto \exp(-t/\tau_\mathrm{l})$. Adapted from Ref. [36].

frequencies. The photoconductivity response consist of two parts differing by response time and amplitude. The first part, in the following referred to as $\Delta\sigma_\mathrm{i}/\sigma$, has a very short response time in the nanosecond range, while the second part $\Delta\sigma_\mathrm{l}/\sigma$ has a substantially longer response time in the microsecond range. At low intensities, $\Delta\sigma_\mathrm{l}/\sigma$ dominates while at high intensities $\Delta\sigma_\mathrm{i}/\sigma$ makes the dominant contribution to the photoconductivity response. As it is shown later on, $\Delta\sigma_\mathrm{i}/\sigma$ corresponds to light impact ionization and, consequently, the focus is put on this contribution in the following part, while $\Delta\sigma_\mathrm{l}/\sigma$ is discussed shortly at the end of this section. Because of the different response times, the amplitudes of $\Delta\sigma_\mathrm{i}/\sigma$ and $\Delta\sigma_\mathrm{l}/\sigma$ could be extracted from the photoconductivity response as sketched in the inset in Fig. 23. In the main plot in Fig. 23 intensity dependencies of $\Delta\sigma_\mathrm{i}/\sigma$ are shown for three different frequencies at a temperature of $T = 4.2$ K. The data reveal a superlinear dependence, while the superlinearity decreases, when the radiation frequency is increased. The data are fitted by

$$\frac{\Delta\sigma}{\sigma} = A \cdot \exp\left(-\frac{I_0}{I}\right) + B \cdot I = A \cdot \exp\left(-\frac{E_0^2}{E^2}\right) + B_E \cdot E^2 \qquad (36)$$

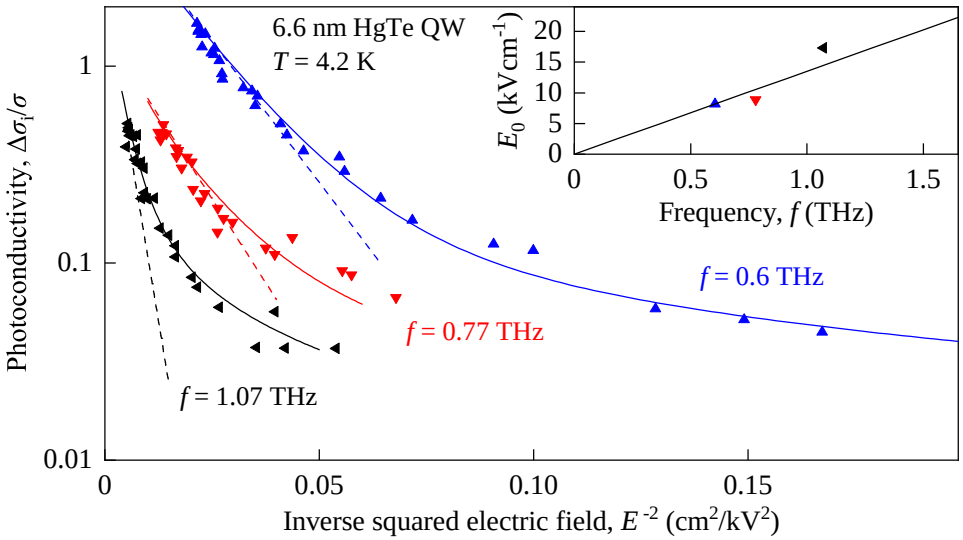

Figure 24: Dependency of the normalized photoconductivity $\Delta\sigma_i/\sigma$ on the inverse squared radiation electric field for the frequencies of 0.6 (blue triangles), 0.77 (red triangles), and 1.07 THz (black triangles) in a sample from wafer #F. The data are presented in a half-logarithmic plot. The solid lines show fits according to Eq. (36). The dashed lines show fits after the exponential term in the right hand side of Eq. (36) resembling the same field dependence as Eq. (63). The inset shows the dependence of the fitting parameter E_0 on the radiation frequency. The solid line is a linear fit after Eq. (63). Adapted from Ref. [36].

with the fitting parameters A, B, and I_0, $B_E = B \cdot n_\omega/(2Z_0)$ and the definitions according to Eq. (35). The fits show that the nonlinearity defined by the parameter $I_0 \propto E_0^2$ decreases increasing the radiation frequency. Replotting the data in a half-logarithmic plot with the inverse squared electric field E^{-2} on the abscissa shows that the exponential term in Eq. (36) describes well the data at high radiation intensities, i.e. low E^{-2}, see Fig. 24. However, at low intensities, i.e. high E^{-2}, a deviation from the exponential behavior is detected and the photoconductivity signal is dominated by the term linear in $E^2 \propto I$, see Eq. (36). The inset in Fig. 24 shows the dependence of the characteristic electric field on the radiation frequency extracted from the fits for the main figure. The rise of E_0 with the intensity also demonstrates the decrease of the superlinearity with an increase of the radiation frequency. Measurements at higher temperatures revealed a decrease of the fitting parameter B and an increase of the characteristic electric field, i.e. a decrease of the nonlinearity. This is exemplarily shown for a radiation frequency of 0.6 THz and three different temperatures in Fig. 25. The data display that at a temperature of 70 K the term linear in $E^2 \propto I$ almost vanishes and the exponential term domi-

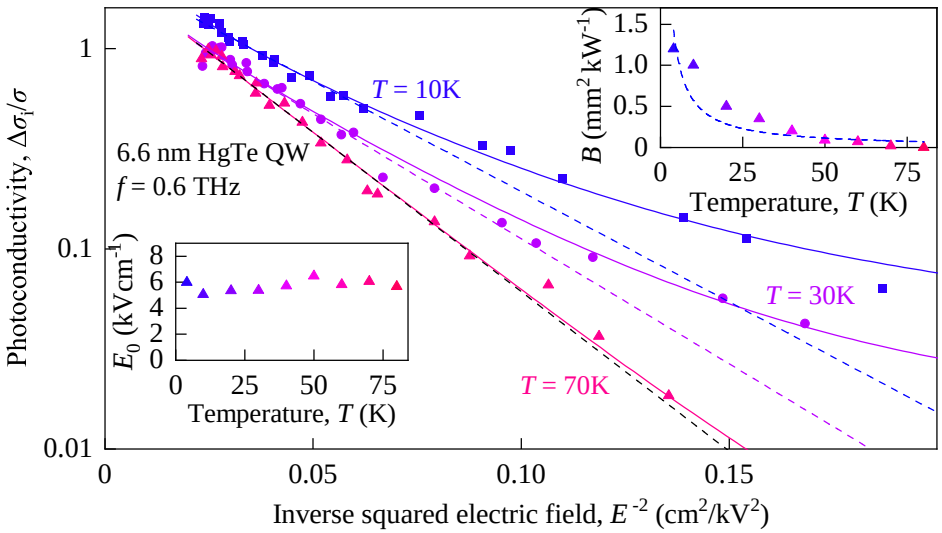

Figure 25: Photoconductivity $\Delta\sigma_\mathrm{i}/\sigma$ as a function of the inverse squared radiation electric field E^{-2} measured for temperatures $T = 10\,\mathrm{K}$ (blue squares), 30 K (purple circles) and 70 K (pink triangles) in a sample from wafer #F. The data were obtained at a radiation frequency of $f = 0.6\,\mathrm{THz}$ and displayed in a half-logarithmic plot. The solid lines depict fits using Eq. (36), while the dashed lines show fits according to solely the exponential term in right hand side of Eq. (36) which gives the same field dependence as the theoretical Eq. (63). Insets show temperature dependencies of the characteristic electric field E_0^2 and the parameter B. Adapted from Ref. [36].

nates. This is also confirmed by the insets in Fig. 25 showing the temperature dependencies of the parameters E_0 and B.

In addition to the results shown above, data for radiation frequencies with photon energies larger than the band gap energy ε_g were obtained and are discussed in the following. Exemplarily, Fig. 26 shows the intensity dependence of the photoconductivity signal for the radiation frequencies 2 and 3.3 THz. Here the qualitative behavior of the intensity dependence is different: For the highest radiation frequency $f = 3.3\,\mathrm{THz}$ a sublinear, saturating behavior was detected with rising intensity instead of a superlinear behavior. This saturation was also observed for $f = 2\,\mathrm{THz}$ but here a superlinear behavior again dominates at high intensities. For the fits in Fig. 26 a term was added to Eq. (36) in order to consider the saturation and, consequently, the fit formula reads

$$\frac{\Delta\sigma_\mathrm{i}}{\sigma} = C\frac{I}{1+I/I_S} + B\cdot I + A\cdot\exp\left(-\frac{I_0}{I}\right), \tag{37}$$

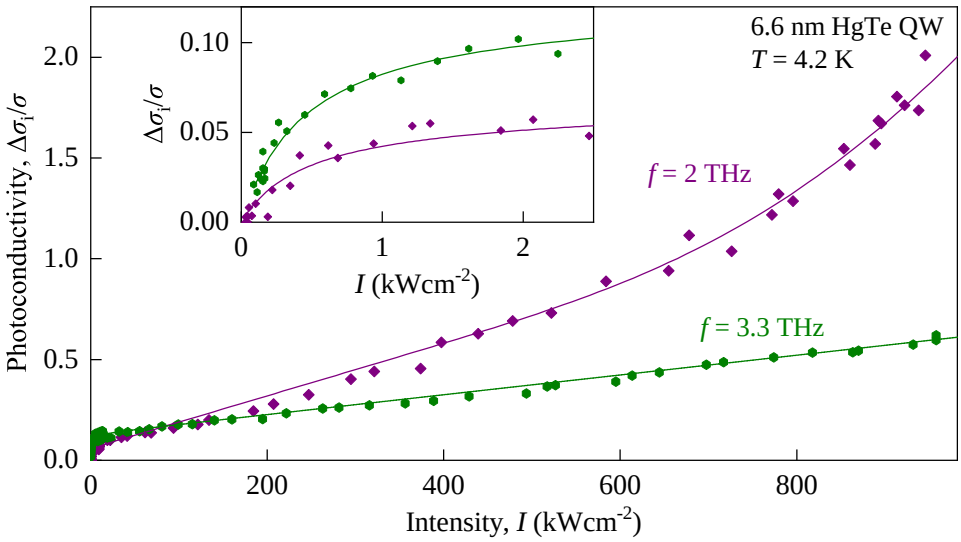

Figure 26: Intensity dependencies of the normalized photoconductivity $\Delta\sigma_\mathrm{i}/\sigma$ at a radiation frequency $f = 2\,\mathrm{THz}$ (violet diamonds) and 3.3 THz (green hexagons) in a sample from wafer #F. The solid lines present fits according to Eq. (37). Note that for both frequencies the photon energy is larger than the band gap ($\hbar\omega > \varepsilon_\mathrm{g}$). The inset shows a zoom-in for low intensities. Adapted from Ref. [36].

with the coefficient C and the saturation intensity I_S as additional fitting parameters. Concluding the experimental part devoted to HgTe QW the slow photoconductivity signal component $\Delta\sigma_\mathrm{l}/\sigma$, see inset in Fig. 23, is shortly described. This signal dominates the photoconductivity signal at low intensities and is characterized by response times $\tau \geq 300\,\mathrm{ns}$, see inset in Fig. 27. For the radiation frequencies of 0.77 and 1.07 THz an intensity dependence of $\Delta\sigma_\mathrm{l}/\sigma$ is shown in Fig. 27. Here, the data is fitted by

$$\frac{\Delta\sigma_\mathrm{l}}{\sigma} = C_l \frac{I}{1 + I/I_{l,S}} + B_l \cdot I \tag{38}$$

with the coefficients B_l and C_l and the saturation intensity $I_{l,S}$ as fitting parameters. The increase of the response time from 300 ns at low intensity, see lower inset in Fig. 27, to several µs at high intensities, see inset in Fig. 24 is caused by the saturation which slows down the time dynamics of the signal. Fig. 28 shows the intensity dependence of the long photoconductivity signal for temperatures of 4 and 20 K and a radiation frequency of 0.6 THz. The data demonstrate a strong reduction of $\Delta\sigma_\mathrm{l}/\sigma$ with temperature, which is confirmed by the inset in Fig. 28 displaying the temperature evolution of the fitting parameter C_l. This inset demonstrates that the slow photoconductivity signal

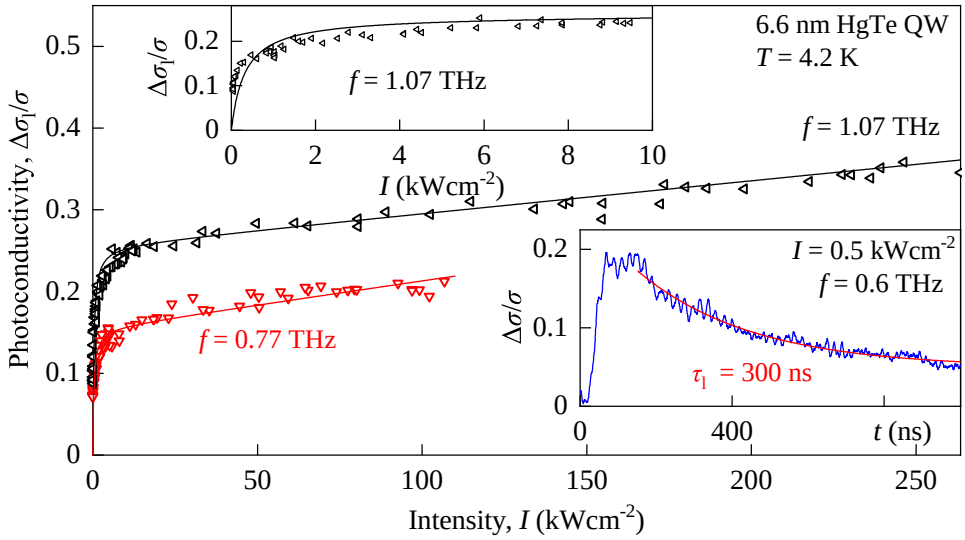

Figure 27: Intensity dependence of the slow component of the normalized photoconductivity $\Delta\sigma_l/\sigma$ excited by the radiation frequencies of 0.77 (red triangles) and 1.07 THz (black triangles) in a sample from wafer #F. The solid lines present fits according to Eq. (38). The left inset shows a zoom-in for low intensities. The right inset shows the typical temporal shape of the photoconductivity pulses obtained for $f = 0.6$ THz and a relatively low intensity of $I = 0.5\,\mathrm{kW/cm^2}$. The red line shows an exponential decay fit according to $\Delta\sigma/\sigma \propto \exp(-t/\tau_l)$. Adapted from Ref. [36].

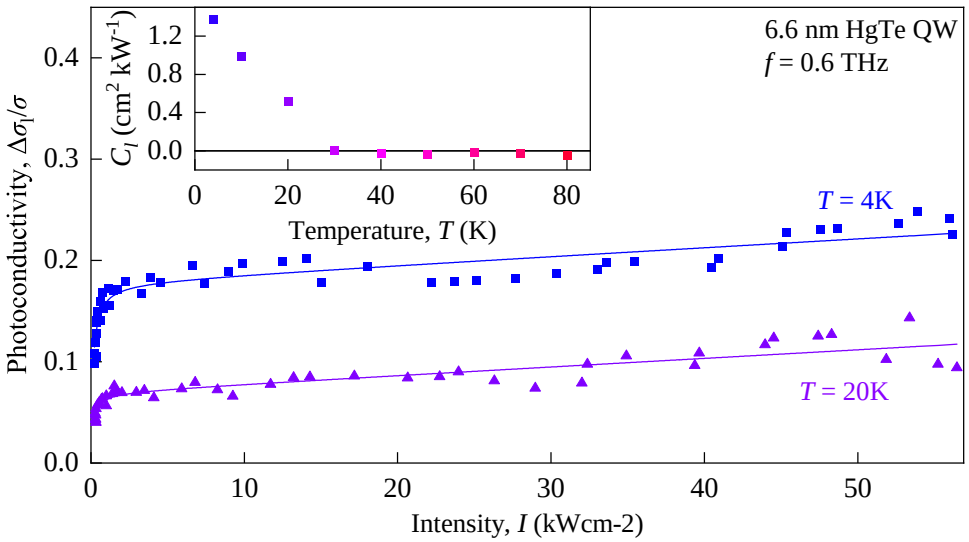

Figure 28: Intensity dependence of the slow component of the normalized photoconductivity $\Delta\sigma_l/\sigma$ excited by the radiation frequency $f = 0.6$ THz at the temperatures of 4 and 20 K. The solid lines present fits according to Eq. (38). The inset shows the temperature evolution of the parameter C_l.

vanishes for temperatures $T \geq 30\,\mathrm{K}$. This fact together with the long response times indicate that the signal is caused by the ionization of impurities. This process is characterized by response times up to the microsecond range and can be activated thermally resulting in no slow photoconductivity response at higher temperatures.

4.3 Discussion

4.3.1 Nonlinear photoconductivity in HgTe quantum wells

The experimental photoconductivity data show the appearance of a terahertz-radiation induced nonlinearity caused by the generation of electron-hole pairs, despite the fact that the photon energy is much smaller than the energy gap. This nonlinearity decreases with rising radiation frequency, see Fig. 21. The observed decrease with the frequency excludes multi-photon processes as driving force for the nonlinearity, since the probability of this process is expected to increase with the radiation frequency [32, 96, 97]. However, this frequency dependence together with the observed exponential increase of the photoconductivity signal $\propto \exp(-E_0^2/E^2)$, see Figs. 19, 21 and Eq. 35 is typical for the process of light impact ionization, see Sec. 2.3 and Refs. [33, 79]. Consequently, light impact ionization is considered as the driving force for the nonlinearity in the following discussion.

In the following the underlying microscopic mechanisms responsible for the formation of the nonlinear photoconductivity in HgTe QWs are outlined. The discussion follows Refs. [35, 36]. As depicted in Sec. 3.1, the Fermi energy in both studied HgTe QWs is much higher than the gap energy ε_g. Moreover, the Fermi energy is also much higher than the impact ionization threshold energy ε_i, see Sec. 2.3. Therefore, the ionization rate is not limited by the absence of conduction band electrons with an energy $\varepsilon \geq \varepsilon_\mathrm{i}$ but by the small number of free states with low energy. Note that in most previous works devoted to impact ionization, e.g. [32], the Fermi energy ε_F was much lower than the impact ionization threshold ε_i and as a consequence, strong heating of the electron gas was necessary to obtain electrons with an energy above the threshold. In our case, heating is not substantial in order to get electrons with energies above the threshold, but the key point is the depletion of the occupied low-energy levels.

In the following, we assume that the main electron momentum relaxation mechanism in HgTe QWs is the scattering by impurities with the corresponding

scattering time $\tau_{\mathrm{i}}(\varepsilon)$, whereas the emission of optical phonons with energies $\varepsilon_{\mathrm{o}} = \hbar\Omega_{\mathrm{o}}$ is the main energy relaxation mechanism. Additionally we consider that the product of radiation angular frequency and momentum relaxation time $\omega\tau$ is larger than unity, which is valid for all experiments conducted in this work.

In the experiments described above, the electric field of the incoming terahertz radiation is polarized along the x-axis. Under these circumstances, the kinetic equation can be written as

$$\frac{\partial f(\boldsymbol{p},t)}{\partial t} + eE\cos(\omega t)\frac{\partial f(\boldsymbol{p},t)}{\partial p_x} = -\frac{f(\boldsymbol{p},t) - f_0(\varepsilon,t)}{\tau_{\mathrm{i}}(\varepsilon)} - St_-^{\mathrm{ph}}\{f\} + St_+^{\mathrm{ph}}\{f\}\,. \quad (39)$$

Here, $f(\boldsymbol{p},t)$ denotes the distribution function, $\boldsymbol{p}$ and e are electron momentum and charge, $v(\varepsilon) = \partial\varepsilon/\partial p$ is the electron velocity at energy ε, $f_0(\varepsilon,t)$ is the contribution of $f(\boldsymbol{p},t)$ independent on the direction of $\boldsymbol{p}$, and $St_-^{\mathrm{ph}}\{f\} + St_+^{\mathrm{ph}}\{f\}$ denotes the collision integral related to optical phonons. Note that the detached terms $St_-^{\mathrm{ph}}\{f\}$ and $St_+^{\mathrm{ph}}\{f\}$ also describe the number of electrons coming into/leaving a state with momentum $\boldsymbol{p}$ in a unit of time considering the interaction with optical phonons. The characteristic impurity scattering time $\tau_{\mathrm{i}}(\varepsilon)$ can also be written as $\tau_{\mathrm{i}}(\varepsilon) = \tau_{\mathrm{i}0}g(0)/g(\varepsilon)$ [98] with the scattering time on the conduction band bottom $\tau_{\mathrm{i}0}$ and the conduction band density of states $g(\varepsilon) = p(\varepsilon)/v(\varepsilon)\pi\hbar^2$.

Assuming the main scattering mechanisms stated above, $f(\boldsymbol{p},t)$ is approximately isotropic and can be written as $f(\boldsymbol{p},t) = f_0(\varepsilon) + f_1(\boldsymbol{p},t)$ with a minor anisotropic correction $f_1(\boldsymbol{p},t)$. The terahertz radiation induced electron gas heating is assumed to be strong enough that the effective electron temperature T_e is higher than the phonon energy $\hbar\Omega_{\mathrm{O}}$. Consequently, $f_0(\varepsilon,t)$ only varies very slowly at energy scales around the phonon energy ε_{O}. On the other hand, the electron gas heating is considered to be weak enough that the average electron energy does not achieve values much higher than the initial Fermi energy ε_{F}. In the case of $\varepsilon > \varepsilon_{\mathrm{O}}$, $f_0(\varepsilon)$ then fulfills the balance equation

$$D(\varepsilon)\frac{\partial f_0}{\partial\varepsilon} + \frac{\varepsilon_{\mathrm{O}}}{\tau_{\mathrm{ph}}(\varepsilon)}f_0(\varepsilon)\left[1 - f_0(\varepsilon)\right] = 0 \quad (40)$$

$$D(\varepsilon) = \frac{e^2E^2v^2(\varepsilon)}{4\omega^2\tau_{\mathrm{i}}(\varepsilon)},\ \frac{1}{\tau_{\mathrm{ph}}(\varepsilon)} = \frac{4\pi\varepsilon_{\mathrm{O}}e^2g(\varepsilon)}{\bar{\epsilon}p(\varepsilon)}. \quad (41)$$

Here, $D(\varepsilon)$ denotes the diffusion coefficient of electrons in the energy space, τ_{ph} (see [99]) is the characteristic phonon emission time, and $1/\bar{\epsilon} = 1/\epsilon_\infty - 1/\epsilon_0$, while ϵ_∞ and ϵ_0 are the high- and low-frequency dielectric permittivities. In Eq. (40), the first part characterizes the terahertz radiation-induced electron gas heating, while the phonon-induced energy losses are described by the second term. Solving Eq. (40) gives

$$f_0(\varepsilon) = \frac{1}{1 + \exp\left[-L(\varepsilon)\right]}, \tag{42}$$

$$L(\varepsilon) = \int_{\varepsilon}^{\varepsilon_{\mathrm{E}}} \frac{\varepsilon_{\mathrm{O}}}{D(\varepsilon')\,\tau_{\mathrm{ph}}(\varepsilon')} d\varepsilon', \tag{43}$$

where the upper integration limit ε_{E} can be determined by the normalization on the density

$$n = \int_0^\infty f_0(\varepsilon) g(\varepsilon) d\varepsilon. \tag{44}$$

Due to the assumption of $f_0(\varepsilon)$ varying slowly on the scale of ε_{O} the same is valid for $1 - f_0(\varepsilon)$. Consequently, from $f_0(\varepsilon) \approx 1$ follows $1 - f_0(\varepsilon) \propto \exp\left[-L(\varepsilon)\right]$. This is fulfilled if $|L(\varepsilon + \varepsilon_{\mathrm{O}}) - L(\varepsilon)| \ll 1$, which is, according to Eqs. (42) and (43), equivalent to $\varepsilon_{\mathrm{O}}^2 \ll D\tau_{\mathrm{ph}}$.

In the case of $\varepsilon < \varepsilon_{\mathrm{O}}$, however, the distribution function $f_0(\varepsilon)$ is characterized by

$$\frac{1}{g(\varepsilon)} \frac{\partial}{\partial \varepsilon} \left[g(\varepsilon)\, D(\varepsilon) \frac{\partial f_0}{\partial \varepsilon} \right] + \frac{1}{\tau_{\mathrm{ph}}^+(\varepsilon)} f_0(\varepsilon + \varepsilon_0) \left[1 - f_0(\varepsilon)\right] = 0, \tag{45}$$

where $f_0(\varepsilon + \varepsilon_{\mathrm{O}})$ is determined from Eq. (40) and

$$\frac{1}{\tau_{\mathrm{ph}}^+} = \frac{2\pi^2 e^2 \varepsilon_{\mathrm{O}} g(\varepsilon - \varepsilon_0) g(\varepsilon)}{\bar{\epsilon} p(\varepsilon)},$$

for a derivation of $1/\tau_{\mathrm{ph}}^+$ see appendix of Ref. [35]. Equation (45) cannot be solved analytically, but under the conditions $\varepsilon_{\mathrm{O}}^2 \ll D\tau_{\mathrm{ph}}$ and $f_0(\varepsilon)$ mentioned above, the second term gets negligibly small and the distribution function can be approximated as constant in the energy range below ε_{O}. Assuming $\varepsilon = \varepsilon_{\mathrm{O}}$

the distribution function can be determined using Eq. (42). If the electron gas heating is not strong enough to lift the effective electron temperature above the Fermi energy, the distribution can be approximated as $f_0 \approx 1$ in the whole range of energies up to ε_E. At higher energies $\varepsilon > \varepsilon_\mathrm{E}$, however, $f_0 \approx 0$ is valid. From this considerations and Eq. (44) it follows

$$n \approx \int_0^{\varepsilon_\mathrm{E}} g(\varepsilon) d\varepsilon, \tag{46}$$

and, consequently, $\varepsilon_\mathrm{E} \cong \varepsilon_\mathrm{F}$ in this case.

Since the Fermi energy in our samples is much larger than the ionization threshold energy ε_i the ionization rate W is limited by the number of unoccupied low-energy states $\rho(\varepsilon)$ described by

$$\rho(\varepsilon) = 1 - f_0(\varepsilon) \approx \exp\left[-L(\varepsilon)\right] . \tag{47}$$

The lower integration limit in Eq. (43) cannot be determined since it is dependent on the exact characteristics of impact ionization. Thus, this limit as is considered as a parameter ε^*. Therefore the dependences of the ionization rate W on frequency and radiation electric field are broken down to $\exp(-L^*)$, i.e.

$$W = W_i \cdot \exp\left(-L^*\right), \tag{48}$$

where W_i is the probability of a single ionization event and

$$L^* = \int_{\varepsilon^*}^{\varepsilon_\mathrm{F}} \frac{\varepsilon_\mathrm{O}}{D(\varepsilon)\tau_\mathrm{ph}(\varepsilon)} d\varepsilon. \tag{49}$$

Parabolic Dispersion For the 5.7 nm wide HgTe QW used in this work (wafer #E) the energy dispersion is parabolic and analytically described by the Bernevig-Hughes-Zhang model [11]:

$$\varepsilon(p) = \sqrt{\varepsilon_\mathrm{g}^2/4 + p^2\varepsilon_\mathrm{g}/2m} - \varepsilon_\mathrm{g}/2 . \tag{50}$$

Subsequently, the density of states $g(\varepsilon)$, electron momentum $p(\varepsilon)$ and electron velocity $v(\varepsilon)$ can be written as $g(\varepsilon) = m(2\varepsilon+\varepsilon_\mathrm{g})/\pi\hbar^2\varepsilon_\mathrm{g}$, $p(\varepsilon) = \sqrt{2m\varepsilon(\varepsilon+\varepsilon_\mathrm{g})\varepsilon_\mathrm{g}^{-1}}$ and $v^2(\varepsilon) = 2\varepsilon(\varepsilon+\varepsilon_\mathrm{g})\varepsilon_\mathrm{g}/m(2\varepsilon-\varepsilon_\mathrm{g})^2$, where m denotes the effective mass of

electrons in the low-energy region of the conduction band. Substitution of these expressions in Eq. (41), Eq. (49), and Eq. (48) leads to the following equation for the ionization rate:

$$W = W_{\mathrm{i}} \cdot \exp\left(-\frac{E_0^2}{E^2}\right), \tag{51}$$

where

$$E_0^2 = \frac{8\pi\Omega_{\mathrm{O}}^2\omega^2 m^{3/2}\tau_{\mathrm{i}0}}{\bar{\epsilon}\sqrt{2\varepsilon_{\mathrm{g}}}} \int_{\varepsilon^*/\varepsilon_{\mathrm{g}}}^{\varepsilon_{\mathrm{F}}/\varepsilon_{\mathrm{g}}} \frac{(2z+1)^2}{(z^2+z)^{3/2}} dz\,. \tag{52}$$

Equations (51) and (52) confirm the experimental key results regarding the photoconductivity measurements in wafer #E: The exponential increase of the normalized conductivity $\Delta\sigma/\sigma$ with E^{-2}, see Fig. 21, is reflected in Eq. (51), considering $\Delta\sigma/\sigma \propto W$. The linear dependence of the characteristic field E_0 on the radiation frequency, see inset in Fig. 21, is also theoretically confirmed in Eq. (52). Moreover, the rise of the characteristic electric field E_0 with the Fermi energy ε_{F} depicted in the inset in Fig. 22 is also qualitatively described in Eq. (52), but, on the other hand, cannot be analyzed quantitatively. This originates from the fact that an increase of the upper limit of the integration in Eq. (52) being proportional to ε_{F} also affects the lower limit proportional to the parameter ε^*. Eventually, the increase of E_0 with rising temperature T, see inset in Fig. 20, is not directly reflected in the equations, but reasonable since the rise of the electron temperature is obtained at higher fields due to increasing energy losses at higher temperatures.

Linear Dispersion For wafer #F, however, the band structure is almost linear, i.e. $\varepsilon = v_{\mathrm{F}}p$, where v_{F} is the Fermi velocity. From this follows $p(\varepsilon) = \varepsilon/v_{\mathrm{F}}$ and, additionally, the density of states can be written as $g(\varepsilon) = \varepsilon/\pi\hbar^2 v_{\mathrm{F}}^2$. Note that, strictly speaking, impact ionization is strongly suppressed in systems with perfect linear dispersion due to the energy-momentum conservation law. In the case relevant to this work, the Fermi energy is high, so holes belonging to the region far away from $k = 0$ can contribute to the impact ionization process. In this region, the dispersion deviates from the linear band structure, which renders the impact ionization process possible. Applying the equations for $p(\varepsilon)$ and $g(\varepsilon)$ to Eq. (41), the electron scattering rate on phonons can be

rewritten as

$$\frac{1}{\tau_{\mathrm{ph}}(\varepsilon)} = \frac{4\pi\varepsilon_{\mathrm{O}}e^2}{v_F\bar{\epsilon}\hbar^2}\,. \tag{53}$$

Above it has been considered, that the main momentum relaxation mechanism is the scattering on charged impurities described by τ_{i}. Assuming a linear spectrum, the scattering rate on impurities can be described as $\tau_{\mathrm{i}}^{-1}(\varepsilon) = \tau_{\mathrm{iF}}^{-1}(\varepsilon_{\mathrm{F}}/\varepsilon)$. Then, assuming the high-frequency limit $\omega\tau_{\mathrm{i}} \gg 1$ relevant to the experiment, the diffusion coefficient (see Eq. (41)) is given by

$$D(\varepsilon) = \frac{e^2E^2v_{\mathrm{F}}^2\varepsilon_{\mathrm{F}}}{4\omega^2\tau_{\mathrm{iF}}\varepsilon} \tag{54}$$

Applying Eqs. (53) and (54) to Eq. (43), L is given by

$$L = \frac{\varepsilon_{\mathrm{E}}^2 - \varepsilon^2}{\tilde{\varepsilon}^2}\,, \tag{55}$$

with the definition of

$$\tilde{\varepsilon}^2 = \frac{\bar{\epsilon}v_{\mathrm{F}}^3\hbar^2\varepsilon_{\mathrm{F}}E^2}{8\pi\varepsilon_0\tau_{\mathrm{iF}}\omega^2}\,. \tag{56}$$

Defining $\Lambda = \exp(-\varepsilon_{\mathrm{E}}^2/\tilde{\varepsilon}^2)$, the distribution function from Eq. (42) can then be written as

$$f_0(\varepsilon) = \frac{1}{1 + \Lambda\exp(\varepsilon^2/\tilde{\varepsilon}^2)}\,, \tag{57}$$

The parameter ε_{E} can now be eliminated by normalization on the density (see Eq. (44)) using Eq. (57) and the density of states $g(\varepsilon) = \varepsilon/\pi\hbar^2v_{\mathrm{F}}^2$ leading to

$$\Lambda = \frac{1}{\exp(2\pi n\hbar^2v_{\mathrm{F}}^2/\tilde{\varepsilon}^2) - 1}\,. \tag{58}$$

As discussed above the generation of electron-hole pairs due to light impact ionization is mainly limited by the number of unoccupied states in the low energy region $\varepsilon \ll \varepsilon_{\mathrm{E}}$ of the conduction band, described by $\rho(\varepsilon) = 1 - f_0(\varepsilon)$. Using the approximations discussed above Eq. (47) it follows analogously

$$\rho(\varepsilon) \approx \Lambda\exp(\varepsilon^2/\tilde{\varepsilon}^2)\,. \tag{59}$$

From the condition of free unoccupied states in the low energy region, i.e. $\rho(\varepsilon) \ll 1$ follows $\Lambda \ll 1$ and consequently it can be approximated

$$\Lambda \approx \exp(-2\pi n\hbar^2 v_{\mathrm{F}}^2/\tilde{\varepsilon}^2)\,. \tag{60}$$

Taking into account Eqs. (59) and (60) the free low energy states distribution can be written as

$$\rho(\varepsilon) \approx \exp[-(2\pi n\hbar^2 v_{\mathrm{F}}^2 - \varepsilon^2)/\tilde{\varepsilon}^2]\,. \tag{61}$$

Similar as stated above in the case of wafer #E with parabolic dispersion, it is not possible to determine the exact "low energy" region important for the generation rate W. That is because the probability of an impact ionization event W_i and the recombination rate of electron-hole pairs is unknown. By analogy with above, the low energy range is denoted by ε^*. Consequently the generation rate W is described by

$$W \propto \rho^2(\varepsilon_c) = \exp[-2(2\pi\hbar^2 v_F^2 - \varepsilon^{*2})/\tilde{\varepsilon}^2]\,, \tag{62}$$

and, using Eq. (56),

$$W \propto \exp(-E_0^2/E^2)\,, \quad \text{with} \quad E_0^2 \propto \omega^2\,. \tag{63}$$

The theoretical Eq. (63) describes well the experimentally observed nonlinear dependence of the photoconductivity $\Delta\sigma_i/\sigma$ in wafer #F at high intensities, see e.g. Fig. 24, considering $\Delta\sigma/\sigma \propto W$. The rise of the characteristic electric field E_0 with the temperature T, see Fig. 25, is also described by the theory discussed above considering higher energy losses due to phonons at higher temperatures, which causes a weaker terahertz-radiation induced electron gas heating and, consequently, a higher E_0. Furthermore, the observed increase of the characteristic electric field E_0 with the frequency ω, see inset in Fig. 24, is theoretically confirmed in Eq. (63). This strong frequency dependence of the light impact ionization process also explains why no superlinearity could be detected for the highest measured frequency, see Fig. 26.

Overall, the results in terms of photoconductivity obtained for wafer #E and wafer #F are very similar: Both samples show a nonlinear behavior proportional to $\exp(-E_0^2/E^2)$ at high intensities caused by the light impact ionization discussed above. All features of this signal contribution are in line with the

theory of light impact ionization discussed above. At low intensities both samples show a deviation from this exponential behavior which is supposed to be caused by μ-photoconductivity, see Sec. 2.2.3. This is considered as a linear contribution in the fit formulas, see Eqs. (36) and (37).

In wafer #F, however, other additional contributions were detected. For radiation frequencies with photon energies larger than the gap energy ($\varepsilon_g \approx 4.5\,\mathrm{meV}$ in wafer #F) also direct optical band-to-band transitions are possible as an absorption mechanism. This was considered in the first term on the right side of the experimental fit formula Eq. (37) as a linear, saturating contribution. At low intensities, the possible final states of direct optical transitions are occupied due to the high Fermi level in wafer #F and, consequently, these transitions are suppressed. As these final states become unoccupied due to electron gas heating as discussed above, direct optical transitions become relevant. At higher intensities these transitions saturate, which is a well-known phenomenon [32].

Furthermore, a third contribution $\Delta\sigma_\mathrm{I}/\sigma$ with much longer response time was additionally observed in wafer #F, see Figs. 27 and 28. The long response time together with the vanishing of the contribution at temperatures above 20 K indicates the ionization of impurities as source of this signal. At higher temperatures, these impurities are already completely ionized thermally, which leads to a vanishing of $\Delta\sigma_\mathrm{I}/\sigma$. Similarly, at low temperatures and high radiation intensities, the impurities get completely ionized due to intense terahertz radiation resulting in a saturation of the signal with rising intensity.

4.3.2 Nonlinear photocurrent in HgTe quantum wells

In our experimental setup, a homogenous sample without an inversion center is uniformly illuminated by normal incident radiation. Under these conditions the appearance of second order electric field effects is possible, see Sec. 2.2. The experimental results in the previous section, see Fig. 17, demonstrate a characteristic polarization dependence due to the LPGE for the measured photocurrent, see Sec. 2.2 and Eq. 34, revealing that the CPGE provides no significant contribution. In the following the microscopic origin of the LPGE observed in the experiments is discussed referring to model and theory developed parallel to the experiments by E.L. Ivchenko and G.V. Budkin from the Ioffe Institute, St. Petersburg [35].

This model considers the LPGE to be caused by the spatial displacement of

carriers due to optical transitions, i.e. a shift photocurrent [37, 48, 56, 100–104].

For the calculation of the shift photocurrent, Drude-like optical transitions within the lowest conduction band c and the highest valence band v are considered. Since electron-hole pairs are generated due to light impact ionization, see previous section and Sec. 2.3, the total photocurrent consists of the sum of the electron photocurrent contribution in the conduction band $\boldsymbol{j}^{(c)}$ and the hole photocurrent in the valence band $\boldsymbol{j}^{(v)}$ given by

$$\boldsymbol{j} = \boldsymbol{j}^{(c)} + \boldsymbol{j}^{(v)} \,. \tag{64}$$

According to Refs. [35, 37] the shift photocurrent $\boldsymbol{j}^{(l)}$ with $l = c, v$ is described by

$$\boldsymbol{j}^{(l)} = 2q_l \sum_{\boldsymbol{k}'\boldsymbol{k}} W_l(\boldsymbol{k}', \boldsymbol{k}) \boldsymbol{R}_l(\boldsymbol{k}', \boldsymbol{k}) \,. \tag{65}$$

Here, $W_l(\boldsymbol{k}', \boldsymbol{k})$ describes the transition rate from the state $|l\boldsymbol{k}\rangle$ to the state $|l\boldsymbol{k}'\rangle$, q_l is the charge of the corresponding carriers ($q_c = e$, $q_v = |e|$) and $\boldsymbol{R}_l(\boldsymbol{k}', \boldsymbol{k})$ is the elementary shift due to the transition from $|l\boldsymbol{k}\rangle$ to $|l\boldsymbol{k}'\rangle$. Drude-like intraband transition rely on the involvement of phonon or defect scattering. In the following, defect scattering is considered as dominant mechanism for the shift photocurrent generation by intraband optical transitions. Considering the condition $\omega\tau \gg 1$ relevant to the experiment, the transition rate can be calculated using Fermi's golden rule for indirect transitions:

$$W_l(\boldsymbol{k}', \boldsymbol{k}) = \frac{2\pi}{\hbar} N_d |M_{l\boldsymbol{k}', l\boldsymbol{k}}|^2 (f_{lk} - f_{lk'}) \delta(E_{lk'} - E_{lk} - \hbar\omega) \,, \tag{66}$$

Here, the matrix element can be written as

$$M_{l\boldsymbol{k}', l\boldsymbol{k}} = \frac{V_l(\boldsymbol{k}) - V_l(\boldsymbol{k}')}{\hbar\omega} \, U_l(\boldsymbol{k}', \boldsymbol{k}) \,, \tag{67}$$

with the defect scattering matrix element $U_l(\boldsymbol{k}', \boldsymbol{k})$, the effective mass m_l corresponding to either conduction (m_c) or valence band (m_v), the scattering defect density N_d, the energy $E_{lk} = \hbar^2 k^2/(2m_l)$, the electron distribution function f_{lk} and the matrix element of electron-light interaction $V_l(\boldsymbol{k})$. The difference between the carrier-light interaction matrix elements for the states $|l\boldsymbol{k}\rangle$ and

$|l\boldsymbol{k}'\rangle$ can be expressed as

$$V_l(\boldsymbol{k}) - V_l(\boldsymbol{k}') = \frac{q_l \hbar A_0}{m_l c} \boldsymbol{e} \cdot (\boldsymbol{k}' - \boldsymbol{k}) \ , \tag{68}$$

where A_0 is the amplitude of the radiation vector potential and $\boldsymbol{e}$ is the unit vector of polarization. Using the theory from Ref. [102], the elementary shift $\boldsymbol{R}_l(\boldsymbol{k}', \boldsymbol{k})$ can be written as

$$\boldsymbol{R}_l(\boldsymbol{k}', \boldsymbol{k}) = -\frac{\mathrm{Im}\left[U_l^*(\boldsymbol{k}', \boldsymbol{k}) \left(\boldsymbol{\nabla}_{\boldsymbol{k}'} + \boldsymbol{\nabla}_{\boldsymbol{k}}\right) U_l(\boldsymbol{k}', \boldsymbol{k})\right]}{\left|U_l(\boldsymbol{k}', \boldsymbol{k})\right|^2} + \mathcal{A}_{l\boldsymbol{k}'} - \mathcal{A}_{l\boldsymbol{k}} \ , \tag{69}$$

where $\mathcal{A}_{l\boldsymbol{k}}$ represents the Berry connection. The contributions from the Berry connections cancel out each other in the steady-state regime of photoexcitation and, thus, are neglected in the following. The carrier-defect interaction operator U_l is Hermitian, i.e.

$$U_l^*(\boldsymbol{k}', \boldsymbol{k}) = U_l(\boldsymbol{k}, \boldsymbol{k}') \ , \tag{70}$$

and it can be written

$$\boldsymbol{R}_l(\boldsymbol{k}', \boldsymbol{k}) = -\frac{\mathrm{Im}\left[U_l(\boldsymbol{k}, \boldsymbol{k}') \left(\boldsymbol{\nabla}_{\boldsymbol{k}'} + \boldsymbol{\nabla}_{\boldsymbol{k}}\right) U_l(\boldsymbol{k}', \boldsymbol{k})\right]}{\left|U_l(\boldsymbol{k}', \boldsymbol{k})\right|^2} \ , . \tag{71}$$

Consequently, if the matrix element $U_l(\boldsymbol{k}', \boldsymbol{k})$ is only dependent on the difference $\boldsymbol{k}' - \boldsymbol{k}$, the elementary shift $\boldsymbol{R}_l(\boldsymbol{k}', \boldsymbol{k})$ vanishes, since $\left(\boldsymbol{\nabla}_{\boldsymbol{k}'} + \boldsymbol{\nabla}_{\boldsymbol{k}}\right) U_l(\boldsymbol{k}' - \boldsymbol{k}) = 0$. Thus, a special case is considered in the following, where $U_l(\boldsymbol{k}', \boldsymbol{k})$ also depends on the sum $\boldsymbol{k}' + \boldsymbol{k}$ and the matrix element $U_l(\boldsymbol{k}', \boldsymbol{k})$ can be expanded as follows:

$$U_l(\boldsymbol{k}', \boldsymbol{k}) = U_0^{(l)} + \mathrm{i} U_{1,\alpha}^{(l)} (k'_\alpha - k_\alpha) + \ U_{2,\beta\gamma}^{(l)} (k'_\beta k'_\gamma + k_\beta k_\gamma) \ , \tag{72}$$

where the Greek indices α, β, γ denote the directions x, y and $U_{2,\beta\gamma}^{(l)} = U_{2,\gamma\beta}^{(l)}$. According to Eqs. (65), (66) and (67), the relevant shift contribution is proportional to $\left|U_l(\boldsymbol{k}', \boldsymbol{k})\right|^2 R_{l\beta}(\boldsymbol{k}', \boldsymbol{k})$. With Eqs. (71) and (72), this can be written as

$$\left|U_l(\boldsymbol{k}', \boldsymbol{k})\right|^2 R_{l\beta}(\boldsymbol{k}', \boldsymbol{k}) = 2 U_{1,\alpha}^{(l)} U_{2,\beta\gamma}^{(l)} (k'_\alpha - k_\alpha)(k'_\gamma + k_\gamma) \ . \tag{73}$$

However, in order not to overload the discussion of the experimental results with cumbersome formulas, in the following only resulting equations for the

shift photocurrent are given. For linearly polarized radiation with the electric field $\boldsymbol{E}$ parallel to the x-direction passing a quarter-wave plate at angle φ, see Sec. 3.2.2, the result is

$$j_{l,x} = \left(\chi_{l,x}^{(0)} + \chi_{l,x}^{(1)} P_{L1}(\varphi) + \chi_{l,x}^{(2)} P_{L2}(\varphi)\right) n_l I, \tag{74}$$

$$j_{l,y} = \left(\chi_{l,y}^{(0)} - \chi_{l,y}^{(1)} P_{L1}(\varphi) + \chi_{l,y}^{(2)} P_{L2}(\varphi)\right) n_l I, \tag{75}$$

where n_l describes the electron or hole densities, respectively, and the Stokes parameters $P_{\mathrm{L1,L2}}(\varphi)$ are described by Eq. (31). Note that Eqs. (74) and (75) agree well with the experimental fit equation (34) for the polarization dependence shown in Fig. 17(c), considering $J \propto j$. The coefficients $\chi_{i,\alpha}^{(l)}$ can be written as

$$\begin{aligned}
\chi_{l,\alpha}^{(0)} &= 2\frac{\eta_l(I)}{n_l}\frac{q_l m_l}{\hbar^2}\frac{U_{2,\alpha\gamma}^{(l)} U_{1,\gamma}^{(l)}}{U_0^{(l)2}}\,, \\
\chi_{l,\alpha}^{(1)} &= \frac{\eta_l(I)}{n_l}\frac{q_l m_l}{\hbar^2}\frac{U_{2,\alpha\gamma}^{(l)} U_{1,\gamma}^{(l)}(2\delta_{\alpha\gamma}-1)}{U_0^{(l)2}}\,, \\
\chi_{l,\alpha}^{(2)} &= \frac{\eta_l(I)}{n_l}\frac{q_l m_l}{\hbar^2}\frac{U_{2,\alpha\beta}^{(l)} U_{1,\gamma}^{(l)}(1-\delta_{\beta\gamma})}{U_0^{(l)2}}\,,
\end{aligned} \tag{76}$$

with the radiation intensity $I \propto E^2$, and the absorbance

$$\eta_l(I) = W_l(I)\frac{\hbar\omega}{I}\,. \tag{77}$$

Here the term $W_l(I)$ defines the absorption rate per unit area coming from the respective carriers l. In our case the electron and hole densities are non-equilibrium densities, thus the absorbance $\eta_l(I)$ depends on the radiation intensity. In the calculations leading to Eq. (76) the second and third expansion terms in Eq. (72) were considered to be smaller than the $\boldsymbol{k}$-independent term U_0. Further analysis demonstrated that the term $\eta_l(I)/n_l$ does not depend on the carrier density n_l under the relevant experimental conditions, which supports the appearance of n_l as a factor in Eqs. (74) and (75).

Since wafer #E is grown on (013)-oriented GaAs, there is no symmetry operation besides the identity. Thus, there is no distinct axis in the quantum well plane and, consequently, there are no symmetry constraints for the coefficients

$U_{1,\alpha}^{(l)}$ and $U_{2,\alpha}^{(l)}$. From this follows that the coefficients $\chi_{c,\alpha}^{(i)}$ for the electrons in the conduction band and the coefficients $\chi_{v,\alpha}^{(i)}$ for the holes in the valence band are linearly independent, i.e., the photocurrent contributions coming from electrons and holes do not have to be parallel to each other. During the process of light impact ionization electron-hole pairs are generated as discussed in the previous section. This leads to an increase of both the electron and hole carrier densities in the conduction and valence bands, respectively. The photocurrent in the x-direction can then be described by

$$J_x = \underbrace{\chi_{c,x}(n_0 + \Delta n)I}_{J_{c,x}} + \underbrace{\chi_{v,x}\Delta pI}_{J_{v,x}} , \tag{78}$$

where n_0 is the electron carrier density in the equilibrium, Δn and Δp are the densities of generated electrons and holes with $\Delta n = \Delta p \propto \exp(-I_0/I)$, see the discussion of light impact ionization in the previous section. Since most of the experimental data was obtained measuring the photocurrent in the x-direction the further discussion is done focusing on j_x. Assuming linearly polarized radiation with $\varphi = 0$ the coefficients χ_c and χ_v can be calculated from Eq. (74)

$$\chi_{c,x} = \kappa(\chi_{c,x}^{(0)} + \chi_{c,x}^{(1)}) \, , \chi_{v,x} = \kappa(\chi_{v,x}^{(0)} + \chi_{v,x}^{(1)}) \, , \tag{79}$$

where κ is the proportionality parameter between photocurrent J_x and current density j_x, which is determined by the exact geometry of laser spot and sample. If $|\chi_{v,x}| > |\chi_{c,x}|$ the hole photocurrent contribution rises faster with increasing intensity than the electron contribution and, at a given intensity, the hole photocurrent exceeds the electronic one. Considering opposite signs for $\chi_{c,x}$ and $\chi_{v,x}$ the nonlinear, sign-inverting photocurrent can be fitted by Eq. (78), see red curve in Fig. 29. The equilibrium carrier density n_0 was extracted from magnetotransport measurements, while the generated carrier densities $\Delta n = \Delta p$ are taken from the fit of the corresponding photoconductivity data according to Eq. (35), see black dashed curve in Fig. 29, considering $\Delta n = \Delta p \propto \Delta\sigma/\sigma$. The fit reveals that $|\chi_{v,x}|$ exceeds $|\chi_{c,x}|$ by an order of magnitude. The assumption $|\chi_{v,x}|>|\chi_{c,x}|$ done above is also confirmed by numerical calculations done including phonon-involved optical transitions [35]. These shift photocurrent calculations based on the Bernevig-Hughes-Zhang model [11] considering scattering by acoustic phonons in (013)-oriented HgTe QWs [105] have demonstrated that the photocurrent established by holes in

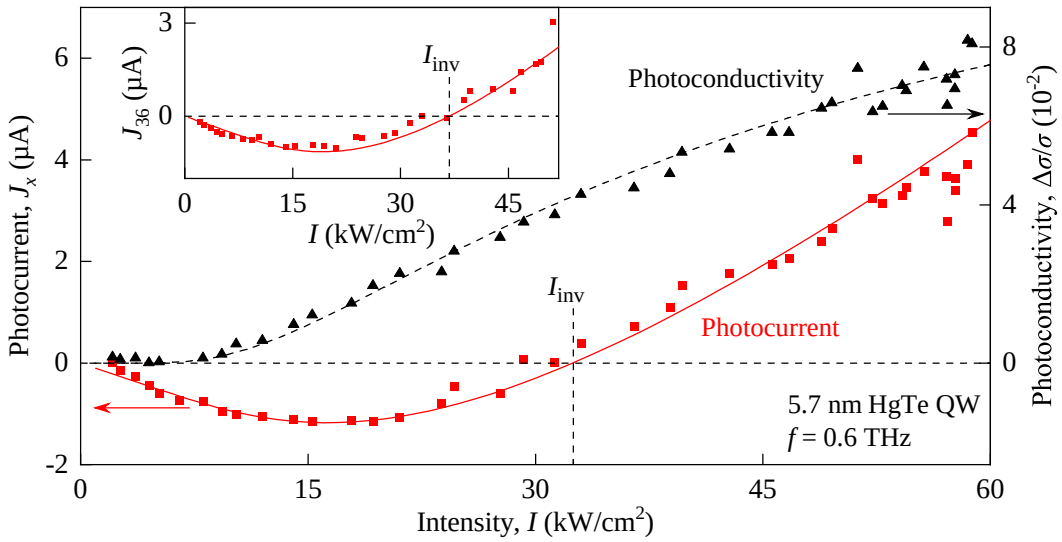

Figure 29: Photocurrent (red squares) and photoconductivity (black triangles) excited by linearly polarized radiation with a frequency of $f = 0.6\,\mathrm{THz}$ as a function of the radiation intensity. The signals were picked up at the central contacts 2 and 5 in a sample from wafer #E, see Fig. 10. The dashed black line shows fit according to Eq. (35) with the fitting parameters $A = 0.15$ and $I_0 = 41\,\mathrm{kW/cm^2}$. The solid red line shows a fit of the photocurrent according to Eq. (78). Here, the parameters A and I_0 are taken from the photoconductivity fit, the carrier density $n = 3 \times 10^{11}\,\mathrm{cm^{-2}}$ was determined by transport measurements, and the coefficients $\chi_c = 3.4 \times 10^{-13}\,\mu\mathrm{Acm^4/kW}$ and $\chi_v = 8.2 \times 10^{-12}\,\mu\mathrm{Acm^4/kW}$ are fitting parameters. The inset shows the intensity dependence of the photocurrent measured diagonal between the contacts 3 and 6, see Fig. 10, excited by linearly polarized radiation with a frequency of $f = 0.6\,\mathrm{THz}$. The solid line displays a fit after Eq. (78) with the coefficients $\chi_c = 2.7 \times 10^{-13}\,\mu\mathrm{Acm^4/kW}$ and $\chi_v = 6 \times 10^{-12}\,\mu\mathrm{Acm^4/kW}$ as fitting parameters. Figure adapted from Ref. [35].

the valence band can be an order of magnitude larger than the contribution from electrons in the conduction band. The detailed analysis of these computations are out of scope of this work. Assuming circularly polarized radiation ($\varphi = 45°$ or $\varphi = 135°$) instead of linear polarization, Eqs. (79) are simplified to

$$\chi_{c,x} = \kappa\chi^{(0)}_{c,x}\,, \chi_{v,x} = \kappa\chi^{(0)}_{v,x}\,. \tag{80}$$

In the experiments, a lower inversion intensity $I^{\mathrm{C}}_{\mathrm{inv}}$ has been detected for circular polarization compared to the inversion intensity for linear polarization $I^{\mathrm{L}}_{\mathrm{inv}}$, see Figs. 17(a) and 17(b). Comparing Eqs. (79) and (80), $I^{\mathrm{C}}_{\mathrm{inv}} < I^{\mathrm{L}}_{\mathrm{inv}}$ is

equivalent to

$$\left|\frac{\chi_{v,x}^{(0)}+\chi_{v,x}^{(1)}}{\chi_{c,x}^{(0)}+\chi_{c,x}^{(1)}}\right| < \left|\frac{\chi_{v,x}^{(0)}}{\chi_{c,x}^{(0)}}\right| . \tag{81}$$

Additionally, different inversion points for the x-direction and diagonal directions were detected in the experiments, compare Fig. 29 and inset in Fig. 29. This difference comes from the fact that hole and electron current are not parallel due to the asymmetry caused by the C_1-symmetry induced by the (013)-oriented substrate, see also Eqs. (74) and (75). The observed larger inversion intensity for the diagonal contacts I_{inv}, see inset in Fig. 29, compared to the corresponding inversion intensity in the x-direction is equivalent to

$$\left|\frac{\chi_{v,x}}{\chi_{c,x}}\right| > \left|\frac{\chi_{v,y}}{\chi_{c,y}}\right| . \tag{82}$$

Finally, the rise of the inversion intensity with increasing temperature, see main figure and inset in Fig. 18, is also explained by the combined theory of light impact ionization and the shift photocurrent: As the temperature rises the ionization rate decreases due to increasing energy losses on phonons as discussed for the photoconductivity results in the previous section. This leads to less holes being created increasing the temperature at a given intensity, and, thus, the inversion intensity rises with the temperature.

In summary, the results in this chapter demonstrate that the illumination of HgTe QWs by intense terahertz radiation leads to the emergence of strongly nonlinear photocurrents and photoconductivity. These effects arise in samples with parabolic and almost linear dispersion and are caused by the phenomenon of light impact ionization in the high-frequency regime, where $\omega\tau > 1$ is valid. Moreover, this phenomenon is first reported in a system where the Fermi energy is much larger than the energy gap. The theoretical model developed alongside the experiments considers that in such systems electron gas heating is needed to deplete occupied conduction band states in order to make the impact ionization process possible.

5 Circular photogalvanic effect in CdHgTe films

5.1 Nonlinearities in CdHgTe films

In the framework of this thesis, optoelectronic phenomena were also studied in bulk $Cd_xHg_{1-x}Te$ in addition to HgTe QWs. These experiments have been conducted in order to check if the nonlinearity, and, consequently, light impact ionization is also a dominant mechanism in other structures. Indeed, a similar picture was detected in $Cd_xHg_{1-x}Te$ sample #C measuring the intensity dependence of the photocurrent excited by a high-power pulsed laser. This is exemplarily shown for a radiation frequency of 3.3 THz and a temperature of $T = 4\,\mathrm{K}$ in Fig. 30. Similar to the results in HgTe QWs, see e.g. Fig. 17, the photocurrent exhibits a change of sign with increasing radiation intensity. Note that $Cd_xHg_{1-x}Te$ sample #C features an almost linear dispersion with a small band gap of $\varepsilon_g = 20\,\mathrm{meV}$. This result demonstrates that the process of light impact ionization is of a more general, fundamental origin. Since the band gap is similar to the gap in the studied HgTe QWs and the photocurrent behavior is very close to the already discussed nonlinear photocurrents in HgTe QWs, see Sec. 4.3.2, the nonlinear photocurrents in $Cd_xHg_{1-x}Te$ were not investigated further. But surprisingly, in these samples also a contribution of the CPGE was detected, which is discussed in the following section.

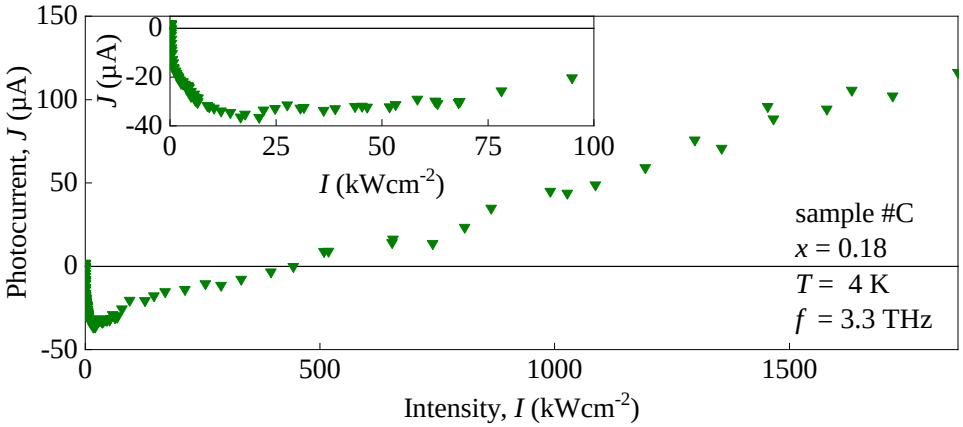

Figure 30: Photocurrents between contacts 2 and 5 [see Fig. 10 (b)] as a function of radiation intensity measured at $T = 4\,\mathrm{K}$ in the $Cd_xHg_{1-x}Te$ wafer #C with a Cd concentration of $x = 0.18$. Here, a pulsed laser at a radiation frequency of 3.3 THz was used. The inset shows a zoom-in for low intensities.

5.2 Circular photocurrent

The CPGE was initially observed in samples #A and #B with a Cd concentration of $x = 0.15$ at liquid helium temperature. At these temperature, samples #A and #B exhibit a negative band gap and, thus, topologically non-trivial behavior. In Fig. 31 the photocurrent normalized by the radiation power is shown as a function of the phase angle φ corresponding to the rotation of a quarter-wave plate, as described in Sec. 3.2.2. These data were obtained for cw radiation with a power in the range of a few mW and frequencies of 1.63 and 2.54 THz. The dependences are fitted by

$$J = J_c \sin(2\varphi) + J_0 + J_{L1}\frac{\cos(4\varphi)+1}{2} + J_{L2}\frac{\sin(4\varphi)}{2} \tag{83}$$

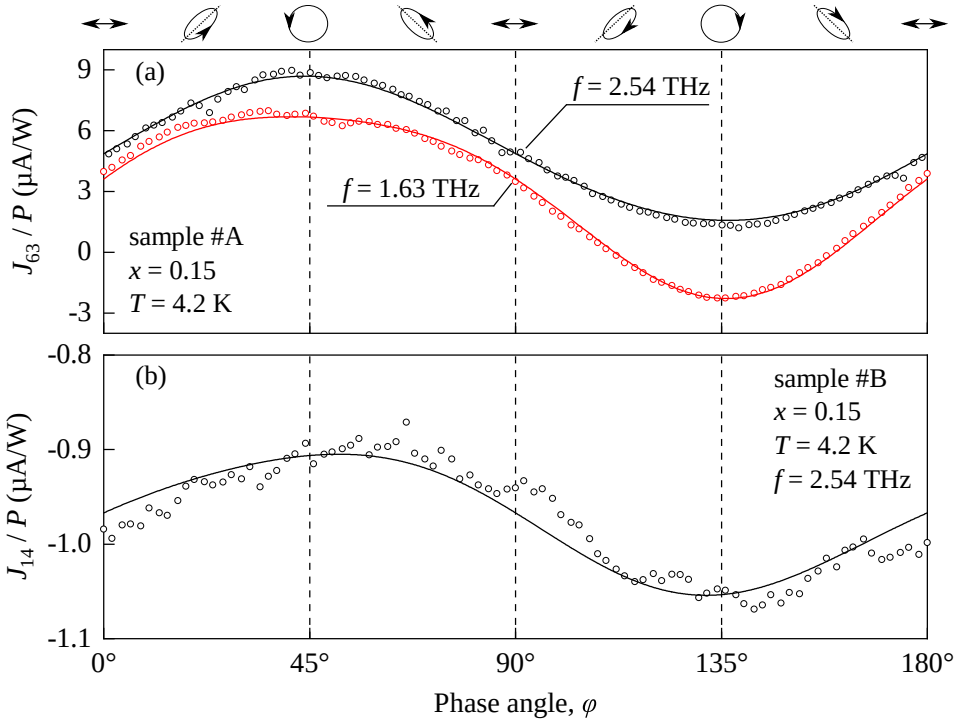

Figure 31: Dependency of the photocurrents between contacts 6 and 3 (a) and 1 and 4 (b), see Fig. 10 (b), on the radiation helicity measured at $T = 4$ K in the $Cd_xHg_{1-x}Te$ wafers #A and #B with an Cd concentration of $x = 0.15$. Note that the photocurrents are normalized to the radiation power P. As a radiation source a low power cw laser operating at frequencies 1.63 and 2.54 THz was used. The solid curves show fits according to Eq. (83). The corresponding fitting parameters are shown in Tab. 1. On top of the figure the polarization state is sketched for important phase angles. Adapted from Ref. [82]

The figure reveals that the total photocurrent is dominated by the circular photocurrent contribution proportional to J_c, which is characterized by a change of sign for opposite helicities. Note that a second major contribution comes from the polarization-independent offset photocurrent J_0. The contributions proportional to the degrees of linear polarization, namely J_{L1} and J_{L2}, have a significantly smaller amplitude compared to J_c and J_0. Previous works already showed that polarization-independent photocurrents (J_0) and photocurrents proportional to the degree of linear polarization ($J_{\mathrm{L1}}, J_{\mathrm{L2}}$) can be excited by terahertz radiation in $Cd_xHg_{1-x}Te$ by photogalvanic and photon drag effects [32, 37, 56]. Circular photocurrent contributions due to photogalvanics or photon drag effects, however, are forbidden by symmetry arguments in $Cd_xHg_{1-x}Te$ crystals [82]. Thus, the origin of the observed circular photocurrent contribution is investigated further.

Since the Cd concentration of samples #A and #B ($x = 0.15$) is lower than the critical one for $T = 4\,\mathrm{K}$ their band ordering is inverted. Consequently, these samples host topological two-dimensional surface states. The symmetry of these two-dimensional states is reduced and, therefore, circular photocurrent contributions become possible. In order to verify if these surface states play a crucial role in the generation of the observed circular photocurrent in $Cd_xHg_{1-x}Te$, measurements were carried out with samples #C having an almost linear dispersion at $T = 4\,\mathrm{K}$, and #D exhibiting a normal band ordering. Note that the Cd concentration in both samples is higher than the critical one for liquid helium temperature and, consequently, these samples do not host topological surface states.

The corresponding measurement data is shown in Fig. 32, where a low-power cw laser at the frequency lines $f = 1.63\,\mathrm{THz}$ and $f = 0.69\,\mathrm{THz}$ was used. Surprisingly, the fit of the data according to Eq. (83) again reveals an large circular photocurrent contribution J_c. These results for the topologically trivial samples #C and #D exclude the band inversion and the resulting topological surface states as requirement for the circular photocurrent in $Cd_xHg_{1-x}Te$ films. Further measurements with an high-power pulsed laser additionally revealed that the circular photocurrent is also detectable at room temperature. The corresponding data is shown in Fig. 33 for the samples #A and #C. Note that at room temperature all $Cd_xHg_{1-x}Te$ samples used in this work exhibit a normal band ordering and, thus, no topological surface states exist under this condition.

To summarize the experimental part on $Cd_xHg_{1-x}Te$ films, the experiments

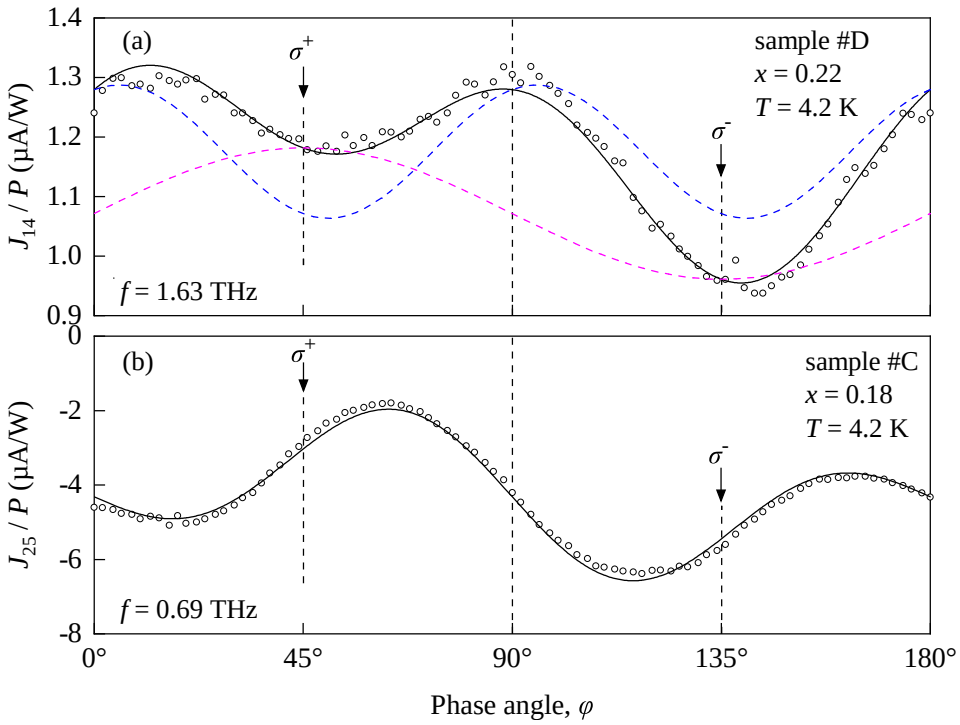

Figure 32: Dependency of the photocurrents between contacts 1 and 4 (a) and 2 and 5 (b), see Fig. 10 (b), on the radiation helicity measured at $T = 4\,\mathrm{K}$ in the $Cd_xHg_{1-x}Te$ wafers #D (Cd concentration $x = 0.22$) and #C (Cd concentration $x = 0.18$) excited by radiation frequencies of $f = 1.63\,\mathrm{THz}$ (Panel (a)) and $f = 0.69\,\mathrm{THz}$ (Panel (b)). Note that the photocurrents are normalized to the radiation power P. A low-power cw laser was used as a radiation source. The solid curves show fits after Eq. (83). The magenta dashed line in (a) shows the photocurrent contribution J_c proportional to the degree of circular polarization P_{circ} (first term in Eq. (83)), the dashed blue curve depicts the contribution J_{L2} proportional to the degree of linear polarization P_{L2} (last term in Eq. (83)). Both dashed lines are shifted by the value of the offset photocurrent J_0. The corresponding fitting parameters are shown in Tab. 1. Adapted from Ref. [82]

show that circular photocurrent can be generated by terahertz radiation in $Cd_xHg_{1-x}Te$ films in samples with normal band ordering, in samples with an inverted band ordering and in samples with almost linear dispersion. Since the circular photocurrent contribution is also detected in samples above the critical Cd concentration, the symmetry breaking in topological surface states is excluded as a requirement for the photocurrent generation.

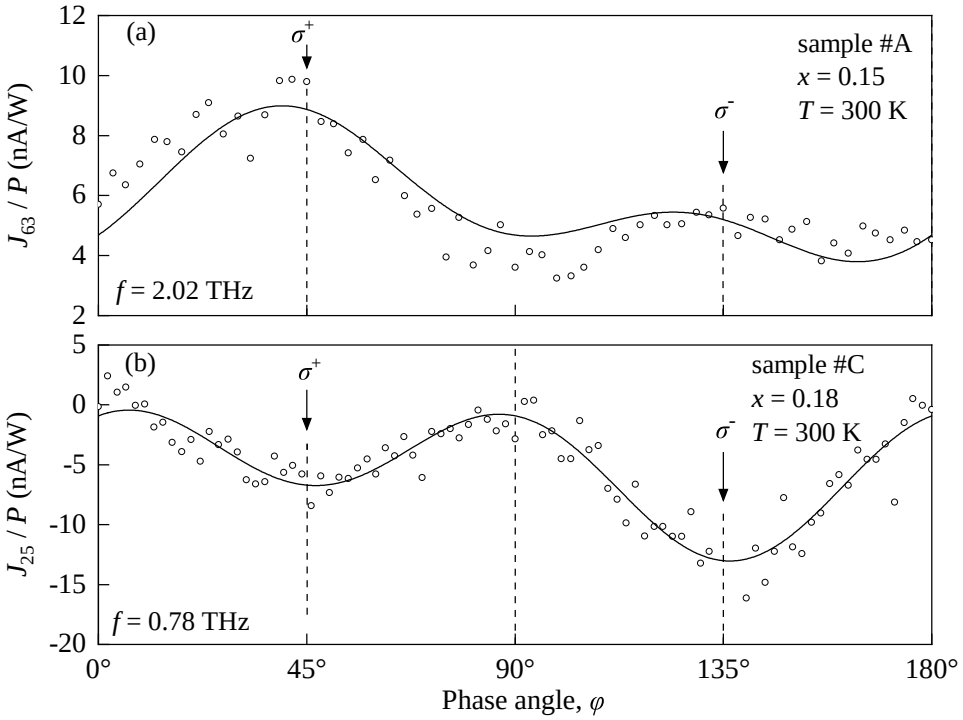

Figure 33: Dependence of photocurrents between contacts 6 and 3 (a) and 2 and 5 (b) [see Fig. 10 (b)] on the radiation helicity measured at room temperature in the $Cd_xHg_{1-x}Te$ wafers #A (Cd concentration $x = 0.15$) and #C (Cd concentration $x = 0.18$). Note that the photocurrents are normalized to the radiation power P. As a radiation source the high-power pulsed terahertz laser (see Sec. 3.2.1) with a power of $P \approx 4\,\mathrm{kW}$ and the frequency lines $f = 2.02\,\mathrm{THz}$ (Panel (a)) and $f = 0.78\,\mathrm{THz}$ (Panel(b)) was used. The solid black curves show a fit according to Eq. (83). The corresponding fitting parameters are shown in Tab. 1. Adapted from Ref. [82].

5.3 Discussion

Bulk $Cd_xHg_{1-x}Te$ crystallizes in zinc-blende structure and, thus, it is characterized by the T_d point group symmetry. On the one hand, this structure does not have a center of inversion, which allows photogalvanic effects induced by terahertz radiation. On the other hand, the material is not gyrotropic, which forbids the appearance of the CPGE, see Sec. 2.2 and Refs. [37, 82]. In order to make the formation of the CPGE possible in bulk $Cd_xHg_{1-x}Te$, the symmetry has to be reduced further. In this work, static strain emerging from, e.g., lattice mismatches at the interfaces is considered as the main cause of this symmetry reduction [106]. Please note that in samples #A and #B at low temperatures topological states are present, see Sec. 2.1.3 and Refs. [19, 107], which can also contribute to the CPGE as shown analogously for HgTe

Sample	Temp., T(K)	Frequency, f(THz)	J_c/P (nA/W)	J_0/P (nA/W)	J_{L1}/P (nA/W)	J_{L2}/P (nA/W)
#A	4.2	2.54	3600	5100	-300	150
#A	4.2	1.63	4500	2200	1400	260
#B	4.2	2.54	74	980	13	-12
#C	4.2	0.69	1200	-4200	-77	-2800
#D	4.2	1.63	100	1100	208	82
#A	300	2.02	1.8	7	2.3	1.3
#C	300	0.78	3.2	-9.9	9	1

Table 1: Fitting parameters J_c/P, J_0/P, J_{L1}/P and J_{L2}/P used in Figs. 31-33 for the fits according to Eq. (83).

2D topological insulators [23, 65]. The discussion below follows Ref. [82] using the theoretical model developed in parallel to the experiments by G.V. Budkin and S.A. Tarasenko from the Ioffe Institute in St. Petersburg, Russia.

Considering the first order in strain, the CPGE photocurrent density can phenomenologically be written as a function of the strain tensor $\boldsymbol{u}$ in the following way

$$\begin{aligned} j_{x'} &= [\chi_1(u_{y'y'} - u_{z'z'})\hat{e}_{x'} + \chi_2(u_{x'y'}\hat{e}_{y'} - u_{x'z'}\hat{e}_{z'})]IP_{\mathrm{circ}}, \\ j_{y'} &= [\chi_1(u_{z'z'} - u_{x'x'})\hat{e}_{y'} + \chi_2(u_{y'z'}\hat{e}_{z'} - u_{x'y'}\hat{e}_{x'})]IP_{\mathrm{circ}}, \\ j_{z'} &= [\chi_1(u_{x'x'} - u_{y'y'})\hat{e}_{z'} + \chi_2(u_{x'z'}\hat{e}_{x'} - u_{y'z'}\hat{e}_{y'})]IP_{\mathrm{circ}}, \end{aligned} \tag{84}$$

where I is the radiation intensity, $x' \parallel [100]$, $y' \parallel [010]$, and $z' \parallel [001]$ are the cubic axes, $\hat{e} = \boldsymbol{q}/q$ is the unit vector in the direction of the photon wave vector $\boldsymbol{q}$, and P_{circ} is the degree of circular polarization defined according to Eq. (31). The phenomenological coefficients χ_1 and χ_2 denote the photocurrent contributions emerging due to normal and shear strain [106]. Hydrostatic strain, however, is not considered, as this type of strain does not reduce the crystal symmetry and, consequently, does not lead to the generation of a CPGE contribution. In this work structures grown on (013) substrates have been investigated. In this orientation, the strain tensor $\boldsymbol{u}$ has the four non-vanishing components u_{xx}, u_{yy}, u_{zz}, and u_{yz}, considering the coordinates $x \parallel [100]$, $y \parallel [03\overline{1}]$, and $z \parallel [013]$ corresponding to the orientation of the structure. The values of u_{xx} and u_{yy} are identical and are generally defined by the lattice mismatch between $Cd_xHg_{1-x}Te$ and the buffer layer (CdTe). The components u_{zz} and u_{yz} can be calculated considering the minimum of the elastic energy

[108]. In the experiments conducted for this work, the photocurrent was always excited by normally incident radiation, i.e., $\hat{\boldsymbol{e}} \parallel z$. Considering this geometry and the coordinate frame defined above, Eqs. (84) simplify to

$$\begin{aligned} j_y &= \left[(\chi_1 + \chi_2)(u_{zz} - u_{yy}) \frac{\sin 2\phi}{2} + \chi_2 u_{yz} \cos 2\phi \right] I P_{\mathrm{circ}} \,, \\ j_z &= -\chi_1 u_{yz} \sin 2\phi \, I P_{\mathrm{circ}} \,, \end{aligned} \tag{85}$$

where $\phi = \arctan(1/3)$ describes the angle between [001] and [013]. Note that the helicity-sensitive photocurrent detected in the experiments (see Figs. 31, 32, 33) always corresponds to the in-plane photocurrent j_y in Eq. (85). The setup and sample geometry used in this work do not allow a detection of the out-of-plane component of the photocurrent density j_z.

While the considerations done above purely rely on the symmetry analysis, now a microscopical model of the photocurrent generation is given according to Ref. [82]. For this, $Cd_xHg_{1-x}Te$ with an concentration x below the critical concentration x_c is assumed, i.e. no topological states are considered as present in the structure. Then the dispersion is non-inverted with the Γ_8 valence band below the Γ_8 conduction band and the band gap ε_{g} is much larger than the photon energy $\hbar\omega$ of terahertz radiation. The Fermi energy lies in the conduction band and, consequently, free carriers are present. Due to these circumstances, the radiation is absorbed by indirect optical transitions in the conduction band, see Fig. 34. These Drude-like transitions include scattering by phonons or defects in order to fulfill energy and quasi-momentum conservation.

Theoretically, these kinds of transitions can be described by perturbation theory in the second order and considering intermediate states during virtual processes. The transition matrix element M_{fi} describing the real transition from the initial state $i = (\boldsymbol{k}, s)$ with wave vector $\boldsymbol{k}$ and spin state s to the final state $f = (\boldsymbol{k}', s')$ with the corresponding wave vector $\boldsymbol{k}'$ and spin s' is then determined by the summation over all matrix elements of virtual transitions via all possible intermediate states j:

$$M_{\boldsymbol{k}'s',\boldsymbol{k},s} = M_{fi} = \sum_j \left(\frac{V_{fj} R_{ji}}{\varepsilon_i - \varepsilon_j} + \frac{R_{fj} V_{ji}}{\varepsilon_i - \varepsilon_j} \right) . \tag{86}$$

Here V_{fj} is the electron scattering matrix element from state j to f, while R_{ji}

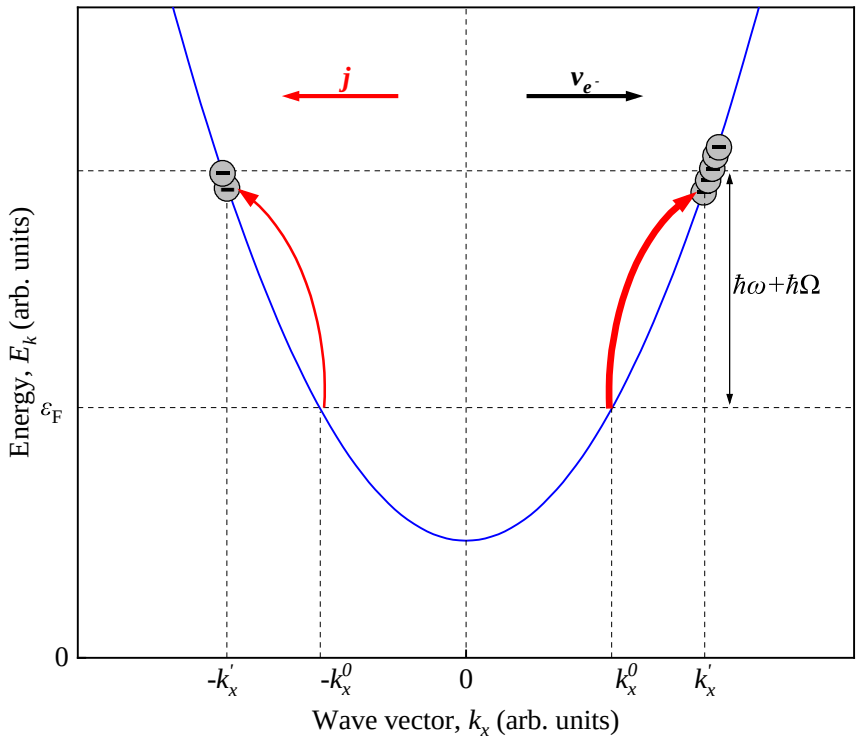

Figure 34: Model sketch of the photocurrent generation caused by Drude-like indirect optical transition. Terahertz radiation with angular frequency ω gets absorbed while a phonon with angular frequency Ω is spontaneously emitted/absorbed. In the case of circularly polarized radiation, the transition probability for negative and positive k values is asymmetric as depicted by thick and thin red arrows leading to a photocurrent. The asymmetry in the transition probability is caused by the interference of pathway matrix elements, see Fig. 35. Adapted from Ref. [82].

describes the electron-photon interaction matrix element from state i to state j and ε_i is the energy in the state i. The majority of the absorption is caused by transitions, where the intermediate states are located in the conduction band, see Figs. 35(a) and 35(b). These transitions involve processes with photon absorption followed by subsequent scattering (Fig. 35(a)) and processes with the opposite order (Fig. 35(b)). These two transition processes describe the Drude absorption, but they are neither sensitive to the radiation helicity, nor do they cause an asymmetry in the $\boldsymbol{k}$-space, i.e., they do not generate a photocurrent. Consequently, in order to describe the photocurrent generation, also virtual transitions involving virtual states located in the valence band are considered. Four of these possible transition processes including virtual transitions via states in the heavy- and light hole band are shown in Figs. 35(c)-35(f). These processes, however, are sensitive to the radiation helicity due to selection

rules [109], unlike the transitions via virtual states in the conduction bands. Since the band gap in the studied $Cd_xHg_{1-x}Te$ structures is small, the contribution made by the transitions with intermediate states in the valence band is comparatively larger. This follows from Eq. (86), where the denominator is proportional to ε_g in the case of such a transition.

Separating the matrix element (Eq. (86)) into the parts coming from transitions from the conduction bands $M_{fi}^{(c)}$ and the corresponding part caused by transitions via the valence bands $M_{fi}^{(v)}$, it can be written:

$$M_{fi} = M_{fi}^{(c)} + M_{fi}^{(v)} \tag{87}$$

The transition probability from the state $i = (\boldsymbol{k}, s)$ to the state $f = (\boldsymbol{k}', s')$ can be calculated by the squared absolute value of the matrix element M_{fi}. Consequently, it follows

$$|M_{fi}|^2 = \left|M_{fi}^{(c)} + M_{fi}^{(v)}\right|^2 = \left|M_{fi}^{(c)}\right|^2 + \left|M_{fi}^{(v)}\right|^2 + 2\mathrm{Re}\left[M_{fi}^{(c)*} M_{fi}^{(v)}\right] , \tag{88}$$

where the asterisk denotes the complex conjugation. Eq. (88) shows that the transition probability depends on the two separate probabilities for the transitions via virtual states in the conduction/valence band as well as on the interference term $2\mathrm{Re}\left[M_{fi}^{(c)*} M_{fi}^{(v)}\right]$. This term can only be nonzero in crystals without an inversion center and causes the helicity-sensitive contribution of the photocurrent, i.e., the CPGE [110]. As discussed above with symmetry arguments, the CPGE can only emerge in strained $Cd_xHg_{1-x}Te$ structures. The static strain results in a mixing of the states, which is sketched in Fig. 35 as a distortion of the valence bands.

The non-centrosymmetric structure of the $Cd_xHg_{1-x}Te$ crystal combined with the strain-induced mixing of the states are the two prerequisites for the CPGE in $Cd_xHg_{1-x}Te$. The corresponding photocurrent is calculated considering these two factors and the electron scattering by acoustic phonons. Since the band gap ε_g is much smaller than the energies of the higher conduction bands and the split-off valence bands, only the first conduction band, the light-hole band and the heavy-hole band are considered. The system is then described by a six-band Kane Hamiltonian [10, 109]. The following microscopic calculations of the matrix elements and, consequently, the photocurrent, is cumbersome and described in [82]. For brevity, only the result for the in-plane photocurrent j_y.

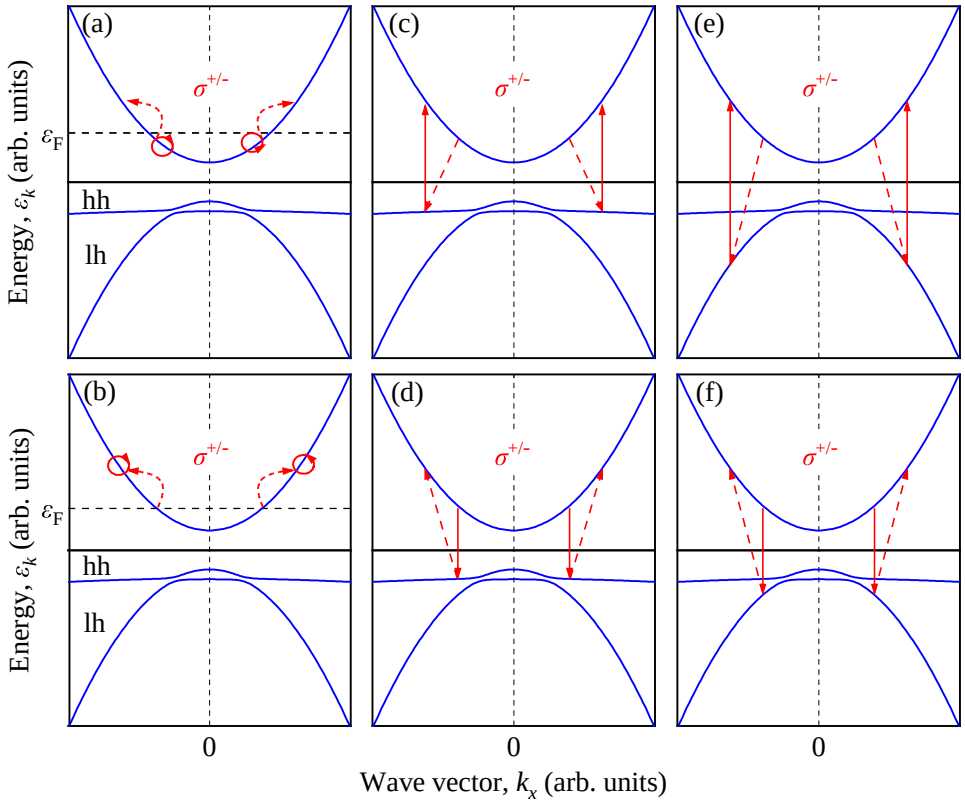

Figure 35: Sketch of virtual intraband transitions excited by circularly polarized radiation with different intermediate states. The red circles represent the interaction between electron and photon, while the curved arrows show the electron scattering. Panels (a) and (b): Virtual intraband transitions with intermediate states in the conduction band. In (a) the absorption of a photon is followed by subsequent scattering, while the reverse order of processes is sketched in (b). Panels (c-f): Virtual intraband transitions with intermediate states in the heavy- and light-hole bands. The distortion of the valence band spectrum around $k = 0$ is caused by the mixing of light-hole and heavy-hole states caused by static strain, which is crucial for the emergence of the CPGE in zinc-blende crystals. Adapted from Ref. [82].

is provided here. The calculations yield

$$\chi_1 = -\frac{64\pi}{35}\frac{e^3 N_e b}{\hbar^2 \omega\, c\, n_\omega}\frac{\Xi_{\rm cv}}{\Xi_{\rm c}}\frac{P^3}{\varepsilon_g^4}\,, \quad \chi_2 = -(5/3)\chi_1\,, \tag{89}$$

and, consequently, using Eq. (85):

$$j_y = \frac{64\pi}{21}\frac{e^3 n_0 b}{\hbar^2 \omega c n_\omega}\frac{\Xi_{\rm cv}}{\Xi_{\rm c}}\frac{P^3}{\varepsilon_{\rm g}^4}\cdot\left[\frac{2}{5}(u_{zz}-u_{yy})\frac{\sin 2\phi}{2} - u_{yz}\cos 2\phi\right] I P_{\rm circ}\,. \tag{90}$$

Here, n_0 is the electron density, b is the valence-band deformation potential,

n_ω is the refractive index of the $Cd_xHg_{1-x}Te$ structure, Ξ_c and Ξ_{cv} are the conduction and interband deformation potentials, and P is the Kane parameter [99]. Note that Eq. (90) is only valid for frequencies fulfilling $\omega\tau \gg 1$ and $\hbar\omega \ll \varepsilon_g$, where τ is the relaxation time. The theoretical Eq. (90) describes well the characteristic dependence on the phase angle φ, see Figs. 31-33, see also Eq. (31). Additionally, the equation proposes a strong dependence of the photocurrent on the band gap $j_y \propto \varepsilon_g^{-4}$ and an inverse proportionality on the frequency $j_y \propto \omega^{-1}$. Please note that the helicity-dependent current density j_y is termed j_c in the following and is related to the measured circular photocurrent J_c by

$$j_c/I = J_c/P \cdot A_{\text{beam}}/(d \cdot d_{\text{beam}}) \,, \tag{91}$$

where A_{beam} and d_{beam} are area and diameter of the laser beam on the sample, P and I are radiation power and intensity, and d is the width of the conducting channel in the sample.

The results shown in the experimental part were obtained with samples having different values of the Cd concentration x and, consequently, the band gap ε_g [18, 19]: At constant temperature the band gap increases with the Cd concentration and, according to Eq. (90) the circular photocurrent should decrease. Exactly this behavior is seen in Fig. 36 where the normalized circular photocurrent parameter obtained from fitting the data from Figs. 31-33 is plotted against the Cd concentration. Note that the data was normalized to the radiation frequency, as suggested by Eq. (90), where $J_c \propto \omega^{-1}$ is proposed. This normalization is justified as shown by the inset in Fig. 36, where the circular photocurrent is plotted against the frequency following $J_c \propto f^{-1}$. The corresponding data values for J_c, the band gap, and other properties are given in Tab. 2. Additionally, Fig. 36 reveals that J_c increases by orders of magnitude for all samples changing the temperature from room temperature to 4.2 K. This is also in line with Eq. (90), since the decrease of the temperature leads to an decrease of the band gap according to Refs. [18, 19] and, consequently, to an decrease of the photocurrent, since $J_c \propto \varepsilon_g^{-4}$. However, note that Eq. (90) is not valid for samples #A and #B at liquid helium temperature, since these samples have a negative band gap under these circumstances. Due to this fact the following discussion is given using the results at room temperature, where Eq. (90) can be applied for all samples.

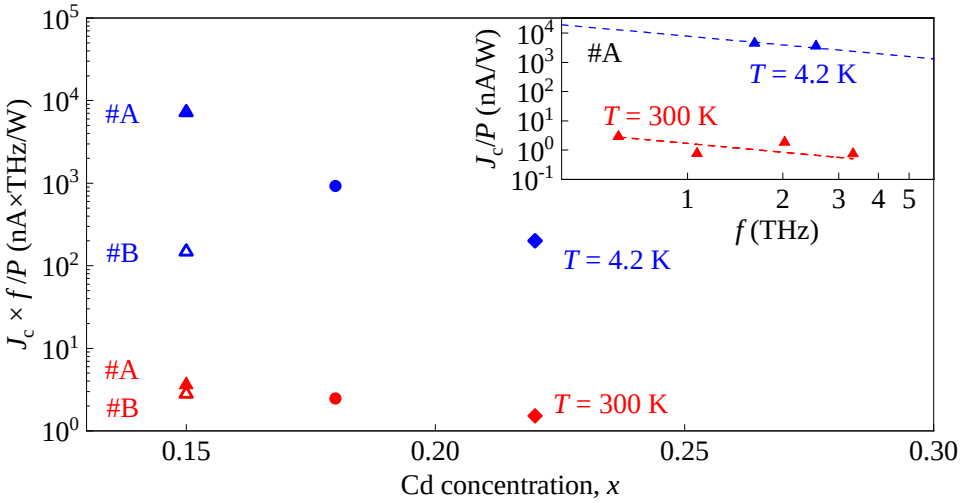

Figure 36: Dependence of the helicity-dependent photocurrent contribution normalized by radiation power and frequency on the Cd concentration x for the temperatures $T = 4.2\,\mathrm{K}$ (blue) and $T = 300\,\mathrm{K}$ (red). In the inset the dependence of the helicity-dependent photocurrent contribution normalized by the radiation power is plotted against the radiation frequency. At the temperatures $T = 4.2\,\mathrm{K}$ (blue) and $T = 300\,\mathrm{K}$ (red). The dashed lines show a fit according to $J_c/P \propto f^{-1}$, see Eq. (90). Adapted from Ref. [82].

Using the data obtained at room temperature, the value of the strain

$$u = \frac{2}{5}(u_{zz} - u_{yy})\frac{\sin 2\phi}{2} - u_{yz}\cos 2\phi \tag{92}$$

can then be estimated. This estimation is reasonable for the room temperature data only, because at liquid helium temperature free carriers and the photocurrent can be spread inhomogeneously across the sample. For the estimations, n_0 was extracted from corresponding magnetotransport measurements the band gap was calculated according to Refs. [18, 19] and the values $2m_0(P/\hbar)^2 = 18.8\,\mathrm{eV}$ [111], $b = -1.4\,\mathrm{eV}$, $n_\omega = 4.6$ [112], and $\Xi_{cv}/\Xi_c = 0.3$ [113] were used. Note that since Ξ_{cv}/Ξ_c is unknown for HgTe the values for GaAs was used. The results of the estimation are presented in the last column of Tab. 2. The values ranging from 1.6×10^{-7} to 6.9×10^{-6} are well below the maximal strain u_{max} estimated for HgTe in Ref. [108]. The result that the values for the strain are many orders of magnitude smaller than u_{max} is reasonable, since the $Cd_xHg_{1-x}Te$ used in this work are rather thick (several µm). In that case, the strain is strongest at the bottom interface, and decreases going in positive z direction (see sample sketch in Fig. 12). Note that this estimation bases on the strain being the only source for the CPGE in the

Sample	x	f (THz)	J_c/P (nA/W)	j_c/I (µA/W)	n_0 (cm^{-3})	ε_g (meV)	u (10^{-6})
#A	0.15	2.02	1.8	1.24	1.8×10^{17}	83	0.4
#B	0.15	2.02	1.4	1.0	1.3×10^{17}	83	0.5
#C	0.18	0.78	3.2	0.8	1.1×10^{17}	123	1.6
#D	0.22	2.02	0.7	0.2	4.1×10^{16}	182	6.9

Table 2: Experimental data for the helicity-dependent contribution of the normalized photocurrent, the normalized circular photocurrent density $j_c/I = J_c/P \cdot A_{\mathrm{beam}}/(d \cdot d_{\mathrm{beam}})$, carrier densities n_0, band gaps ε_{g} calculated according to Refs. [18, 19] and the estimated strain u for samples #A-#D at $T = 300\,\mathrm{K}$. Table adapted from Ref. [82].

studied $Cd_xHg_{1-x}Te$ films. Other symmetry-reducing mechanisms or interface effects can also give contributions to the CPGE as well as topological surface states in samples #A and #B at low temperatures.

Another possible contribution to the circular effect in $Cd_xHg_{1-x}Te$ films is the circular photon drag effect (circular dynamic Hall effect), which was already observed in GaAs QWs [114], bulk Te [115] and graphene [116, 117]. Here, momentum and angular momentum of the radiation are transferred to the charge carriers. This effect is symmetry-forbidden in materials with T_{d} point group symmetry just as the CPGE, so the symmetry reduction via lattice deformation has to be considered. Using the theory of irreducible representation, the helicity-dependent photon drag photocurrent density at normal incidence can be written as [82]

$$j_x^{(cpd)} = \{\alpha u_{yz} + \beta[2u_{yz}\cos 4\phi + (u_{zz} - u_{yy})\sin 4\phi]\}\, qP_{\mathrm{circ}}\, I\,. \tag{93}$$

Here, q is the radiation wave vector and the parameters α and β are independent constants. The ratio between the photon drag current amplitude and the CPGE amplitude can be estimated as

$$\frac{j^{(cpd)}}{j^{(cpge)}} \propto \frac{\bar{v}}{c}\frac{\tau}{\hbar/\varepsilon_{\mathrm{g}}}\frac{1}{\zeta}\,, \tag{94}$$

with the characteristic electron velocity $\bar{v} = P/\hbar$ and the scattering asymmetry parameter $\zeta = \Xi_{cv}/\Xi_c = 0.3$. For room temperature, the momentum relaxation time in the investigated samples can be approximated by $\tau \approx 50\,\mathrm{fs}$ and the band gap is around $\varepsilon_{\mathrm{g}} \approx 100\,\mathrm{meV}$. For this values, Eq. (94) yields $j^{(cpd)}/j^{(cpge)} \approx 0.1$ and, thus, the circular photon drag current is considered to

be an order of magnitude smaller than the CPGE contribution. Note that in the experimental conditions of Refs. [114, 116, 117] the CPGE was suppressed.

To sum up this chapter, the results on $Cd_xHg_{1-x}Te$ demonstrate the symmetry breaking in this structure, which causes the generation of a helicity-sensitive photocurrent contribution, i.e., the CPGE. This has been demonstrated in several $Cd_xHg_{1-x}Te$ films with different Cd concentration and at various temperatures. The experimental data are supported by a theoretical model based on second-order perturbation theory. This model shows that the CPGE emerges due to the interference of matrix elements belonging to Drude-like transitions involving virtual states in valence and conduction bands.

6 Conclusion

In this thesis terahertz-radiation induced optoelectronics were studied in HgTe-based structures revealing several exciting results. It was demonstrated that excitation of HgTe-based structures with intense terahertz radiation leads to the appearance of strongly nonlinear photocurrent and photoconductivity. These effects are caused by the phenomenon of light impact ionization, where electron-hole pairs are generated by terahertz radiation with a photon energy much smaller than the energy gap. This phenomenon was observed for the first time under the condition that the Fermi energy is larger than the energy gap. Moreover, the experiments in $Cd_xHg_{1-x}Te$ films demonstrated the appearance of a surprising CPGE, which is supposed to be caused by the strain-induced symmetry reduction of the system. All of these experimental results were shown and discussed in Chaps. 4 and 5.

Initially, the optoelectronic phenomena observed in HgTe QWs have been discussed. Here, excitation by intense terahertz radiation results in a strongly nonlinear photocurrent, which changes its sign with increasing radiation intensity. This photocurrent was shown to be almost helicity-independent and stemming from the sample bulk. Investigations in a wide temperature range demonstrated that the nonlinearity decreases with an increase of the temperature. Further studies revealed that the nonlinear photocurrent is accompanied by a corresponding photoconductivity, which shows a characteristic, nonlinear intensity dependence proportional to $\exp(-E_0^2/E^2)$. Investigations with different frequencies demonstrated that the characteristic field E_0 is proportional to the radiation frequency. These characteristic dependencies are a fingerprint of light impact ionization in the high-frequency regime $\omega\tau > 1$ [34] and prove this effect as the origin of the nonlinearity. Studies in QWs with almost linear dispersion demonstrated that light impact ionization is also possible under these conditions. The data were discussed and analyzed applying the supporting theory by A.P. Dmitiriev and E.L. Ivchenko from the Ioffe Institute, St. Petersburg, which has been developed parallel to the experiments [35, 36].

This theory demonstrates that light impact ionization also occurs in systems with the Fermi energy higher than the impact ionization threshold energy. The developed model considers electron gas heating as a mechanism for the depletion of conduction band states, which are needed as final states of the impact ionization process. Moreover, the theory shows that the nonlinear photocurrent observed in the experiment is a consequence of the PGE on the electrons

and holes generated by the process of light impact ionization. Future studies in this field should include samples with a semitransparent gate, where the carrier density could be reduced in order to suppress the contribution of impact ionization. This could reveal contributions of other optoelectronic phenomena induced by intense terahertz radiation, e.g., multiphoton absorption [32, 97, 118], tunneling ionization [91, 119, 120], or the generation of a Floquet topological insulator [24].

In Chap. 5 the results obtained in $Cd_xHg_{1-x}Te$ films were presented. In this structures, similar nonlinear photocurrents were detected, proving the more general occurrence of light impact ionization. However, a surprising helicity-dependent photocurrent was also detected in this material. Since the CdHgTe material class crystallographically belongs to the non-gyrotropic T_d point group, such a CPGE should be forbidden in this material by symmetry arguments. Various experiments revealed the formation of the CPGE at different temperatures and Cd concentrations x and, consequently, excluded the formation of topological surface states as a driving force of the helicity-sensitive photocurrent. Furthermore, the data support the conclusion that the reduction of the crystal symmetry due to strain causes the formation of the CPGE. The theoretical model developed parallel to the experiments by G.V. Budkin and S.A. Tarasenko from the Ioffe Institute in St. Petersburg supports the experimental data using second order perturbation theory and the interference of transition matrix elements of virtual transitions in valence and conduction bands [82]. In future studies of terahertz-induced optoelectronics in bulk $Cd_xHg_{1-x}Te$, the role of helical surface states in the generation of the CPGE is an interesting topic for investigations.

References

[1] M. Henini and M. Razeghi, *Handbook of Infra-red Detection Technologies* (Elsevier Science, Amsterdam, 2002).

[2] A. Rogalski, *HgCdTe infrared detector material: history, status and outlook*, Rep. Prog. Phys. **68**, 2267–2336 (2005).

[3] S. A. Dvoretsky, N. N. Mikhailov, Y. G. Sidorov, V. A. Shvets, S. N. Danilov, B. Wittman, and S. D. Ganichev, *Growth of HgTe Quantum Wells for IR to THz Detectors*, J. Electron. Mater. **39**, 918 (2010).

[4] C. Downs and T. Vandervelde, *Progress in Infrared Photodetectors Since 2000*, Sensors **13**, 5054–5098 (2013).

[5] V. V. Rumyantsev, D. V. Kozlov, S. V. Morozov, M. A. Fadeev, A. M. Kadykov, F Teppe, V. S. Varavin, M. V. Yakushev, N. N. Mikhailov, S. A. Dvoretskii, and V. I. Gavrilenko, *Terahertz photoconductivity of double acceptors in narrow gap HgCdTe epitaxial films grown by molecular beam epitaxy on GaAs(013) and Si(013) substrates*, Semicond. Sci. Technol. **32**, 095007 (2017).

[6] S. Ruffenach, A. Kadykov, V. V. Rumyantsev, J. Torres, D. Coquillat, D. But, S. S. Krishtopenko, C. Consejo, W. Knap, S. Winnerl, M. Helm, M. A. Fadeev, N. N. Mikhailov, S. A. Dvoretskii, V. I. Gavrilenko, S. V. Morozov, and F. Teppe, *HgCdTe-based heterostructures for terahertz photonics*, APL Materials **5**, 035503 (2017).

[7] D. Yavorskiy, K. Karpierz, M. Baj, M. Bąk, N. Mikhailov, S. Dvoretsky, V. Gavrilenko, W. Knap, F. Teppe, and J. Usakowski, *Magnetoconductivity and Terahertz Response of a HgCdTe Epitaxial Layer*, Sensors **18**, 4341 (2018).

[8] M. Bąk, D. Yavorskiy, K. Karpierz, J. Łusakowski, D. But, J. Przybytek, I. Yahniuk, G. Cywiński, W. Knap, F. Teppe, S. Krishtopenko, N. Mikhailov, S. Dvoretsky, and V. Gavrilenko, *Magnetoconductivity of a Mercury Cadmium Telluride Resonant THz Detector*, Acta Phys. Pol. A **134**, 973–977 (2018).

[9] N. Vanamala, K. C. Santiago, and N. C. Das, *Enhanced MWIR absorption of HgCdTe (MCT) via plasmonic metal oxide nanostructures*, AIP Advances **9**, 025113 (2019).

[10] N. N. Berchenko and M. V. Pashkovskii, *Mercury telluride - a zero-gap semiconductor*, Sov. Phys. Usp. **19**, 462 (1976).

[11] B. A. Bernevig, T. L. Hughes, and S.-C. Zhang, *Quantum Spin Hall Effect and Topological Phase Transition in HgTe Quantum Wells*, Science **314**, 1757–1761 (2006).

[12] M. König, S. Wiedmann, C. Brüne, A. Roth, H. Buhmann, L. W. Molenkamp, X.-L. Qi, and S.-C. Zhang, *Quantum Spin Hall Insulator State in HgTe Quantum Wells*, Science **318**, 766 (2007).

[13] L. Fu, C. L. Kane, and E. J. Mele, *Topological Insulators in Three Dimensions*, Phys. Rev. Lett. **98**, 106803 (2007).

[14] D. Hsieh, Y. Xia, D. Qian, L. Wray, J. H. Dil, F. Meier, J. Osterwalder, L. Patthey, J. G. Checkelsky, N. P. Ong, A. V. Fedorov, H. Lin, A. Bansil, D. Grauer, Y. S. Hor, R. J. Cava, and M. Z. Hasan, *A tunable topological insulator in the spin helical Dirac transport regime*, Nature **460**, 1101 (2009).

[15] M. Z. Hasan and C. L. Kane, *Colloquium: Topological insulators*, Rev. Mod. Phys. **82**, 3045 (2010).

[16] J. E. Moore, *The birth of topological insulators*, Nature **464**, 194 (2010).

[17] B. Büttner, C. X. Liu, G. Tkachov, E. G. Novik, C. Brüne, H. Buhmann, E. M. Hankiewicz, P. Recher, B. Trauzettel, S. C. Zhang, and L. W. Molenkamp, *Single valley Dirac fermions in zero-gap HgTe quantum wells*, Nature Phys. **7**, 418–422 (2011).

[18] J. P. Laurenti, J. Camassel, A. Bouhemadou, B. Toulouse, R. Legros, and A. Lusson, *Temperature dependence of the fundamental absorption edge of mercury cadmium telluride*, J. Appl. Phys. **67**, 6454–6460 (1990).

[19] F. Teppe, M. Marcinkiewicz, S. S. Krishtopenko, S. Ruffenach, C. Consejo, A. M. Kadykov, W. Desrat, D. But, W. Knap, J. Ludwig, S. Moon, D. Smirnov, M. Orlita, Z. Jiang, S. V. Morozov, V. Gavrilenko, N. N. Mikhailov, and S. A. Dvoretskii, *Temperature-driven massless Kane fermions in HgCdTe crystals*, Nat. Commun. **7**, 12576 (2016).

[20] M. Orlita, D. M. Basko, M. S. Zholudev, F. Teppe, W. Knap, V. I. Gavrilenko, N. N. Mikhailov, S. A. Dvoretskii, P. Neugebauer, C. Faugeras, A.-L. Barra, G. Martinez, and M. Potemski, *Observation of three-dimensional massless Kane fermions in a zinc-blende crystal*, Nat. Phys. **10**, 233–238 (2014).

[21] J. D. Malcolm and E. J. Nicol, *Magneto-optics of massless Kane fermions: Role of the flat band and unusual Berry phase*, Phys. Rev. B **92**, 035118 (2015).

[22] K. C. Nowack, E. M. Spanton, M. Baenninger, M. König, J. R. Kirtley, B. Kalisky, C. Ames, P. Leubner, C. Brüne, H. Buhmann, L. W. Molenkamp, D. Goldhaber-Gordon, and K. A. Moler, *Imaging currents in HgTe quantum wells in the quantum spin Hall regime*, Nat. Mater. **12**, 787–791 (2013).

[23] K.-M. Dantscher, D. A. Kozlov, M. T. Scherr, S. Gebert, J. Bärenfänger, M. V. Durnev, S. A. Tarasenko, V. V. Bel'kov, N. N. Mikhailov, S. A. Dvoretsky, Z. D. Kvon, J. Ziegler, D. Weiss, and S. D. Ganichev, *Photogalvanic probing of helical edge channels in two-dimensional HgTe topological insulators*, Phys. Rev. B **95**, 201103 (2017).

[24] N. H. Lindner, G. Refael, and V. Galitski, *Floquet topological insulator in semiconductor quantum wells*, Nature **7**, 490–495 (2011).

[25] S. D. Ganichev, J. Diener, and W. Prettl, *Nonlinear far-infrared absorption in InSb due to light impact ionization*, Appl. Phys. Lett. **64**, 1977–1979 (1994).

[26] A. G. Markelz, N. G. Asmar, B. Brar, and E. G. Gwinn, *Interband impact ionization by terahertz illumination of InAs heterostructures*, Appl. Phys. Lett. **69**, 3975–3977 (1996).

[27] P. Gaal, K. Reimann, M. Woerner, T. Elsaesser, R. Hey, and K. H. Ploog, *Nonlinear Terahertz Response of n-Type GaAs*, Phys. Rev. Lett. **96**, 187402 (2006).

[28] H. Wen, M. Wiczer, and A. M. Lindenberg, *Ultrafast electron cascades in semiconductors driven by intense femtosecond terahertz pulses*, Phys. Rev. B **78**, 125203 (2008).

[29] M. C. Hoffmann, J. Hebling, H. Y. Hwang, K.-L. Yeh, and K. A. Nelson, *THz-pump/THz-probe spectroscopy of semiconductors at high field strengths [Invited]*, JOSA B **26**, A29 (2009).

[30] H. A. Hafez, X Chai, A Ibrahim, S Mondal, D Férachou, X Ropagnol, and T Ozaki, *Intense terahertz radiation and their applications*, J. Opt. **18**, 093004 (2016).

[31] A. T. Tarekegne, H. Hirori, K. Tanaka, K. Iwaszczuk, and P. U. Jepsen, *Impact ionization dynamics in silicon by MV/cm THz fields*, New J. Phys. **19**, 123018 (2017).

[32] S. D. Ganichev and W. Prettl, *Intense Terahertz Excitation of Semiconductors* (Oxford University Press, Oxford, 2005).

[33] S. D. Ganichev, A. P. Dmitriev, S. A. Emel'yanov, Y. V. Terent'ev, I. D. Yaroshetskii, and I. N. Yassievich, *Impact ionization in semiconductors under the influence of the electric field of an optical wave*, Zh. Eksp. Teor. Fiz. **90**, 445 (1986), [JETP **63**, 256 (1986)].

[34] L. V. Keldysh, *Concerning the theory of impact ionization in semiconductors*, Zh. Eksp. Teor. Fiz. **48**, 1692 (1965), [JETP **21**,1135 (1965)].

[35] S. Hubmann, S. Gebert, G. V. Budkin, V. V. Bel'kov, E. L. Ivchenko, A. P. Dmitriev, S. Baumann, M. Otteneder, J. Ziegler, D. Disterheft, D. A. Kozlov, N. N. Mikhailov, S. A. Dvoretsky, Z. D. Kvon, D. Weiss, and S. D. Ganichev, *High-frequency impact ionization and nonlinearity of photocurrent induced by intense terahertz radiation in HgTe-based quantum well structures*, Phys. Rev. B **99**, 085312 (2019).

[36] S. Hubmann, G. Budkin, M. Urban, V. Bel'kov, A. Dmitriev, J. Ziegler, D. Kozlov, N. Mikhailov, S. Dvoretsky, Z. Kvon, D. Weiss, and S. Ganichev, *Impact Ionization Induced by Terahertz Radiation in HgTe Quantum Wells of Critical Thickness*, J. Infrared Millim. Terahertz Waves **41**, 1155 –1169 (2020).

[37] E. L. Ivchenko, *Optical Spectroscopy of Semiconductor Nanostructures* (Alpha Sci. Int. Ltd., Harrow, 2005).

[38] X.-L. Qi and S.-C. Kane, *Topological insulators and superconductors*, Rev. Mod. Phys. **83**, 1057 (2011).

[39] J. Chu and A. Sher, *Physics and Properties of Narrow Gap Semiconductors* (Springer, Nov. 7, 2007).

[40] C. R. Whitsett and D. A. Nelson, *Lattice Thermal Conductivity of p-Type Mercury Telluride*, Phys. Rev. B **5**, 3125–3138 (1972).

[41] K.-M. Dantscher, *Terahertz Laser Spectroscopy of Two- and Three-Dimensional Topological Insulators basedon HgTe Nanostructures*, PhD thesis, University of Regensburg, 2017.

[42] D. J. Chadi, J. P. Walter, M. L. Cohen, Y. Petroff, and M. Balkanski, *Reflectivities and Electronic Band Structure of CdTe and HgTe*, Phys. Rev. B **5**, 3058 (1972).

[43] J. K. Furdyna, *Diluted magnetic semiconductors*, J. Appl. Phys. **64**, R29–R64 (1988).

[44] S. Murakami, N. Nagaosa, and S.-C. Zhang, *Spin-Hall Insulator*, Phys. Rev. Lett. **93** (2004).

[45] L. Fu and C. L. Kane, *Topological insulators with inversion symmetry*, Phys. Rev. B **76**, 045302 (2007).

[46] M. König, H. Buhmann, L. W. Molenkamp, T. Hughes, C.-X. Liu, X.-L. Qi, and S.-C. Zhang, *The Quantum Spin Hall Effect: Theory and Experiment*, J. Phys. Soc. Jpn. **77**, 031007 (2008).

[47] J.-W. Luo and A. Zunger, *Design Principles and Coupling Meachanisms in the 2D Quantum Well Topological Insulator HgTe/CdTe*, Phys. Rev. Lett. **105**, 176805 (2010).

[48] B. Wittmann, S. N. Danilov, V. V. Bel'kov, S. A. Tarasenko, E. G. Novik, H. Buhmann, C. Brüne, L. W. Molenkamp, Z. D. Kvon, N. N. Mikhailov, S. A. Dvoretsky, N. Q. Vinh, A. F. G. van der Meer, B. Murdin, and S. D. Ganichev, *Circular photogalvanic effect in HgTe/CdHgTe quantum well structures*, Semicond. Sci. Technol. **25**, 095005 (2010).

[49] R. Dornhaus and G. Nimtz, "Narrow-gap semiconductors", in, edited by G. Höhler (Springer Tracts in Modern Physics, 1983) Chap. The properties and applications of the $Hg_{1-x}Cd_xTe$ alloy system. Pp. 119–281.

[50] J. L. Schmit and E. L. Stelzer, *Temperature and Alloy Compositional Dependences of the Energy Gap of Hg1-xCdxTe*, J. Appl. Phys. **40**, 4865–4869 (1969).

[51] C. Rigaux, "Interband magnetooptics in narrow gap semiconductors", in *Narrow Gap Semiconductors Physics and Applications* (Springer Berlin Heidelberg, 1980), pp. 110–124.

[52] H. Overhof, *Relativistic Energy Bands of HgTe and HgSe*, Phys. Status Solidi B **43**, 221–226 (1971).

[53] M. Glazov and S. Ganichev, *High frequency electric field induced nonlinear effects in graphene*, Phys. Rep. **535**, 101–138 (2014).

[54] H. Plank, *Optoelectronic Phenomena Induced by Terahertz/Infrared Laser Radiation in Topological Insulators and Graphene*, PhD thesis, University of Regensburg, 2018.

[55] V. I. Belinicher and B. I. Sturman, *The photogalvanic effect in media lacking a center of symmetry*, Usp. Fiz. Nauk **130**, 415 (1980), [Sov. Phys. Usp. **23**, 199(1980)].

[56] B. I. Sturman and V. M. Fridkin, *The Photovoltaic and Photorefractive Effects in Non-Centrosymmetric Materials* (Gordon and Breach Science Publishers, New York, 1992).

[57] P. Olbrich, L. E. Golub, T. Herrmann, S. N. Danilov, H. Plank, V. V. Bel'kov, G. Mussler, C. Weyrich, C. M. Schneider, J. Kampmeier, D. Grützmacher, L. Plucinski, M. Eschbach, and S. D. Ganichev, *Room-Temperature High-Frequency Transport of Dirac Fermions in Epitaxially Grown Sb_2Te_3- and Bi_2Te_3-Based Topological Insulators*, Phys. Rev. Lett. **113**, 096601 (2014).

[58] W. Weber, L. E. Golub, S. N. Danilov, J. Karch, C. Reitmaier, B. Wittmann, V. V. Bel'kov, E. L. Ivchenko, Z. D. Kvon, N. Q. Vinh, A. F. G. van der Meer, B. Murdin, and S. D. Ganichev, *Quantum ratchet effects induced by terahertz radiation in GaN-based two-dimensional structures*, Phys. Rev. B **77**, 245304 (2008).

[59] S. A. Tarasenko, *Direct current driven by ac electric field in quantum wells*, Phys. Rev. B **83**, 035313 (2011).

[60] S. Candussio, M. V. Durnev, S. A. Tarasenko, J. Yin, J. Keil, Y. Yang, S.-K. Son, A. Mishchenko, H. Plank, V. V. Bel'kov, S. Slizovskiy, V. Fal'ko, and S. D. Ganichev, *Edge photocurrent driven by terahertz electric field in bilayer graphene*, Phys. Rev. B **102**, 045406 (2020).

[61] L. E. Golub, S. A. Tarasenko, M. V. Entin, and L. I. Magarill, *Valley separation in graphene by polarized light*, Phys. Rev. B **84**, 195408 (2011).

[62] S. D. Ganichev and W. Prettl, *Spin photocurrents in quantum wells*, J. Phys. Cond. Matt. **15**, R935 (2003).

[63] S. D. Ganichev, V. V. Bel'kov, P. Schneider, E. L. Ivchenko, S. A. Tarasenko, W. Wegschneider, D. Weiss, D. Schuh, E. V. Beregulin, and W. Prettl, *Resonant inversion of the circular photogalvanic effect in n-doped quantum wells*, Phys. Rev. B **68**, 035319 (2003).

[64] V. Kaladzhyan, P. P. Aseev, and S. N. Artemenko, *Photogalvanic effect in the HgTe/CdTe topological insulator due to edge-bulk optical transitions*, Phys. Rev. B **92**, 155424 (2015).

[65] M. V. Durnev and S. A. Tarasenko, *High-Frequency Nonlinear Transport and Photogalvanic Effects in 2D Topological Insulators*, Ann. Phys. **531**, 1800418 (2019).

[66] P. Valov, B. Ryvkin, I. Yaroshetskii, and I. Yassievich, *Intraband photoconductivity in n-type Ge caused by optical heating of electrons*, Fiz.Tekh. Poluprovodn. **5**, 904–910 (1971), [Sov. Phys. Semicond. **5**, 797-801(1971)].

[67] K. Seeger, *Semiconductor Physics: An Introduction* (Springer, 2004).

[68] E. H. Putley, *Far Infra-Red Photoconductivity*, Phys. Status Solidi B **6**, 571–614 (1964).

[69] E. V. Beregulin, P. M. Valov, S. M. Ryvkin, D. V. Tarkhin, and I. D. Yaroshetskii, *Very-fast-response uncooled photodetector based on intraband μ-photoconductivity*, Sov. J. Quantum Electron. **8**, 797–799 (1978).

[70] S. D. Ganichev, S. A. Emelianov, A. G. Pakhomov, I. V. Terentev, and I. D. Iaroshetskii, *Fast uncooled detector for far-IR and submillimeter laser beams*, Pis'ma Zh. Tekh. Fiz. **11**, 913–915 (1985), [Sov. Tech. Phys. Lett. **11**,377-378 (1985)].

[71] S. D. Ganichev, E. V. Beregulin, and I. D. Yaroshetskii, "Room-temperature high-sensitivity fast detector of FIR radiation", in Physical Concepts and Materials for Novel Optoelectronic Device Applications II, edited by F. Beltram and E. Gornik (1993).

[72] G. P. Agrawal, *Semiconductor lasers* (Van Nostrand Reinhold, New York, 1993).

[73] J. Carroll, *Hot electron microwave generators* (Edward Arnold, London, 1970).

[74] S. Sze and K. K. Ng, *Physics of Semiconductor Devices* (John Wiley & Sons, Inc., 2006).

[75] E. Yablonovitch and N. Bloembergen, *Avalanche Ionization and the Limiting Diameter of Filaments Induced by Light Pulses in Transparent Media*, Phys. Rev. Lett. **29**, 907–910 (1972).

[76] E. Yablonovitch, *Similarity principles for laser-induced breakdown in gases*, Appl. Phys. Lett. **23**, 121–122 (1973).

[77] N. Bloembergen, *Laser-induced electric breakdown in solids*, IEEE J. Quant. Electr. **10**, 375–386 (1974).

[78] I. V. Oladyshkin, S. B. Bodrov, Y. A. Sergeev, A. I. Korytin, M. D. Tokman, and A. N. Stepanov, *Optical emission of graphene and electron-hole pair production induced by a strong terahertz field*, Phys. Rev. B **96**, 155401 (2017).

[79] S. D. Ganichev, A. P. Dmitriev, S. A. Emel'yanov, Y. V. Terent'ev, I. D. Yaroshetskii, and I. N. Yassievich, *Impact ionization in a semiconductor in a light wave*, Pis'ma Zh. Eksp. Teor. Fiz. **40**, 187 (1984), [JETP Lett. **40**, 948 (1984)].

[80] B. Kochman, K. Yeom, and J. Singh, *Laser induced impact ionization in semiconductors: A Monte Carlo study for silicon*, Appl. Phys. Lett. **68**, 1936–1938 (1996).

[81] H. Maier, J. Ziegler, R. Fischer, D. Kozlov, Z. D. Kvon, N. Mikhailov, S. A. Dvoretsky, and D. Weiss, *Ballistic geometric resistance resonances in a single surface of a topological insulator*, Nat. Commun. **8**, 2023 (2017).

[82] S. Hubmann, G. V. Budkin, M. Otteneder, D. But, D. Sacré, I. Yahniuk, K. Diendorfer, V. V. Bel'kov, D. A. Kozlov, N. N. Mikhailov, S. A. Dvoretsky, V. S. Varavin, V. G. Remesnik, S. A. Tarasenko, W. Knap, and S. D. Ganichev, *Symmetry breaking and circular photogalvanic effect in epitaxial CdxHg1-xTe films*, Phys. Rev. Mat. **4** (2020).

[83] Y. G. Sidorov, S. A. Dvoretskii, V. S. Varavin, N. N. Mikhailov, M. V. Yakushev, and I. V. Sabinina, *Molecular-beam epitaxy of mercury-cadmium-telluride solid solutions on alternative substrates*, Semiconductors **35**, 1045–1053 (2001).

[84] S.-C. Tsen, D. J. Smith, J. Hutchins, B. Skromme, Y. Chen, and S. Sivananthan, *Heteroepitaxial CdTe(111) grown by MBE on nominally flat and misoriented Si(001) substrates: characterization by electron microscopy and optical methods*, J. Cryst. Growth **159**, 58–63 (1996).

[85] J. P. Zanatta, P. Ferret, G. Theret, A. Million, M. Wolny, J. P. Chamonal, and G. Destefanis, *Heteroepitaxy of HgCdTe (211)B on Ge substrates by molecular beam epitaxy for infrared detectors*, J. Electron. Mater. **27**, 542–545 (1998).

[86] T. J. de Lyon, R. D. Rajavel, J. A. Vigil, J. E. Jensen, O. K. Wu, C. A. Cockrum, S. M. Johnson, G. M. Venzor, S. L. Bailey, I. Kasai, W. L. Ahlgren, and M. S. Smith, *Molecular-beam epitaxial growth of HgCdTe infrared focal-plane arrays on silicon substrates for midwave infrared applications*, J. Electron. Mater. **27**, 550–555 (1998).

[87] S. Dvoretsky, N. Mikhailov, D. Ikusov, V. Kartashev, A. Kolesnikov, I. Sabinina, Y. G. Sidorov, and V. Shvets, "The Growth of CdTe Layer on GaAs Substrate by MBE", in *Cadmium Telluride (CdTe) - Prospects, Challenges and Applications* (IntechOpen, 2019).

[88] K. Renk, *Basics of Laser Physics* (Springer, Berlin Heidelberg, 2012).

[89] G. W. Chantry, *Long-wave optics : the science and technology of infrared and near-millimetre waves* (Academic Press, London Orlando, 1984).

[90] W. Demtröder, *Experimentalphysik 3* (Springer Berlin Heidelberg, 2016).

[91] S. Ganichev, *Tunnel ionization of deep impurities in semiconductors induced by terahertz electric fields*, Physica B **273-274**, 737–742 (1999).

[92] P. Olbrich, *THz radiation induced spin polarized currents in low dimensional semiconductor structures*, PhD thesis, University of Regensburg, 2010.

[93] S. D. Ganichev, Y. V. Terent'ev, and I. D. Yaroshetskii, *Photon-drag photodetectors for the far-IR and submillimeter regions*, Pis'ma Zh. Tekh. Fiz. **11**, 46 (1985), [Sov. Tech. Phys. Lett. **11**, 20 (1989)].

[94] P. Faltermeier, *Terahertz Laser Induced Ratchet Effects and Magnetic Quantum Ratchet Effects in Semiconductor Nanostructures*, PhD thesis, University of Regensburg, 2017.

[95] S. V. Morozov, M. S. Joludev, A. V. Antonov, V. V. Rumyantsev, V. I. Gavrilenko, V. Y. Aleshkin, A. A. Dubinov, N. N. Mikhailov, S. A. Dvoretskiy, O. Drachenko, S. Winnerl, H. Schneider, and M. Helm, *Study of lifetimes and photoconductivity relaxation in heterostructures with* $Hg_x Cd_{1-x} Te/Cd_y Hg_{1-y} Te$ *quantum wells*, Fiz. Tekh. Poluprovodn. **46**, 1388 (2012), [Semicond. **46**, 1362 (2012)].

[96] L. V. Keldysh, *Ionization in the Field of a Strong Electromagnetic Wave*, Zh. Eksp. Teor. Fiz. **47**, 1945–1957 (1964), [JETP **20**,1307 (1964)].

[97] S. D. Ganichev, S. A. Emel'yanov, E. L. Ivchenko, E. Y. Perlin, Y. V. Terent'ev, A. V. Fedorov, and I. D. Yaroshetskii, *Multiphoton absorption in semiconductors at submillimeter wavelengths*, Sov. Phys. JETP **64**, 729–737 (1986).

[98] V. F. Gantmakher, Y. B. Levinson, A. A. Grinberg, and S. Luryi, *Carrier Scattering in Metals and Semiconductors*, Phys. Today **41**, 84–85 (1988).

[99] P. Y. Yu and M. Cardona, *Fundamentals of Semiconductors* (Springer Berlin Heidelberg, 2010).

[100] V. I. Belinicher, E. L. Ivchenko, and B. I. Sturman, *Kinetic theory of the displacement photovoltaic effect in piezoelectric*, Zh. Eksp. Teor. Fiz. **83**, 649 (1982), [JETP **56**, 359 (1982)].

[101] J. E. Sipe and A. I. Shkrebtii, *Second-order optical response in semiconductors*, Phys. Rev. B **61**, 5337–5352 (2000).

[102] L. E. Golub and E. L. Ivchenko, *Shift photocurrent induced by two-quantum transitions*, Zh. Eksp. Teor. Fiz. **139**, 175–183 (2011), [JETP **112**, 152 (2011)].

[103] S. M. Young and A. M. Rappe, *First Principles Calculation of the Shift Current Photovoltaic Effect in Ferroelectrics*, Phys. Rev. Lett. **109**, 116601 (2012).

[104] U. Bajpai, B. S. Popescu, P. Plecháč, B. K. Nikolić, L. E. F. F. Torres, H. Ishizuka, and N. Nagaosa, *Spatio-temporal dynamics of shift current quantum pumping by femtosecond light pulse*, J. Phys.: Mater. **2**, 025004 (2019).

[105] P. Olbrich, C. Zoth, P. Vierling, K.-M. Dantscher, G. V. Budkin, S. A. Tarasenko, V. V. Bel'kov, D. A. Kozlov, Z. D. Kvon, N. N. Mikhailov, S. A. Dvoretsky, and S. D. Ganichev, *Giant photocurrents in a Dirac fermion system at cyclotron resonance*, Phys. Rev. B **87**, 235439 (2013).

[106] Y. B. Lyanda-Geller and G. E. Pikus, *Circular photogalvanic effect in deformed nongyrotropic crystals*, Fiz. Tverd. Tela **31**, 77 (1989), Sov. Phys.-Solid State **31**, 2068.

[107] M. Otteneder, D. Sacré, I. Yahniuk, G. V. Budkin, K. Diendorfer, D. A. Kozlov, I. A. Dmitriev, N. N. Mikhailov, S. A. Dvoretsky, V. V. Bel'kov, W. Knap, and S. D. Ganichev, *Terahertz Magnetospectroscopy of Cyclotron Resonances from Topological Surface States in Thick Films of $Cd_xHg_{1-x}Te$*, Phys. Status Solidi B, 2000023 (2020).

[108] K.-M. Dantscher, D. A. Kozlov, P. Olbrich, C. Zoth, P. Faltermeier, M. Lindner, G. V. Budkin, S. A. Tarasenko, V. V. Bel'kov, Z. D. Kvon, N. N. Mikhailov, S. A. Dvoretsky, D. Weiss, B. Jenichen, and S. D. Ganichev, *Cyclotron-resonance-assisted photocurrents in surface states of a three-dimensional topological insulator based on a strained high-mobility HgTe film*, Phys. Rev. B **92**, 165314 (2015).

[109] G. Bir and G. Pikus, *Symmetry and Strain-induced Effects in Semiconductors* (Wiley, New York, 1974).

[110] S. A. Tarasenko, *Orbital mechanism of the circular photogalvanic effect in quantum wells*, JETP Lett. **85**, 182 (2007).

[111] E. G. Novik, A. Pfeuffer-Jeschke, T. Jungwirth, V. Latussek, C. R. Becker, G. Landwehr, H. Buhmann, and L. W. Molenkamp, *Band structure of semimagnetic $Hg_{1-y}Mn_yTe$ quantum wells*, Phys. Rev. B **72**, 035321 (2005).

[112] S. Adachi, *Handbook on Physical Properties of Semiconductors* (Kluwer Academic Publishers, Boston, 2004).

[113] G. Pikus, V. Marushchak, and A. Titkov, *Spin Splitting of Energy Bands and spin relaxation of carriers in cubic III-V crystals (Review)*, Sov. Phys. Semicond. **22**, 115 (1988).

[114] V. A. Shalygin, H. Diehl, C. Hoffmann, S. N. Danilov, T. Herrle, S. A. Tarasenko, D. Schuh, C. Gerl, W. Wegscheider, W. Prettl, and S. D. Ganichev, *Spin photocurrents and the circular photon drag effect in (110)-grown quantum well structures*, JETP Lett. **84**, 570–576 (2007).

[115] V. A. Shalygin, M. D. Moldavskaya, S. N. Danilov, I. I. Farbshtein, and L. E. Golub, *Circular photon drag effect in bulk tellurium*, Phys. Rev. B **93**, 045207 (2016).

[116] J. Karch, P. Olbrich, M. Schmalzbauer, C. Zoth, C. Brinsteiner, M. Fehrenbacher, U. Wurstbauer, M. M. Glazov, S. A. Tarasenko, E. L. Ivchenko, D. Weiss, J. Eroms, R. Yakimova, S. Lara-Avila, S. Kubatkin, and S. D. Ganichev, *Dynamic Hall Effect Driven by Circularly Polarized Light in a Graphene Layer*, Phys. Rev. Lett. **105**, 227402 (2010).

[117] C. Jiang, V. A. Shalygin, V. Y. Panevin, S. N. Danilov, M. M. Glazov, R. Yakimova, S. Lara-Avila, S. Kubatkin, and S. D. Ganichev, *Helicity-dependent photocurrents in graphene layers excited by midinfrared radiation of a CO_2 laser*, Phys. Rev. B **84**, 125429 (2011).

[118] S. D. Ganichev, S. A. Emel'yanov, E. L. Ivchenko, E. Y. Perlin, and I. D. Yaroshetskii, *Many-photon absorption in p-Ge in the submillimeter range*, JETP Lett. **37**, 568–570 (1983).

[119] S. D. Ganichev, W. Prettl, and P. G. Huggard, *Phonon assisted tunnel ionization of deep impurities in the electric field of far-infrared radiation*, Phys. Rev. Lett. **71**, 3882–3885 (1993).

[120] S. D. Ganichev, I. N. Yassievich, W. Prettl, J. Diener, B. K. Meyer, and K. W. Benz, *Tunneling Ionization of Autolocalized DX^- Centers in Terahertz Fields*, Phys. Rev. Lett. **75**, 1590–1593 (1995).

Acknowledgements

On the last page of this thesis I would like to thank everyone who supported me on my way to this thesis.

Special thanks goes to my doctorate supervisor, Sergey D. Ganichev for giving me the opportunity to do my PhD in a great working atmosphere and always supporting me throughout the entire thesis. Thank you for always being open for questions and giving suggestions for improvements.

Many thanks also to my colleagues Susanne Candussio, Maximilian Otteneder, Erwin Mönch for proofreading and, together with Sergey Danilov as well as Helene Plank, Kathrin-Maria Dantscher, Tobias Herrmann, and Philipp Faltermeier, thanks for providing a pleasant working atmosphere and for the support. In the same way I also want to give my thanks to former and current bachelor and master students, especially Michael Urban, Sebastian Gebert, Jakob Kox and Susanne Baumann. For always providing solutions to technical problems, I want to additionally thank Christian Schneider. For my help with formal things thanks go to Hannelore Lanz and Claudia Moser. I also want to say thanks to Johannes Ziegler for helping me with the treatment of the HgTe samples.

A big thanks also goes to Grisha Budkin for providing the theoretical support for almost any experimental results, proofreading my manuscript and thousands of band structure calculations. Equally, thanks go also to Alexander Dmitriev, Leonid Golub, Sergey Tarasenko, Vasily Bel'kov and Eugenius Ivchenko for providing theoretical calculations and models corresponding to my work.

Further thanks go to Dima Kozlov for nice discussions of sample and transport properties and additionally the whole HgTe growth group in Novosibirsk for providing the samples needed to perform this work. Additionally I want to thank the entire groups of Jonathan Eroms and Dima Efetov, for providing samples and discussions for the studies on mono- and bilayer graphene.

Moreover, I want to thank my parents for supporting me all the way from the beginning in the bachelor degree course to the PhD, representing the whole family.

Last but not least I want to thank all of my friends for providing distraction from the work and cheering me up.